DISSERTATIONES
CHIMICAE
UNIVERSITATIS
TARTUENSIS
224

PATRICK TEPPOR

Obtaining platinum-free oxygen reduction catalysts through biomass valorization: a case study of peat

DISSERTATIONES CHIMICAE UNIVERSITATIS TARTUENSIS
224

DISSERTATIONES CHIMICAE UNIVERSITATIS TARTUENSIS
224

PATRICK TEPPOR

Obtaining platinum-free oxygen reduction catalysts through biomass valorization: a case study of peat

UNIVERSITY OF TARTU
Press
1632

Institute of Chemistry, Faculty of Science and Technology, University of Tartu, Estonia

The dissertation is accepted for the commencement of the degree of Doctor of Philosophy in Chemistry on June 22nd, 2023, by the Council of Institute of Chemistry, University of Tartu.

Supervisors: Research Fellow Rutha Jäger, Ph.D.
University of Tartu, Estonia

Professor Enn Lust, Ph.D.
University of Tartu, Estonia

Opponent: Alexey Serov, Ph.D.
Oak Ridge National Laboratory, United States

Commencement: 30.08.2023 at 16:15 in auditorium 1020, Ravila 14a, Tartu (in-person) and Microsoft Teams (online)

This work has been partially supported by ASTRA project PER ASPERA Graduate School of Functional Materials and Technologies receiving funding from the European Regional Development Fund under project in University of Tartu, Estonia

ISSN 1406-0299 (print)
ISBN 978-9916-27-298-5 (print)
ISSN 2806-2159 (pdf)
ISBN 978-9916-27-299-2 (pdf)

University of Tartu Press
www.tyk.ee

TABLE OF CONTENTS

1. LIST OF ORIGINAL PUBLICATIONS

This thesis consists of four original publications listed below. The articles are referred to as Roman numerals in the text.

I. **P. Teppor**, R. Jäger, M. Paalo, R. Palm, O. Volobujeva, E. Härk, Z. Kochovski, T. Romann, R. Härmas, J. Aruväli, A. Kikas, E. Lust, Peat-derived carbon-based non-platinum group metal type catalyst for oxygen reduction and evolution reactions, *Electrochemistry Communications*, 113, **2020**, 106700.

II. R. Jäger, **P. Teppor**, M. Paalo, M. Härmas, A. Adamson, O. Volobujeva, E. Härk, Z. Kochovski, T. Romann, R. Härmas, J. Aruväli, A. Kikas, E. Lust, Synthesis and Characterization of Cobalt and Nitrogen Co-Doped Peat-Derived Carbon Catalysts for Oxygen Reduction in Acidic Media, *Catalysts*, 11, **2021**, 715.

III. **P. Teppor**, R. Jäger, M. Paalo, A. Adamson, M. Härmas, O. Volobujeva, J. Aruväli, R. Palm, E. Lust, Peat as a carbon source for non-platinum group metal oxygen electrocatalysts and AEMFC cathodes, *International Journal of Hydrogen Energy*, 47, **2022**, 16908.

IV. **P. Teppor**, R. Jäger, M. Koppel, O. Volobujeva, R. Palm, M. Månsson, E. Härk, Z. Kochovski, J. Aruväli, K. Kooser, S. Granroth, T. Käämbre, J. Nerut, E. Lust, Unlocking the Porosity of Fe-N-C Catalysts Using Hydroxyapatite as a Hard Template En Route to Eco-Friendly High-Performance AEMFCs (manuscript).

Author's contribution:

Publication I: The author performed the synthesis of the catalysts, N_2 sorption measurements, and electrochemical characterization. The author was primarily responsible for interpreting the data and writing the manuscript.

Publication II: The author performed the synthesis of the catalysts, N_2 sorption measurements, and electrochemical characterization. The author participated in interpreting the data and writing the manuscript.

Publication III: The author performed the synthesis of the catalysts, N_2 and Ar sorption measurements, laser diffraction measurements, and electrochemical characterization. The author was primarily responsible for interpreting the data and writing the manuscript.

Publication IV: The author performed the synthesis of the catalysts, N_2 sorption and laser diffraction measurements, and electrochemical characterization. The author was primarily responsible for interpreting the data and writing the manuscript.

2. ABBREVIATIONS AND SYMBOLS

AEM	anion exchange membrane
AEMFC	anion exchange membrane fuel cell
BET	Brunauer-Emmett-Teller
C	concentration of oxygen
CCM	catalyst-coated membrane
D	diffusion coefficient
$Dv50$	median volumetric particle size
E	electrode potential
E_{onset}	onset potential
$E_{1/2}$	half-wave potential
F	Faraday constant
GCDE	glassy carbon disc electrode
GDE	gas diffusion electrode
GDL	gas diffusion layer
HA	hydroxyapatite
HOR	hydrogen oxidation reaction
HR-SEM	high-resolution scanning electron microscopy
I	current
I_D	intensity of the D band
I_{disc}	disc current
I_G	intensity of the G band
I_k	kinetic current
I_{mt}	mass transport current
IPA	isopropyl alcohol
I_{ring}	ring current
j	current density
j_c	corrected current density
MA	mass activity
M-N_x	metal coordinated to x number of nitrogen atoms
MEA	membrane electrode assembly
N	collection efficiency of the Pt ring
$n_{K\text{-}L}$	electron transfer number according to the Koutecký-Levich analysis
NPGM	non-platinum group metal
ORR	oxygen reduction reaction
ω	electrode rotation speed
P	power
PDC	peat-derived carbon
PEM	proton exchange membrane
PEMFC	proton exchange membrane fuel cell
PGM	platinum-group metal
PPD	peak power density

PTFE	polytetrafluoroethylene
RDE	rotating disc electrode
RHE	reversible hydrogen electrode
RRDE	rotating ring disc electrode
R(R)DE	rotating (ring) disc electrode
S	electrode area
SEM-EDS	scanning electron microscope energy-dispersive spectroscopy
S_{BET}	specific surface area according to the BET multipoint theory
S_{DFT}	specific surface area according to the SAIEUS pore size distribution
SSA	specific surface area
TEM	transmission electron microscopy
TPB	triple-phase boundary
U	voltage
V_{DFT}	specific pore volume according to the SAIEUS pore size distribution
V_{micro}	micropore specific pore volume according to the SAIEUS pore size distribution
V_{TOT}	specific pore volume calculated from the isotherm data at a relative pressure of 0.95
v	kinematic viscosity
WE	working electrode
XAS	X-ray absorption spectroscopy
XPS	X-ray photoelectron spectroscopy
XRD	X-ray diffraction
2D-NLDFT-HS	two-dimensional non-local density functional theory for carbon materials with a heterogeneous surface

3. INTRODUCTION

As countries all over the world shift away from relying on fossil fuels towards more environmentally friendly options, the adoption of renewable energy sources such as solar and wind continues to skyrocket [1]. In Estonia, developing solar and wind parks has gained serious attention only recently [2,3] mainly as the direct result of a significant reduction in cost [4] and the energy crisis of the 2022/23 winter season [5]. Despite a relatively late start compared to other countries, ambitious plans have already been established. For instance, wind power projects with a cumulative power capacity of almost 10 GW are under development [3]. As a result, the power demand of the country with a peak of roughly 1.6 GW [6] should be more than satisfied. However, a majority of that energy will be produced offshore while the main power lines are located on the other side of the country. Additionally, the excess energy needs to be curtailed to keep the electricity grid stable. While this may be considered a problem, it also presents a unique opportunity.

Many of the issues created by avoiding fossil fuels can be solved by direct electrification [7]. However, several applications will still require energy in a different form other than electricity [8]. Thus, a “green” fuel is needed for these hard-to-abate sectors. Large political organizations and governments have decided that the fuel of the future will be hydrogen and its derivatives [9,10]. Hydrogen can be easily produced via electrolysis using the excess energy generated by renewables presenting an economical solution to the issue of curtailment. It can then be stored, transported, and used for many applications including as a fuel for fuel cells [11].

Fuel cells convert the chemical energy of hydrogen and oxygen into electrical energy through electrochemical reactions. Both reactions require catalysts to proceed at sufficient rates, but the issue is magnitudes worse for the oxygen reduction reaction (ORR). As a result, a considerable amount of platinum is needed for practically applicable fuel cells making them fairly expensive [12]. Solving this problem has demanded several decades of attention from researchers around the world [13]. Currently, the most promising alternative to conventional platinum-based catalysts is the non-platinum group metal (NPGM) catalyst, which is mainly composed of carbon, nitrogen, and an inexpensive transition metal, such as Fe or Co [14]. As these novel catalysts have been consistently improved over time, it has become increasingly relevant to fabricate them from abundant resources to minimize their potential cost.

In this work, we hypothesize that active NPGM ORR catalysts can be synthesized from naturally abundant well-decomposed peat. Well-decomposed peat is a biomass that is currently used only in low-value applications, namely as a source of heat energy [15]. Converting well-decomposed peat into an advanced functional material would present a unique opportunity to facilitate the adoption of fuel cells and hydrogen by valorizing naturally abundant resources.

The well-decomposed peat was converted into NPGM ORR catalysts through two synthesis pathways discussed in more detail below. The performances of the obtained peat-derived carbon (PDC) materials were analyzed both in alkaline and acidic media, and in three-electrode and fuel cell measurement setups. A wide array of physical characterization methods were utilized to elucidate why some materials are better ORR catalysts than others. Combining the knowledge gained throughout the study led to a PDC catalyst with excellent activity owing to its suitable physical properties.

4. LITERATURE OVERVIEW

4.1. The modern fuel cell

4.1.1. Basic operating principles

A fuel cell is a device that converts the chemical energy of a fuel and an oxidant into electrical energy. The specific requirements for the fuel and the oxidant as well as the operating conditions for the energy conversion process depend on the type of the fuel cell. While there are numerous vastly different types of fuel cells, the current market is dominated by the proton exchange membrane fuel cell (PEMFC). Out of the 2.3 GW of fuel cells shipped in 2021, PEMFCs take up a commanding 86% share [16].

A PEMFC uses hydrogen and oxygen as the fuel and oxidant, respectively. These gases are converted to electricity through electrochemical reactions occurring at the anode and cathode of the fuel cell, respectively (**Figure 1a**). In the layered structure of the fuel cell, the electrons produced from hydrogen at the anode flow to the cathode through the external circuit allowing useful electrical energy to be harnessed. To complete the circuit, the protons produced at the anode flow to the cathode through a proton-conducting polymer layer called the proton exchange membrane (PEM) or more generally the polymer electrolyte membrane. The overall environment of a PEMFC is highly acidic due to the nature of the membrane.

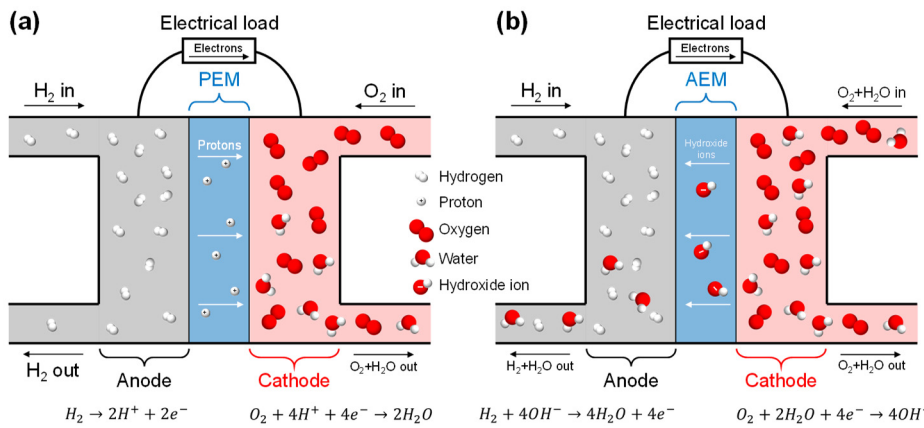

Figure 1. The basic operating principles, general structures, and electrochemical reactions occurring at the anodes and cathodes of (a) PEMFCs and (b) AEMFCs.

Another representative of low-temperature fuel cells, meaning fuel cells usually operating below 100 °C, alongside the PEMFC is the anion exchange membrane fuel cell (AEMFC). The operating principles of an AEMFC are largely like those of the PEMFC with two critical exceptions (**Figure 1b**).

Firstly, the polymer membrane known as an anion exchange membrane (AEM) conducts hydroxide ions instead of protons resulting in an alkaline environment. This has major implications for the materials that can be used in the device as discussed in the following section. Secondly, the role of water changes from a product to a reactant. Managing water in a fuel cell is crucial since both flooding and drying will significantly impede the performance. Despite the commercialization status of low-temperature fuel cells, water management remains a topic of great interest in the scientific community [17–20].

An even more critical factor determining the performance of a fuel cell besides water management is the rate at which the hydrogen oxidation reaction (HOR) and oxygen reduction reaction (ORR) occur. Without assistance, the rates of both reactions are too slow to be applied in a practical energy conversion device. Hence, catalysts are used at both the anode and the cathode to speed up the HOR and ORR, respectively. Over the almost two centuries of fuel cell history, platinum has earned its place as the supreme catalyst for low-temperature fuel cells [21]. While the HOR proceeds at sufficient rates even with extremely low amounts of catalyst, the ORR is markedly more sluggish and requires considerably larger amounts of catalyst [22]. As a result, current research and development is heavily weighted towards developing and studying ORR catalysts [23].

4.1.2. Main components

As briefly implied above, the most important part of the fuel cell is the 3-layer structure consisting of the anode, membrane, and cathode called a membrane-electrode assembly (MEA) (**Figure 2**). The anode and cathode are often more specifically referred to as the anode and cathode catalyst layers, respectively, which are mainly made up of a catalyst material. In a modern fuel cell, the catalyst material is in turn comprised of catalytically active particles and a carbon support material. For the active particles, the Toyota Mirai fuel cell vehicle utilizes a PtCo alloy with a particle size of roughly 3.5–4.1 nm [24]. These particles are deposited on a carbon support material with a high specific surface area (*SSA*) and suitable porosity for optimal distribution of active particles as well as facile and efficient transport of reactants and products. The catalyst layers additionally consist of an ionomer network connecting the active particles or more specifically the active sites to the membrane to ensure optimal ion transport. The ionomer has properties largely identical to the membrane but is mainly in the form of individual fibers. An extensive ionomer network is required because the ORR and HOR only occur at the triple-phase boundaries (TPB) of gas-ionomer-active site as depicted in **Figure 2**.

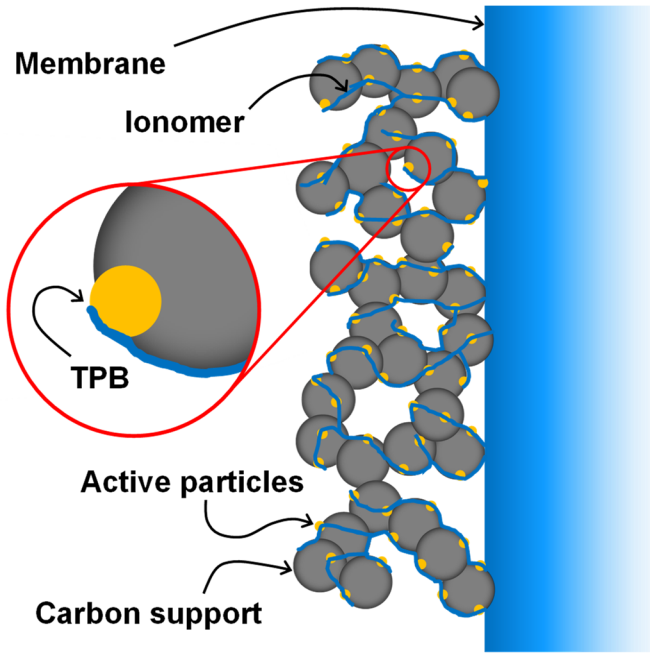

Figure 2. A graphical representation of one side of a platinum-based MEA and the formation of a triple-phase boundary.

In contrast to the catalyst layers, the membrane is a relatively simple gas-impermeable electron-insulating polymer which is as thin and ion-conductive as possible to minimize ohmic losses. For instance, a Toyota Mirai fuel cell vehicle utilizes a membrane that is only ~10 µm thick [25]. The membrane has been chemically functionalized to conduct protons or hydroxide ions. These functional groups determine the environment of the fuel cell. A proton-conducting membrane typically has sulfonic acid functional groups resulting in an acidic environment. The most well-known PEM material is Nafion™, which was developed in the early 1970s [26] and is still widely used due to its excellent properties [27]. Hydroxide-conducting membranes have not reached the technological maturity level of their acidic counterparts yet and thus a variety of functional groups are used which all ultimately generate an alkaline environment [28]. As a result, the choice of AEMs is more varied and a single prime candidate has not emerged yet.

The environment of a fuel cell sets strict restrictions on the materials that can be used. In an acidic PEMFC, platinum-group metals (PGMs) are currently the only practical options for catalysts owing to their high chemical stability. However, intensive research is still being conducted to identify and develop inexpensive alternatives to platinum [29]. Of these alternatives, non-platinum group metal (NPGM) catalysts based on carbon, nitrogen, and inexpensive transition metals discussed in more detail below have shown the highest performance. However, overcoming the challenges of the harsh acidic environment of

PEMFCs is exceedingly difficult for NPGM catalysts as demonstrated by their insufficient stability [30].

NPGM catalysts could instead be much more successful in the alkaline AEMFC. Numerous studies have shown how these materials are distinctly more stable in alkaline conditions compared to an acidic environment [31–33]. So far, the AEMFC has remained a relatively niche subject due to a severe bottleneck in the membrane technology. However, several research groups have recently demonstrated major breakthroughs in developing anion exchange membranes with sufficient conductivity and promising stability [34–39]. Some have even proceeded with commercializing their findings. As a result, AEMFCs utilizing NPGM catalysts have become a topic worth seriously considering as a future alternative to platinum-based PEMFCs.

In addition to the MEA, the fuel cell consists of several other components which are mainly responsible for distributing reactants to and products from the TPB as well as electron and heat conduction. These components, such as the gas diffusion layers (GDLs), flow fields, and bipolar plates, are mainly based on carbon or metals covered with corrosion-resistant coatings. An in-depth overview of these components in the modern fuel cell has been given by Jiao et al. [25].

4.1.3. Bottleneck inhibiting widespread adoption

Despite significant advances in the design of fuel cells, their adoption is still severely lagging behind other devices used in the field of renewable energy, such as batteries and solar panels. While the reasons are numerous, the most pressing concern currently is still the cost of a fuel cell. Only a few suppliers provide a price upfront and these are mainly for small systems below 5 kW [40]. According to estimates, the cost of larger fuel cells ranges loosely from 1727 to 3140 € per kW [41]. However, the cost is expected to markedly decrease once production rates scale up [42].

Ultimately, the scarcity of platinum will become a critical bottleneck when an economy of scale is realized for fuel cells. Approximately 190 tons of platinum are mined annually [43], and this capacity can only be increased by roughly 10% each year [44]. Modern fuel cells require at least 0.1 g of platinum per kW [45]. Accordingly, 1.9 TW of fuel cells can be produced annually at current conditions. Assuming a 100 kW fuel cell per vehicle leads to a yearly hydrogen vehicle production rate of 19 million units compared to the 80 million motor vehicles produced in 2021 [46]. This results in a maximal market penetration of 24% if all the mined platinum was directed to fuel cell production. A similar conclusion was reached by Reverdiau et al. [44], who demonstrated that a market penetration of 20% or more can only be achieved with significant progress in required platinum per power unit and rigorous platinum recycling. Alarmingly, the study also demonstrates that without progress in these aspects platinum reserves will run out by 2045. Furthermore, platinum is highly concentrated with South Africa, Russia, and Zimbabwe as the three largest producers raising major geopolitical issues [43]. Clearly, solving these

issues is needed for fuel cells to be implemented at a large scale. As a result, intense research is being conducted to find alternative catalyst materials to platinum to solve the issue of raw material scarcity [29].

4.2. Making fuel cells better

4.2.1. Non-platinum group metal oxygen reduction catalysts

Non-platinum group metal oxygen reduction catalysts are promising alternatives to conventional catalysts. Their main advantage is being composed of abundant elements potentially making them significantly more inexpensive than platinum-based catalysts [47]. The bulk of an NPGM catalyst is carbon which by itself exhibits low activity. Adequate catalytic activity is achieved by modifying the carbon with nitrogen and a transition metal.

Synthesizing NPGM catalysts can be done via two principal pathways (**Figure 3**) [47]. Pathway #1 starts with carbonizing a carbon precursor into a carbon support, which is then decorated with active sites resulting in a catalyst analogous to the conventional platinum-based catalyst. With this method, the porosity of the catalyst can be precisely controlled by using carbon support materials with pre-defined porosities. In pathway #2, the carbon is formed from a precursor simultaneously to the active sites, typically in a one-pot method. Consequently, the active sites are embedded directly into the carbon network.

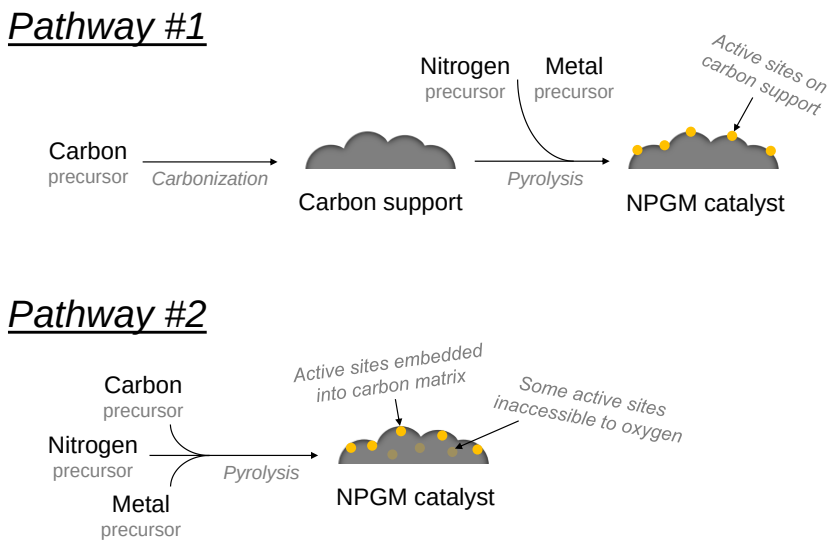

Figure 3. Graphical depictions of NPGM catalyst synthesis pathway #1 (top) and pathway #2 (bottom).

As Gupta et al. demonstrated in 1989 [48], NPGM catalysts can be synthesized by pyrolyzing simple compounds acting as sources of carbon, nitrogen, and transition metal at a high temperature opening a path for virtually endless combinations of precursors. Throughout the years, this approach has been validated by many workgroups demonstrating NPGM catalysts obtained with countless different precursors. However, the choice of the specific type of precursor strongly affects the final performance of the NPGM catalyst [49]. For the transition metal, Fe and Co have demonstrated the best results so far with the former generally providing higher activity and the latter better stability [50]. For the nitrogen precursor, high activity has been obtained with a wider array of substances, such as polymers (polyaniline [51]), cyclic molecules (melamine [52]), and acyclic compounds (dicyandiamide [53]). It has been discussed that these precursors are suitable nitrogen sources due to their structures containing delocalized electrons and their low cost [54]. In the present study we use one representative of the cyclic class of compounds, 2,2'-bipyridine, and one representative of dicyandiamide-like compounds, guanidine carbonate.

Both pathway #1 and pathway #2 have proven to yield catalysts with excellent activity. A survey of the best-performing NPGM catalysts in both PEMFCs and AEMFCs using data provided by Akula et al. [55] and Hossen et al. [56], respectively, reveals that 6 out of 20 can be categorized as pathway #1 catalysts with the rest as pathway #2 catalysts. In general, researchers are trending towards pathway #2 as understanding of NPGM catalysts has improved significantly over the course of the past decade. Most importantly, it was observed that contrary to conventional catalysts where discrete particles provide the active sites, specific moieties of nitrogen alone or in combination with a transition metal embedded into the carbon matrix constitute the main active sites in NPGM catalysts and will be discussed in the following section [57]. The ability of a moiety to effectively reduce oxygen and the amount of these moieties in a catalyst will be collectively referred to as the intrinsic activity of a catalyst in the present work. An additional factor in favor of pathway #2 is limiting the number of steps in the synthesis as the economic viability of this new type of catalyst needs to be considered.

4.2.2. Improving intrinsic activity

As discussed above, the intrinsic activity of a catalyst is determined by its moieties. Unfortunately for researchers, these moieties are rather difficult to study with current methods [58]. Furthermore, there are numerous different moieties all with different activities towards the ORR (**Figure 4**) [57]. The nitrogen and the transition metal (M) form M-N_x moieties where the metal can be bonded to nitrogen atoms numbering from two up to five. The activity of the M-N_x moiety is in turn influenced by its local environment, i.e., the surrounding carbon atoms. Several noteworthy authors have proposed that out of all the possibilities, the M-N_4 moiety provides the highest activity [59–62]. These

moieties were only recently directly visualized with advanced microscopy techniques by Chung et al. [63].

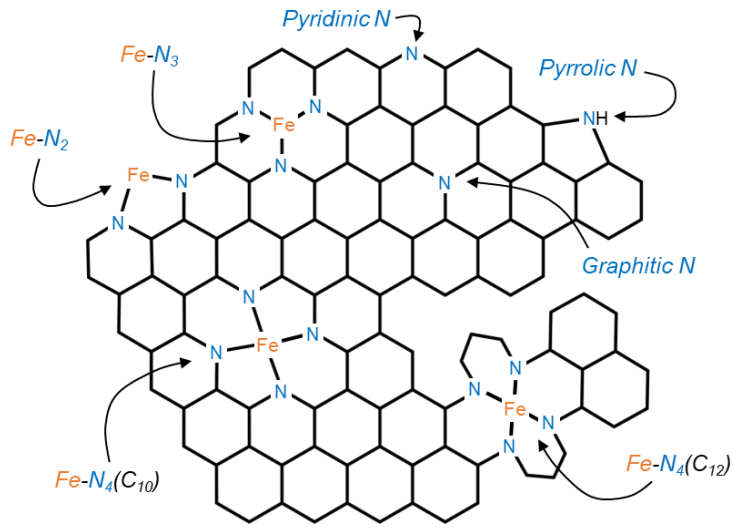

Figure 4. An illustration visualizing some of the possible active sites of a Fe-based NPGM catalyst adapted from reference [57].

Additionally, nitrogen moieties embedded into the carbon matrix without being bonded to a transition metal also constitute as active sites (**Figure 4**). The specific nature of the nitrogen is commonly analyzed with X-ray photoelectron spectroscopy which can deconvolute the sum signal of nitrogen into several nitrogen species, such as pyridinic, pyrrolic, graphitic, and nitrogen-oxide species. There is still active debate regarding which of these species provides the highest activity [64–66].

Another complication is that only a few moieties can directly reduce oxygen to water through the 4-electron pathway as is the case for platinum (**Figure 5**, Equation 1.1) [57]. Most moieties can reduce oxygen to hydrogen peroxide through the 2-electron pathway (Equation 1.2). The hydrogen peroxide can then be reduced to water at the same moiety, travel to a neighboring active site completing the 2+2-electron pathway (Equation 1.3) or escape the catalyst layer. The 4-electron pathway is greatly preferred as escaped hydrogen peroxide can damage the catalyst or the other components of the fuel cell leading to a short-lived system [67]. Similar principles apply for the alkaline environment, where oxygen is reduced to hydroxide ions in the preferred direct 4-electron pathway (Equation 2.1). The 2-electron pathway yields a hydroperoxide anion (Equation 2.2) which can be reduced further (Equation 2.3) or escape from the catalyst layer potentially damaging the system.

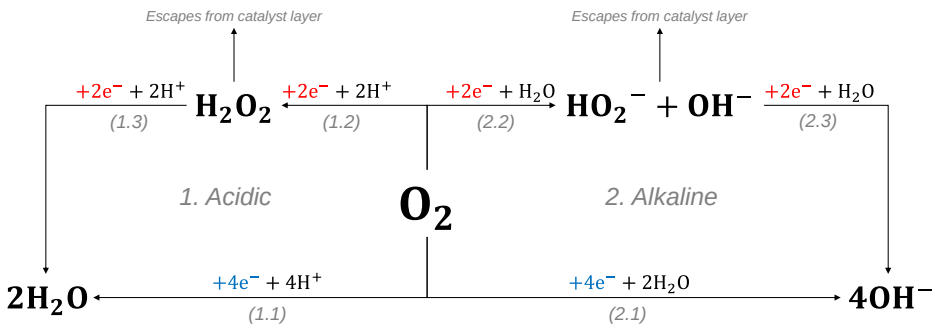

Figure 5. The 2- and 2+2-electron (top) and 4-electron (bottom) pathways for the ORR in acidic (left) and alkaline (right) media.

Improving the intrinsic activity of a catalyst is done by refining the synthesis procedure. First, a set of carbon, nitrogen, and metal precursors are chosen which lead to decent activity in an R(R)DE test. The synthesis conditions are then rigorously optimized, such as varying the amounts of precursors and the pyrolysis temperature. For instance, increasing the amount of metal will improve the intrinsic activity of a catalyst only up to a limit as the M-N_x moieties will start being replaced by agglomerated metallic particles with lower or no activities [68–70]. Additionally, the formation of both the M-N_x and N moieties can be influenced by the pyrolysis temperature [71]. For example, according to Zhang et al. [72] moieties with considerable activity towards the ORR start forming at a minimal temperature of 800 °C. Increasing the temperature resulted in more graphitic nitrogen species at the expense of pyridinic nitrogen leading to enhanced ORR activity in their case. Contrarily, others have reported that moieties with considerable activity can start forming already at a low temperature of 400 °C and a higher temperature may be only required for forming a carbon matrix [73]. In general, active catalysts have been obtained by using pyrolysis temperatures ranging from 800 to 1100 °C owing to a suitable combination of active moieties and a well-formed carbon matrix [70,74,75]. However, optimizing these synthesis conditions is highly individual and must be done separately for each set of precursors.

4.2.3. Improving porosity

Next to intrinsic activity, the second critical property of a catalyst is porosity. For clarity, the IUPAC definition of pore sizes [76] consisting of micropores (below 2 nm), mesopores (2...50 nm), and macropores (above 50 nm) will be used in the present work. For NPGM catalysts, porosity has two main purposes (**Figure 6**). The first purpose, identically to conventional Pt-based catalysts, is to ensure that the mass transport of reactants and products proceeds at a sufficient rate. As a result, meso- and macroporosity are highly desired properties in fuel cell catalysts [17]. The second purpose, unique to NPGM catalysts, is

related to the active sites. In 2006, Jaouen et al. [77] examined numerous NPGM catalysts and observed that their activity is best correlated with their micropore surface area. Several years later researchers reached a conclusion that many of the most active moieties discussed in the previous section preferably form in micropores [78,79]. Additionally, increasing the *SSA* of a catalyst increases the availability of the active sites otherwise hidden deeper in the carbon matrix [80].

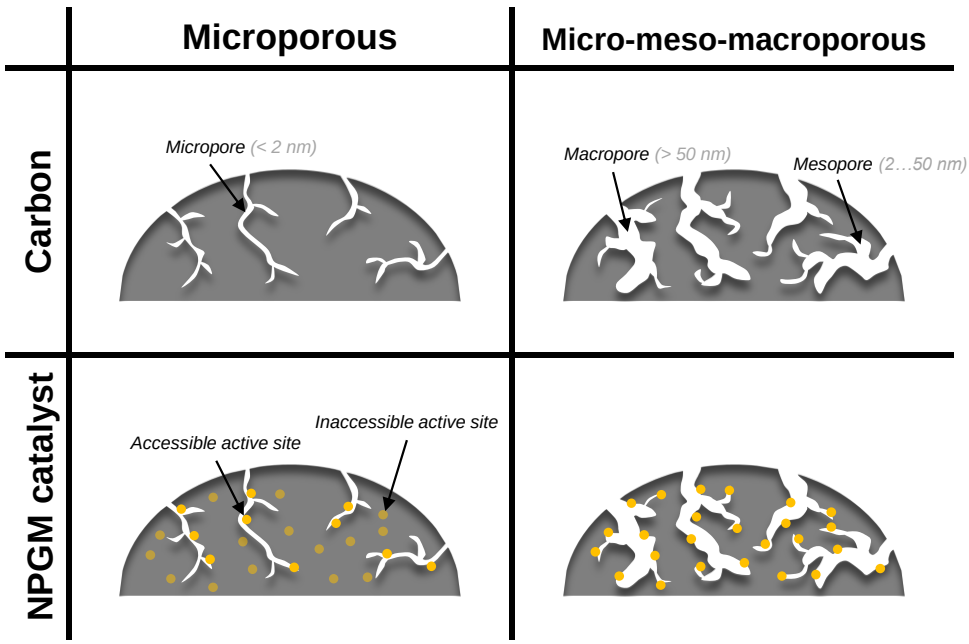

Figure 6. Graphical depictions of fully microporous (left) and micro-meso-macroporous (right) structures for pristine carbon (top) and NPGM catalysts (bottom).

A considerable amount of micropores is almost always formed when synthesizing NPGM catalysts. However, these micropores can be influenced by changing the synthesis strategy or using special pore formers [81]. For instance, a class of state-of-the-art catalysts is synthesized from a zinc-based zeolitic imidazolate framework, where the zinc is substituted by either iron or cobalt during the synthesis [72]. The result is a highly microporous carbon network with abundant active sites due to the distinct structure of the precursor.

Outside such frameworks, zinc has also garnered attention as a separate pore former in the form of $ZnCl_2$. Carbon materials intended for supercapacitors have benefited from the ability of zinc chloride to chemically activate carbon producing large quantities of micropores [82]. The specifics of the activation process have been discussed by Caturla et al. [83]. Besides activation, a specific templating effect can also be expected due to the relatively low boiling point of

$ZnCl_2$ (732 °C) [84]. Recent reports have provided preliminary evidence that using $ZnCl_2$ as a precursor enhances the activity of NPGM catalysts [80,85].

Aside from influencing the intrinsic activity, the pyrolysis step greatly affects porosity as well. The pyrolysis temperature, heating rate, and duration can be finely tuned to achieve the desired porosity [86]. Multi-step pyrolysis procedures employing multiple temperatures are also widely used [87]. In general, the issue is finding a compromise between the level of graphitization and porosity as the former increases and the latter decreases when the pyrolysis temperature is raised [88].

Another class of state-of-the-art NPGM catalysts, which we use as a reference in some parts of the study, is synthesized by combining various simple nitrogen-rich compounds, such as nicarbazin, and an iron salt and pyrolyzing the mixture [89]. Importantly, silica powders with various particle sizes are also added to the mixture to act as hard templates. As a result, catalysts with excellent meso- and macroporosity can be obtained. This approach has gained considerable traction as other workgroups use other combinations of silica or zeolites [90–93]. The main drawback of these hard templates is their silicon content requiring HF or extremely concentrated strong bases as leaching agents. Alternative hard templates which can be leached with less toxic chemicals are needed to improve the feasibility of synthesizing NPGM catalysts. While several silicon-free hard templates have been proposed for producing porous carbon materials [94,95], only a few publications report using them for the specific purpose of NPGM catalysts [96,97]. Furthermore, these catalysts are rarely studied as fuel cell cathodes, where their porosity would provide invaluable data.

Ideally, the hard template should consist of naturally abundant elements. One candidate is hydroxyapatite (HA, $Ca_{10}(PO_4)_6(OH)_2$), which is a naturally occurring mineral widely present in bones and teeth. HA has a melting point of 1100 °C [98] making it a suitable hard template where lower pyrolysis temperatures are used. Nanostructured HA with particle lengths and widths of roughly 80 nm and 20 nm, respectively, are widely used in the biomedical field owing to its similarity to the HA present in human bones [99,100]. Based on these factors, we hypothesize that HA can be used as a hard template to produce NPGM catalysts with abundant meso- and macropores. This unique porous network is a critical factor for achieving high performance in a fuel cell.

4.2.4. Measuring the performance of NPGM catalysts

Studying the performance of a novel NPGM catalyst typically follows a straightforward route consisting of two main electrochemical analysis methods. Firstly, the intrinsic activity of a novel catalyst is screened with the rotating disc electrode (RDE) or rotating ring disc electrode (RRDE) methods which observe the behavior of the catalyst in acidic or alkaline electrolyte solutions using three-electrode experimental setups (**Figure 7**).

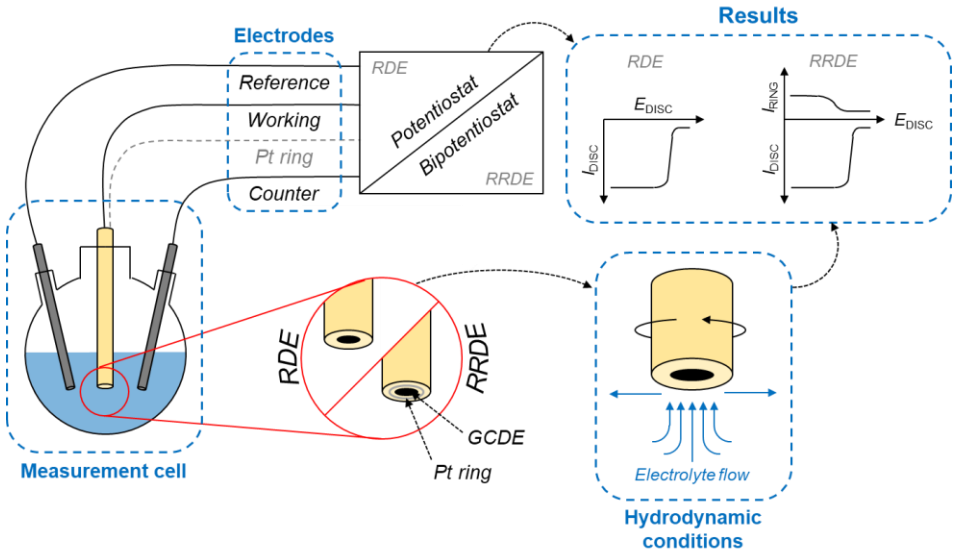

Figure 7. Graphical depictions of RDE and RRDE measurement setups and their general principles.

Both these methods revolve around a cylindrical electrode which is coated with a catalyst and then inserted into an electrochemical measurement cell containing an electrolyte solution [101]. The cylindrical electrode can be made from a variety of different materials. In ORR measurements, the material of choice is often glassy carbon resulting in a glassy carbon disc electrode (GCDE). A potential (E) where no electrochemical processes occur is then applied between the catalyst-coated GCDE, i.e., the working electrode (WE), and a reference electrode. Next, the potential is scanned at a fixed scan rate towards lower values until the ORR starts, i.e., the absolute current measured between the WE and a counter electrode increases. At this stage, it is mandatory to account for the current produced by charged electrolyte particles moving in the electric field, i.e., the background current. Depending on how soon the ORR starts occurring, a preliminary decision can be made regarding the intrinsic activity of a catalyst. Concurrently to the electrical measurements, the WE is rotated at fixed rotation rates to establish specific hydrodynamic conditions near the WE. The result is an ORR polarization curve with a distinct shape as depicted in **Figure 7**.

Many parameters can be extracted from the polarization curve to compare various catalysts to each other. The most common parameters are the onset potential (E_{onset}) defined as the WE potential at a current density (j) of -0.1 mA cm^{-2}, and the half-wave potential ($E_{1/2}$) defined as the WE potential at a current density value corresponding to half of the current density value at the diffusion-limited region. For catalysts with sufficient activity, a more detailed parameter can be calculated called mass activity (MA) at 0.9 V vs. RHE, which

is obtained by dividing the current density at 0.9 V vs. RHE by the catalyst loading. Obtaining polarization curves at various rotation rates is central to the Koutecký-Levich analysis which gives information about the number of electrons ($n_{K\text{-}L}$) participating in the ORR (discussed in 4.2.2.) [102]. The value of $n_{K\text{-}L}$ can be calculated according to Formula 1:

$$\frac{1}{I} = \frac{1}{I_k} + \frac{1}{I_d} = \frac{1}{I_k} + \frac{1}{0.62 * n_{K\text{-}L} * F * S * D^{\frac{2}{3}} * \nu^{-\frac{1}{6}} * C} * \omega^{-\frac{1}{2}}, \quad [1]$$

where I, I_k, and I_d are the measured, kinetic, and diffusion-limited currents, respectively, F is the Faraday constant, S is the electrode area, D and v are the diffusion coefficient and kinematic viscosity of the solution, respectively, C is the concentration of oxygen in the solution, and ω is the rotation rate. Since all variables besides $n_{K\text{-}L}$ have known values, the value of $n_{K\text{-}L}$ can be extracted from the slope of an I^{-1} vs. $\omega^{-1/2}$ plot.

A more direct way of investigating the number of participating electrons is the RRDE method where the WE is additionally surrounded by a Pt ring electrode [103]. The measurement proceeds similarly to the description above but with a separate fixed potential applied to the Pt ring. As a result, the hydrogen peroxide produced by the catalyst which is not reduced further and escapes the catalyst layer is oxidized at the Pt ring electrode. Therefore, the magnitude of the current gives direct information about the number of electrons participating in the ORR. The fact that some of the produced hydrogen peroxide bypasses the Pt ring electrode and escapes into the bulk electrolyte solution is accounted for by the collection efficiency of the Pt ring electrode. As a result, the peroxide yield ($x\ H_2O_2$), which is inversely correlated to the number of participating electrons, can be calculated according to Formula 2 [104]:

$$x\ H_2O_2 = \frac{200 * \frac{I_{ring}}{I_{disc}}}{N + \frac{I_{ring}}{I_{disc}}}, \quad [2]$$

where I_{disc} and I_{ring} are the disc and ring currents, respectively, and N is the collection efficiency.

In acidic conditions, reaching the benchmark set by platinum is an extremely difficult task. Currently, the best NPGM catalysts exhibit E_{onset} values upwards of 0.98 V vs. RHE [73,105,106], while conventional Pt-based catalysts exhibit current values higher than the −0.1 mA cm^{-2} defined for finding E_{onset} values already at 1.0 V vs. RHE [107]. In contrast, several workgroups have demonstrated NPGM catalysts with activity more comparable to platinum in alkaline conditions. Here, E_{onset} values near 1.00 V vs. RHE have been demonstrated by several research groups [108–111]. However, it is crucial to consider that these excellent results have been obtained with NPGM catalyst loadings several factors higher than what is used for Pt-based catalysts.

While RDE and RRDE are well-established methods for obtaining invaluable information about the intrinsic activity of a catalyst, the obtained results are not necessarily indicative of performance in a fuel cell where porosity is a far more critical parameter. A recent publication has clearly demonstrated that relying only on R(R)DE when investigating novel catalysts may lead to erroneous conclusions [112]. Thus, the most promising catalysts need to be studied as cathodes in two-electrode fuel cell setups to analyze how they perform in conditions more comparable to practical applications.

Contrary to R(R)DE, two-electrode fuel cell experiments are much more complex (**Figure 8**). Preparing the catalyst into an MEA is a more intricate process than coating a GCDE and in the measurement itself there are a significantly larger number of parameters that need to be considered. Fabricating an MEA can be done by two routes [113]. The first involves coating the catalyst directly onto the membrane resulting in a catalyst-coated membrane (CCM). In the second route, the catalyst is coated onto a GDL resulting in a gas diffusion electrode (GDE). A membrane is then inserted between the two GDEs and the structure is usually hot-pressed together to ensure sufficient contact between the catalyst layers and the membrane. The GDE route is more commonly used for NPGM catalysts because large catalyst loadings upwards of 4.0 mg cm^{-2} are needed for satisfactory performance [114]. Thick catalyst layers require substrates with sufficient mechanical stiffness which the thin membrane cannot provide.

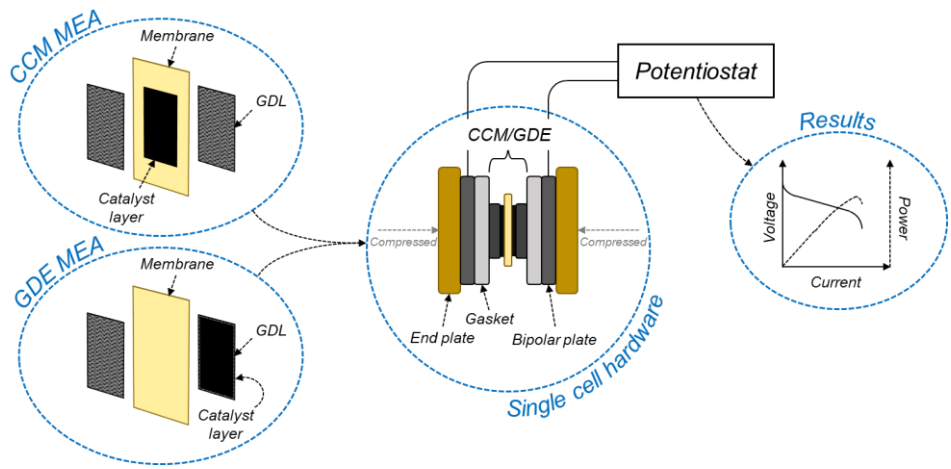

Figure 8. A simplified schematic of a two-electrode fuel cell measurement setup.

The MEA is inserted alongside other components (mentioned in section 4.1.2) into a single cell hardware which is connected to the required measurement devices. H_2 and O_2 are then supplied to the anode and cathode, respectively, resulting in a specific voltage (U) between the electrodes known as the open-circuit voltage. As current is drawn from the cell through an external circuit, the

voltage drops considerably due to kinetic losses. After overcoming the initial drop, the voltage decreases at a slower rate as ohmic losses related to the transport of electrons and ions dictate the behavior of the cell. The influence of a third type of voltage loss related to the transport of reactants and products known as mass transport losses becomes a more critical factor the larger the drawn current. Ultimately, the voltage of the cell drops rapidly once a certain current is reached as the cell cannot support faster mass transport. The result is a climbing power-current density curve (P, j) which drops off after reaching a maximum value known as the peak power density (*PPD*).

Optimizing the operating conditions of a fuel cell, i.e., cell temperature, gas flow rates, gas humidification degrees, and gas pressures, is critically important to minimize the voltage losses stemming from suboptimal transport of electrons, ions, reactants, and product [19]. The transport of these species severely depends on the management of water inside the cell. Too little water will dry out the membrane and ionomer leading to restricted ionic conductivity. Too much water will flood the cell blocking the formation of TPBs needed for the electrochemical reactions to occur. Carefully managing the amount of water and its locality inside the cell is the subject of many recent fuel cell studies, especially regarding AEMFCs [115–117].

In fuel cell experiments, obtaining results comparable to platinum is a much more difficult task in both acidic and alkaline conditions in comparison to R(R)DE experiments. Even state-of-the-art NPGM catalysts exhibit considerably lower performance than conventional platinum catalysts [118]. An excellent example of this was demonstrated by Akula et al. [55] who studied several state-of-the-art NPGM catalysts in both RDE and fuel cell experiments. In their study, the best NPGM catalyst exhibited an $E_{1/2}$ value only 40 mV lower than a conventional platinum-based catalyst in RDE testing. In a PEMFC test, however, the NPGM catalyst was competitive with the Pt-based catalyst only at very low overpotentials. Major differences in performances appeared once more current was drawn from the cells leading to a *PPD* value of 837 mW cm^{-2} for the NPGM catalyst compared to >1000 mW cm^{-2} (data cut off before reaching true *PPD*) for the Pt catalyst. In contrast, a similar state-of-the art NPGM catalyst exhibited a *PPD* value of 2050 mW cm^{-2} in an AEMFC test representing the highest performance to date for NPGM catalysts in fuel cells [119]. However, improvements especially regarding AEMFCs are still expected in the following years due to focused research and rising technological maturity [120].

4.3. Valorizing abundant local resources

4.3.1. Catalysts from biomass

NPGM catalysts can be synthesized from a virtually unlimited array of precursors as long as they include sources of carbon, nitrogen, and a transition metal. Many researchers turn to industrial organic chemistry to find inexpensive carbon- and nitrogen-rich compounds. Another option is to utilize naturally abundant resources as precursors. A great example of this are coconut husks, which are one of the key raw materials used to produce activated carbon [121]. The main advantages of this approach are the abundancy, extremely low-cost, and high carbon content of biomass [122]. Additionally, biomass is a remarkably flexible source as it can be converted into carbons with vastly distinct structures by modifying the synthesis strategy [123].

Biomass-derived NPGM catalysts have exhibited promising results in both R(R)DE screening tests as well as fuel cell experiments. Out of all possible biomass precursors, lignocellulosic biomass has been considered as the most accessible [124]. Lignin has been successfully used as a carbon source for synthesizing catalysts based on noble metals [125], inexpensive transition metals [126] or even no metals [127]. The feasibility of using lignin as a precursor was validated by Shen et al. [128] who achieved an excellent *PPD* value of 779 mW cm^{-2} in a PEMFC single cell test utilizing a lignin-derived catalyst.

4.3.2. Estonian peat

While active NPGM catalysts can be synthesized from basically any biomass, it is critically important to consider the availability of such resources. For example, coconut trees do not grow in Estonia and thus importing coconut husks to produce NPGM catalysts is nonsensical. Minimizing contributions to climate change through the emissions-heavy shipping industry is a part of the European Green Deal [129]. Consequently, novel materials including NPGM catalysts need to be sourced from local precursors as much as possible.

In Estonia, a potential biomass material is peat which is "…the second most attractive and mined natural resource after oil shale (in Estonia)" according to the Estonian Peat Association [130]. Peat is an accumulation of decayed organic matter (**Figure 9a**) covering roughly 22.3% of the total landmass of Estonia [15]. Similarly to other plants, peat is mainly composed of lignin and cellulose [131] leading to a cellular structure common for organic matter (**Figure 9b**).

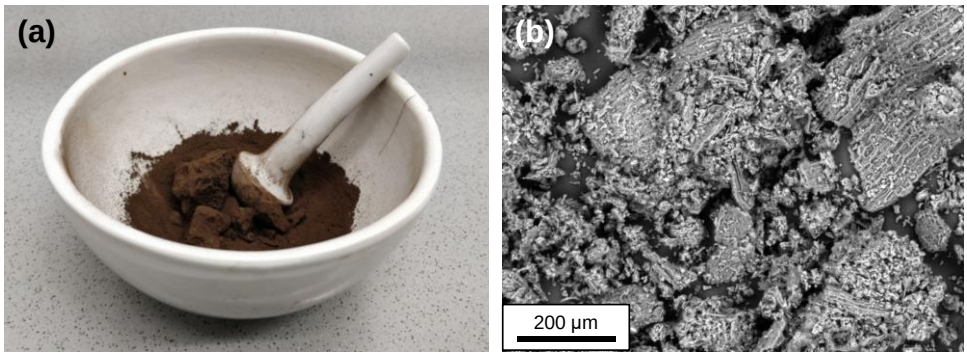

Figure 9. (a) Blended and dried peat in the middle of pulverization. (b) Scanning electron microscopy image of peat.

Peatlands can be loosely categorized as pristine and drained peatlands. While pristine peatlands are carbon sinks, drained peatlands can ultimately become net carbon emitters of CO_2 and CH_4 as the peat starts decomposing more rapidly [132]. Unfortunately, a large amount (~65%) of the peatlands in Estonia have been drained and destroyed as the result of human activities [133]. These peatlands have to be either restored by re-wetting [134] or the peat utilized [135].

At the present time, peat is mainly utilized in horticulture and as a source of heat [15]. The former application requires lightly decomposed peat while well-decomposed peat can only be used in the latter application. The well-decomposed peat could instead be converted into a significantly more valuable product in the form of an advanced functional material for electrochemical devices. Our research group has recently demonstrated the feasibility of this idea in the field of supercapacitors [136] and batteries [137]. Therefore, we hypothesize that well-decomposed peat can also be converted into highly active NPGM catalysts. The knowledge gained in this study can be used to develop a value-added product opening up the exponentially increasing market of fuel cells for peat [16]. Currently, 573 million tons of peat deposits are available for industrial mining in Estonia alone [130].

5. RESEARCH AIM AND HYPOTHESES

Stemming from the discussion above, the widespread adoption of fuel cells requires developing replacements to conventional platinum-based catalysts that exhibit sufficiently high intrinsic activity as well as porosity and are produced from inexpensive resources. As a result, a general **research aim** was framed for this thesis:

- Develop novel non-platinum group metal oxygen reduction catalysts with high intrinsic activity and superior porosity by valorizing naturally abundant local resources.

The research aim was used as a guiding principle to direct this study towards a more focused target which was formulated into a **hypothesis**:

- Abundant Estonian peat can be converted into active non-platinum group metal oxygen reduction catalysts with superior porosity and excellent fuel cell performance using a suitable synthesis strategy.

6. EXPERIMENTAL

6.1. Synthesis of peat-derived carbon catalysts

The peat used in this work was obtained from a nearby peatland (Möllatsi, Estonia). Before further processing, the peat was pre-treated by mixing it with water and homogenizing in a blender. The mixture was dried and pulverized with a mortar and pestle. Modifying the peat into NPGM catalysts proceeded through pathway #1 and pathway #2 in publications I-III and IV, respectively.

Pathway #1 consisted of first carbonizing the peat into carbon support materials under various conditions and then activating the peat-derived carbon (PDC) support materials with cobalt and nitrogen. The carbonization procedures can be classified into three groups: direct carbonization, chemical activation, and multi-step pyrolysis. In the direct carbonization, the peat was pyrolyzed for 3 h at 800 °C in a flow of Ar (AGA, 99.999%, 200 ml min^{-1}) resulting in a carbon yield of roughly 35% and a material denoted as **PDC-1**. In the chemical activation step group, the peat was mixed with one of three activator compounds, KOH, $ZnCl_2$ or $FeCl_3$ (1:4 ratio of peat:activator by weight), pyrolyzed for 2 h at 700 °C in a flow of Ar and washed with 1 M HCl to obtain **PDC-2**, **PDC-3**, and **PDC-4**, respectively, depending on the used activator. In the multi-step pyrolysis group, the peat was first pyrolyzed for 3 h at 450 °C in Ar, then washed with 20 wt% KOH and 50 wt% HCl solutions to obtain **PDC-5**. The powder was pyrolyzed a second time for 2 h at 1000 °C in Ar to obtain **PDC-6**.

The PDCs were then modified with cobalt and nitrogen through a dry ball-milling method by mixing 300 mg of a PDC with 74 mg of $Co(NO_3)_3 \cdot 6H_2O$ (Sigma-Aldrich, ≥99.0%) and 80 mg of 2,2'-bipyridine (Sigma-Aldrich, ReagentPlus®, ≥99%). The mixture was ball-milled (FRITSCH Pulverisette 6) in a zirconia crucible containing 5 zirconia balls (20 mm diameter) for 2 h at 300 rpm. Finally, the powder was pyrolyzed for 1.5 h at 800 °C in Ar to obtain NPGM catalysts denoted as **Co-N/PDC-x**, where x is determined by which of the PDCs obtained in the previous paragraph was used as the carbon support. An overview of the main synthesis conditions of the materials acquired through pathway #1 and their designations in publications I–III are given below in **Table 1**.

Table 1. A summary of the main synthesis conditions used for the PDCs and the designations of the PDCs and PDC catalysts in publications [I–III].

PDC						PDC catalyst	
Designation in text	Designations in publications	Activating agent	Pyrolysis	Washing	2nd pyrolysis	Designation in text	Designations in publications
PDC-1	PDC [I] C-1 [II]	-	800 °C	-	-	Co-N/PDC-1	Co-N/PDC [I] Co-N/C-1 [II] PDCC_HT [III]
PDC-2	C-2(KOH) [II]	KOH	700 °C	HCl	-	Co-N/PDC-2	Co-N/C-2(KOH) [II]
PDC-3	C-2($ZnCl_2$) [II]	$ZnCl_2$	700 °C	HCl	-	Co-N/PDC-3	Co-N/C-2($ZnCl_2$) [II] PDCC_$ZnCl_2$ [III]
PDC-4	-	$FeCl_3$	700 °C	HCl	-	Co-N/PDC-4	PDCC_$FeCl_3$ [III]
PDC-5	C-3 [II]	-	450 °C	KOH HCl	-	Co-N/PDC-5	Co-N/C-3 [II]
PDC-6	C-3(pyr) [II]	-	450 °C	KOH HCl	1000 °C	Co-N/PDC-6	Co-N/C-3(pyr) [II] PDCC_W [III]

Note: Roman numerals in square brackets indicate publication.

Pathway #2 consisted of carbonizing the peat together with the metal and nitrogen sources to directly embed the active sites into the carbon matrix. The baseline catalyst, denoted as **Fe-N-PDC-1**, was obtained by mixing 3 g of peat with 1 g of guanidine carbonate (Sigma-Aldrich, 99%), 0.1 g of $Fe(NO_3)_3 \cdot 9H_2O$ (ACS reagent, Sigma-Aldrich, ≥98%), and 2 g of $ZnCl_2$ (anhydrous, ACS reagent, Sigma-Aldrich, ≥97%). A step-by-step mixing procedure consisting of ball-milling (15 min grinding cycles, 25 WC balls with a diameter of 10 mm, FRITSCH Pulverisette 6), mixing with a high-shear mixer (S10N-10G dispersing tool, IKA), and sonicating for 30 min, 1 h, and 30 min, respectively, was used to homogenize the mixture. In contrast to the previous ball-milling procedure used for the pathway #1 catalysts, isopropyl alcohol (IPA, 99.0%, Sigma-Aldrich) was also added to the dry mixture to enhance the efficiency of the milling step. After drying the mixture overnight at 80 °C, the powder was pyrolyzed for 1 h at 800 °C in Ar followed by washing with 1 M HNO_3 for 8 h at 80 °C and a final pyrolysis conducted at identical conditions to the first pyrolysis. **Fe-N-PDC-2** and **Fe-N-PDC-3** were synthesized analogously but with a doubled amount of either the Fe precursor or $ZnCl_2$, respectively. The next two catalysts were synthesized by taking Fe-N-PDC-3 as a new baseline, but with elevated pyrolysis temperatures of 900 °C and 1000 °C for **Fe-N-PDC-4** and **Fe-N-PDC-5**, respectively.

The final catalyst, **Fe-N-PDC-6**, was synthesized using a doubled amount of both Fe precursor and $ZnCl_2$ and a pyrolysis temperature of 1000 °C with the inclusion of 4 g of acicular hydroxyapatite (HA, $Ca_{10}(PO_4)_6(OH)_2$, ≥96%, 60±10 nm particle size, Sigma-Aldrich) before the homogenization step as a hard template. The ball-milling was conducted in a zirconia crucible with 250 zirconia balls with a diameter of 5 mm to avoid contamination with WC. An overview of the main synthesis conditions of the catalysts obtained through pathway #2 and their designations in publication IV are given below in **Table 2**.

A state-of-the-art NPGM catalyst material (PMF-12704, Pajarito Powder) denoted as Fe-N-C-comm was used as a reference.

Table 2. A summary of the main synthesis parameters used for the PDC catalysts and their designations in the text and in publication [IV].

Designation in text and in publication	Precursors / g					Pyrolysis temperature
	Peat	Guanidine carbonate	$Fe(NO_3)_3 \cdot 9H_2O$	$ZnCl_2$	Hydroxyapatite	
Fe-N-PDC-1 [IV]	3	1	0.1	2	-	800 °C
Fe-N-PDC-2 [IV]	3	1	0.2	2	-	800 °C
Fe-N-PDC-3 [IV]	3	1	0.1	4	-	800 °C
Fe-N-PDC-4 [IV]	3	1	0.1	4	-	900 °C
Fe-N-PDC-5 [IV]	3	1	0.1	4	-	1000 °C
Fe-N-PDC-HA [IV]	3	1	0.2	4	4	1000 °C

Note: Roman numerals in square brackets indicate publication.

6.2. Physical characterization methods

A wide array of physical characterization methods was used to analyze the various properties of the synthesized materials.

- High-resolution scanning electron microscopy (HR-SEM) measurements [I-IV] were performed with a Zeiss Merlin microscope by depositing the samples onto a copper sample holder covered with carbon tape. SEM energy-dispersive X-ray spectroscopy (SEM-EDS) [I-IV] were performed with a Bruker EDX-XFlash® 6/30 detector. Accelerating voltages of 2 kV and 8 kV were used for the HR-SEM and SEM-EDS measurements, respectively. The elemental compositions of the samples were obtained using a P/B-ZAF standardless mode.
- Transmission electron microscopy (TEM) measurements [I-IV] were performed with a JEOL JEM-2100 microscope utilizing a working voltage of 200 kV.
- Low-temperature sorption measurements were performed with Micromeritics ASAP 2020 and 3Flex devices using nitrogen [I-IV] and argon [III] as the gas probes at the boiling temperatures of nitrogen (-195.8 °C) and argon (-185.8 °C), respectively. The specific surface area values were calculated according to the Brunauer-Emmett-Teller multipoint theory (S_{BET}) and the pore volume values (V_{TOT}) were calculated from the isotherm data at a relative pressure of 0.95. Specific surface area (S_{DFT}) and pore volume (V_{DFT}) values were also extracted from the pore size distribution data calculated according to the two-dimensional non-local density functional theory for carbon materials with a heterogeneous surface (2D-NLDFT-HS) using SAIEUS software.
- Mercury intrusion porosimetry measurements [IV] were performed with a Micromeritics AutoPore IV device in the pressure range from 0.01 to 410 MPa.
- Laser diffraction measurements [III, IV] were performed with a Microtrac BLUEWAVE particle size analyzer by suspending the samples in IPA and sonicating the mixture for 15 min.
- X-ray diffraction (XRD) measurements [I-IV] were performed with a Bruker D8 Advanced diffractometer using a Ni filtered Cu Kα X-ray source with a wavelength of 1.5406 Å. Data analysis was performed with Topas software.
- X-ray photoelectron spectroscopy (XPS) measurements were performed with a SCIENTA SES 100 spectrometer equipped with a Thermo XR3E2 X-ray tube [I-III] and a Thermo Scientific Nexsa system [IV]. Data analysis was performed with Casa XPS [I-III] and SPANCF [IV] softwares.
- X-ray absorption spectroscopy (XAS) measurements [IV] were performed at the FinEstBeAMS beamline at the MaxIV synchrotron using a total electron yield mode.
- Raman spectroscopy measurements [I, II] were performed with a Renishaw inVia spectrometer using a 514 nm laser line. Data analysis was performed with OriginPro 2016 software.

6.3. Electrochemical activity screening

In publications I-III, the rotating disc electrode (RDE) method was used to screen the activity of the synthesized carbon materials. The materials were prepared into suspensions by mixing a carbon powder with IPA, Milli-Q® water, and Nafion™ ionomer (D521 dispersion, Ion Power) in a cooled ultrasonic bath for 1 h. The suspensions (1:4 ratio of IPA:water by weight, 1:3 ratio of ionomer:catalyst by weight) were drop-casted in one 9 µl aliquot onto glassy carbon disc electrodes (GCDE, 5 mm diameter), which were polished beforehand with an alumina slurry (MicroPolish™ Alumina, 0.3 µm, Buehler), resulting in target catalyst loadings of 0.8 mg cm^{-2}. Prior to the measurements, all the required glassware were washed with a mixture of H_2SO_4 and H_2O_2 heated to 80 °C and then rinsed with deionized water and Milli-Q® water. The 0.1 M acidic [II] and alkaline [I, III, IV] working solutions were prepared from 67-72% $HClO_4$ (Sigma-Aldrich) and KOH pellets (99.99%, Sigma-Aldrich). A three-electrode setup consisting of a GCDE coated with the catalyst as the working electrode, a carbon rod as the counter electrode, and a different reference electrode depending on the electrolyte solution (saturated calomel electrode [II], Hg/HgO/0.1 M KOH [I, III] or reversible hydrogen electrode (RHE) [IV]. All measured potentials were converted to the RHE scale.

The measurements were performed with a Pine Instrumental Company rotator and a Gamry Instruments Reference 600™ potentiostat controlled with Gamry Instruments Framework software. As a first step, the RDE was conditioned by scanning in a potential range from 1.2 to 0.25 V vs. RHE at a potential scan rate of 10 mV s^{-1} for 15 cycles. The polarization curves were measured in an O_2-saturated solution at a potential scan rate of 10 mV s^{-1} at electrode rotation rates ranging from 500 to 3000 rpm. The measured current values were corrected with the background current values and against the ohmic drop by using the electrolyte resistance value determined with electrochemical impedance spectroscopy to obtain the corrected current density values (j_c).

In publication IV, the rotating ring disc electrode (RRDE) method was used to screen the activity and selectivity of the synthesized catalysts otherwise identically to the method described above but with a few differences. The catalysts were prepared into suspensions similarly but in a more diluted manner resulting in lower target catalyst loadings of 0.3 mg cm^{-2}. Additionally, the RRDE (5 mm diameter) was coated by drop-casting the suspension in three 3 µl aliquots. The measurements were conducted with a Pine rotator and a Metrohm Autolab PGSTAT302 potentiostat equipped with a BA module and Nova 1.11 software. Prior to measuring every polarization curve, the Pt ring was activated by scanning from 1.4 to 0.025 V vs. RHE at a potential scan rate of 50 mV s^{-1} for 20 cycles. During the measurements, the Pt ring was held at a constant potential of 1.2 V vs. RHE. Formula 2 was used to calculate the hydrogen peroxide yield from the acquired measurement data with a collection efficiency of 0.249 determined previously.

6.4. Fuel cell experiments

The PEMFC measurements [II] were performed by first preparing the catalysts into gas diffusion electrodes (GDE). The cathode GDEs were fabricated by drop-casting the catalyst suspensions onto gas diffusion layers (GDL, Sigracet 25 BC, FuelCellStore) in 200 µl aliquots until a catalyst loading of 4.0±0.1 mg cm^{-2} was reached. The suspensions were prepared according to the procedure described above but with an ionomer to catalyst ratio of 1.75:1. Between aliquots, the suspensions were allowed to dry in ambient conditions. The anode GDEs with a catalyst loading of 1.0±0.1 mg cm^{-2} were fabricated by coating 60 wt% Pt/Vulcan (FuelCellStore) onto GDLs (Sigracet 25 BC, FuelCellStore) with an ultrasonic spray coating method [138]. The GDEs were hot-pressed together with a PEM (Nafion™ HP, FuelCellStore) at 135 °C for 2 min utilizing a pressure of 4.9 MPa resulting in an MEA with an active area of 5 cm^2. The MEAs were inserted into a single cell measurement hardware which was connected to a potentiostat (PGSTAT302N, BOOSTER20A, Autolab, Metrohm) and a humidification system (Fuel Cell Technologies Inc.). Fully prehumidified O_2 and H_2 were directed to the cathode and anode, respectively, at a flow rate of 200 ml min^{-1} and a backpressure of 100 kPa. The polarization curves were measured galvanostatically at a cell temperature of 80 °C by increasing the current density in 40 mA cm^{-2} steps at 1 min intervals.

The AEMFC measurements were performed according to two different procedures. In publication [III], the catalysts were prepared into suspensions as per previous instruction but with an anion exchange ionomer (Fumion FAA-3-SOLUT-10, FuMA-Tech, FuelCellStore) instead of a Nafion™ ionomer, an ionomer to carbon ratio of 0.9:1, and an additional 1 h of mechanical mixing before the sonication step. The suspensions were drop-casted onto 5 cm^2 GDLs (Freudenberg H23C3, FuelCellStore) heated to 50 °C until a cathode catalyst loading of 4.0±0.1 mg cm^{-2} was reached. The anodes with a catalyst loading of 0.67±0.1 mg cm^{-2} were fabricated via the CCM method by spray-coating an AEM (FAA-3-50, FuMA-Tech, FuelCellStore) with a commercial PtRu catalyst (60% PtRu on Ketjenblack EC-300J, FuelCellStore) according to a previously published guideline [139]. The components were then submerged in a 1 M KOH solution overnight converting the membrane and ionomer into the hydroxide-conducting form. After rinsing the components with Milli-Q® water, they were assembled in a single cell measurement hardware and connected to the same measurement station described above. O_2 and H_2 were humidified at 58 °C and directed to the cell at a flow rate of 50 ml min^{-1}. The polarization curves were measured galvanostatically at a cell temperature of 60 °C by increasing the current density in 20 mA cm^{-2} steps at 15 s intervals.

In publication [IV], the GDEs were prepared using a procedure adapted from a method developed by Mustain et al. [108,140]. The cathode catalyst suspensions were prepared by pestling 563 µl of ionomer (Pention-D34-5wt%, FuelCellStore) and 12.23 mg of polytetrafluoroethylene (PTFE, Ultraflon MP-25, FuelCellStore) in a mortar for 10 min to break up the larger agglomerates.

Then, 75 mg of an NPGM catalyst and 37.5 mg of non-catalyzed carbon (Vulcan XC-72R, FuelCellStore) were added to the mixture and pestled for an additional 10 min to incorporate the ionomer and PTFE into the catalyst and carbon powder. Finally, 0.5 ml of Milli-Q® water and 3.25 ml of IPA were pestled together with the mixture until a homogeneous suspension was reached. The suspension was sonicated in a cooled ultrasonic bath for 1 h and then spray-coated onto GDLs (Toray TGP-H-060, FuelCellStore) heated to 50 °C using a Hansa 681 airbrush. The anode GDEs were prepared analogously but with 900 µl of ionomer (Pention-D72-5wt%, FuelCellStore), 12 mg of PTFE, 150 mg of a PtRu catalyst (60% PtRu on Ketjenblack EC300-J, FuelCellStore), 75 mg of non-catalyzed carbon, 1 ml of Milli-Q® water, and 9 ml of IPA. The target catalyst loadings for both the cathode and anode GDEs were 1.0±0.1 mg cm^{-2}. The GDEs with an active area of 5 cm^2 and an AEM (Xion AEM-Pention-72-15CL-20um, Xergy Inc., FuelCellStore) affixed between PTFE subgaskets were hydrated in Milli-Q® water for 20 min. The components were then transferred to a 1 M KOH solution, which was refreshed every 20 min, for a total of 1 h. After the membrane and ionomer were converted to the hydroxide-conducting form, the components were assembled in a single cell measurement hardware with suitable PTFE gaskets resulting in a cell compression of 20-30%. The cell was connected to the measurement station described above. O_2 and H_2 were humidified at temperatures separately optimized during the measurement process [119] and directed to the cell at flow rates of 1000 and 500 ml min^{-1}, respectively. The polarization curves were measured at a potential scan rate of 10 mV s^{-1} at cell temperatures of 65 °C and 80 °C.

7. RESULTS AND DISCUSSION

7.1. Peat-derived carbon as a catalyst support

The first peat-derived carbon support, PDC-1 [I, II], was obtained by simply carbonizing the peat at a temperature of 800 °C without any additional treatment. A simple and straightforward carbonization procedure was chosen for the first test to get a general overview of the feasibility of using peat as a carbon source. The carbonization yielded a PDC which consisted of large grains and exhibited moderate microporosity with limited mesoporosity (**Figure 10a**). Additionally, it was clear that without acid-leaching any PDC will contain a significant amount of calcium in the form of portlandite ($Ca(OH)_2$), which is also visible on the carbon grains, and a plethora of other impurities (**Figure 10b**). These elements are naturally present in peat and are thus expected additives [141]. In an RDE experiment conducted in acidic media, the PDC exhibited a surprisingly high E_{onset} value of 0.59 V vs. RHE (analyzed in the next section). These results strongly suggested that while peat is worthy of further study the carbonization procedure needs to be focused on to obtain PDCs with more suitable properties.

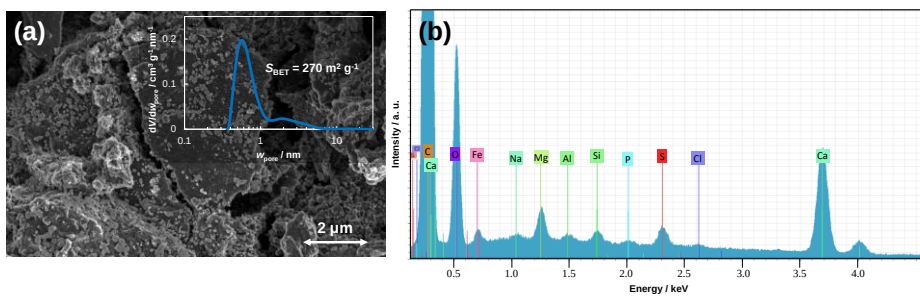

Figure 10. (a) HR-SEM image, (a inset) pore size distribution, and (b) SEM-EDS spectra for PDC-1.

7.1.1. Modifying the properties of peat-derived carbon

Continuing the analysis, several PDCs with widely different morphological and structural characteristics were synthesized with two main carbonization strategies in addition to the basic procedure used in the previous section [II]. The first additional method involved using chemical activation via either KOH, $ZnCl_2$, or $FeCl_3$ at 700 °C to enhance the porosity of the resulting PDCs. The second method utilized a multi-step pyrolysis procedure involving an initial pyrolysis at 450 °C to form a crude carbon network and a second pyrolysis at 1000 °C to fully carbonize the structure.

The pristine PDCs were first subjected to rigorous analysis with various physical characterization methods. While noticeable differences can be observed between all the PDCs, the most distinct structure was obtained with KOH as an activating agent (**Figure 11a, b**). KOH reacts directly with the carbon leading to a sponge-like structure, which has been noted in the synthesis of other carbon materials as well [82]. Distinct differences in the microstructure of the PDCs were detected using Raman spectroscopy (**Figure 11c**). According to the D band and G band intensity ratio (I_D/I_G) and the width of the D band obtained by fitting the data, there is a clear correlation between the pyrolysis temperature and the graphitization degree of the PDCs. More specifically, a higher pyrolysis temperature yields carbons with higher I_D/I_G and smaller D band width values indicating more extensive graphitization. Only PDC-6 exhibited an abnormal graphitization degree despite a higher pyrolysis temperature of 1000 °C compared to the 700 °C and 800 °C used to pyrolyze the more graphitic PDCs. This can be attributed to the multi-step nature of the pyrolysis procedure used for PDC-6 where the initial pyrolysis at 450 °C formed local graphitic domains [137] and the second pyrolysis at 1000 °C managed to only reorganize the existing graphitic domains.

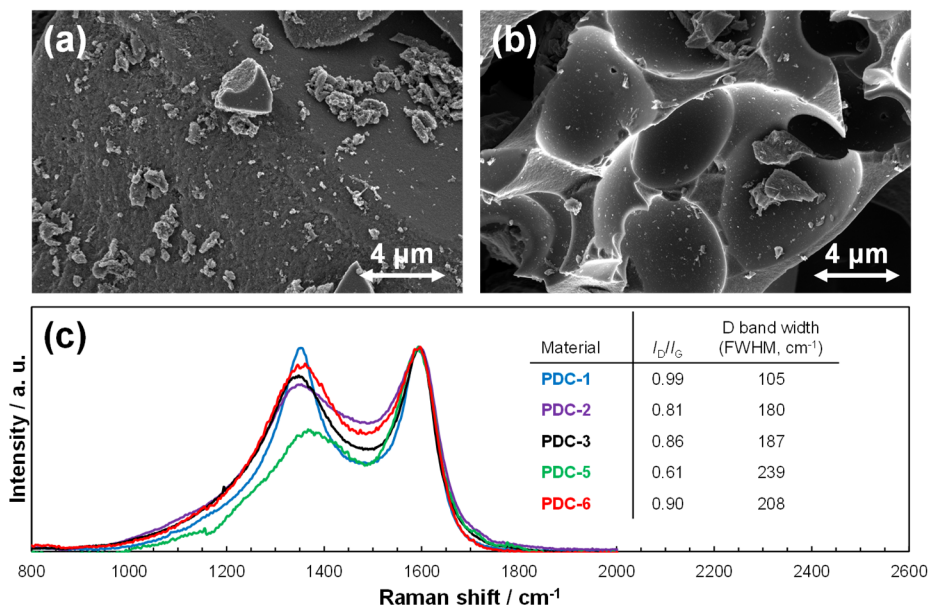

Figure 11. HR-SEM images for (a) PDC-3 and (b) PDC-2. (c) Raman spectra and (inset) D and G band fitting results for the PDCs.

The synthesized PDCs exhibited widely different porosities ranging from 7 $m^2 g^{-1}$ for PDC-5 to 2450 $m^2 g^{-1}$ for the KOH-activated PDC-2 (**Figure 12**). In general, the pore-generating effect of the activating agents was confirmed in

the case of the PDCs illustrated by their larger S_{BET} values. Additionally, using $ZnCl_2$ as the activating agent specifically yielded a PDC (PDC-3) with a considerable degree of mesoporosity as indicated by the V_{MICRO}/V_{DFT} value, which describes the proportion of micropore volume (pores with widths up to 2 nm) out of the total volume of pores with widths up to 30 nm. As a side note, this parameter will be used to describe the micro- or mesoporosity of the following peat-based materials as well. Accordingly, carbonizing peat should involve an activating agent if high porosity is desired. Importantly, the issue of impurities was largely solved by including a leaching step in the synthesis as the Ca content was reduced below the limits of detection of the SEM-EDS and XPS methods [II].

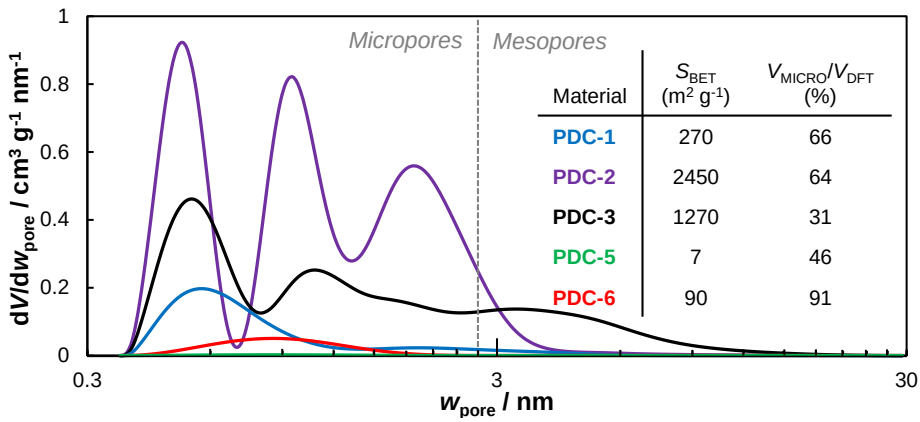

Figure 12. Pore size distributions, (inset) S_{BET}, and V_{MICRO}/V_{DFT} values for the PDCs.

All the abovementioned differences in morphological and structural characteristics emerge as majorly dissimilar electrochemical activity towards the ORR in RDE experiments conducted in acidic media (**Figure 13a**). The lowest E_{onset} value was obtained with PDC-5 most likely due to a severely underdeveloped carbon network as a result of the low pyrolysis temperature of 450 °C. Pyrolyzing this PDC a second time at a temperature of 1000 °C completed the carbonization of peat as demonstrated by the significantly higher E_{onset} value for PDC-6. A similar E_{onset} value was obtained for the KOH-activated PDC-2. In contrast, using $ZnCl_2$ as the activator (PDC-3) provided a carbon support with remarkably enhanced activity. The source of some of this activity could be related to the ~2 wt% of nitrogen present in the sample according to the SEM-EDS data. As discussed above in section 4.2.2., nitrogen atoms embedded into the carbon matrix act as active sites with performance depending on their specific configuration even without being bonded to a transition metal. However, nitrogen was also present in PDC-2 and PDC-5 which are clearly not as active as PDC-3. Therefore, the high activity of PDC-3 can most likely be attributed to structural properties caused specifically by $ZnCl_2$. An additional

measurement was conducted for PDC-1, but in a 0.1 M KOH solution (**Figure 13b**). In the alkaline environment, the PDC exhibited a much higher E_{onset} value of 0.80 V vs. RHE clearly indicating that catalyzing the ORR is simpler in alkaline than acidic media.

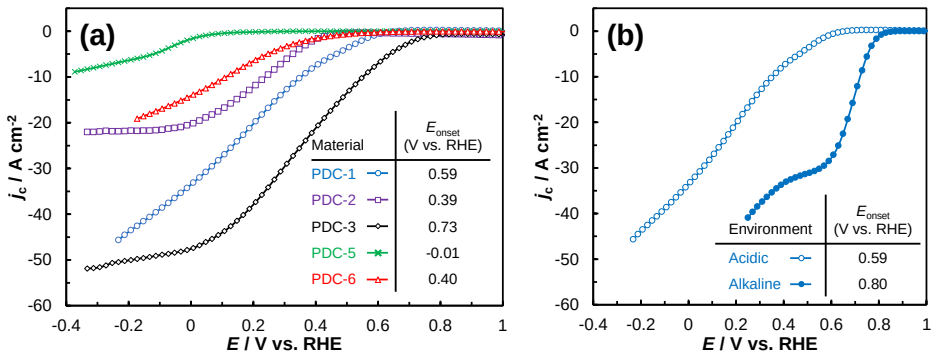

Figure 13. ORR polarization curves and (inset) E_{onset} values measured (a) for the PDCs in 0.1 M $HClO_4$ and (b) for PDC-1 in 0.1 M $HClO_4$ and 0.1 M KOH at 2000 rpm using a potential scan rate of 10 mV s^{-1}.

7.2. Synthesizing NPGM catalysts from PDCs via pathway #1

The PDCs obtained in the previous section were converted into Co-N/PDC catalysts via pathway #1 [I, II, III]. The facile synthesis procedure involved ball-milling the carbon supports with cobalt and nitrogen sources and then pyrolyzing the mixtures at 800 °C. The synthesis procedure was identical for each catalyst to study the influence of the carbon support on the final physical and electrochemical properties of the catalysts.

7.2.1. Investigating the catalysts physical properties

Modifying the PDCs with Co and N via pathway #1 lead to structures that were, in general, much more similar to each other due to the homogenization effect of the ball-milling step. For example, PDCs with both high and low porosity were ultimately converted into Co-N/PDCs with moderate porosity ranging from 240 to 590 m^2 g^{-1} (**Figure 14a**). The porosity emerged predominantly as micropores as even the high mesoporosity noted for PDC-3 (**Figure 12**) was noticeably decreased after the modification process. However, using activating agents still provided PDC catalysts with superior porosity. Raman spectroscopy measurements conducted for some PDC catalysts demonstrated that the modification process involving a pyrolysis at 800 °C produced structures that were more graphitic compared to the initial PDCs [II].

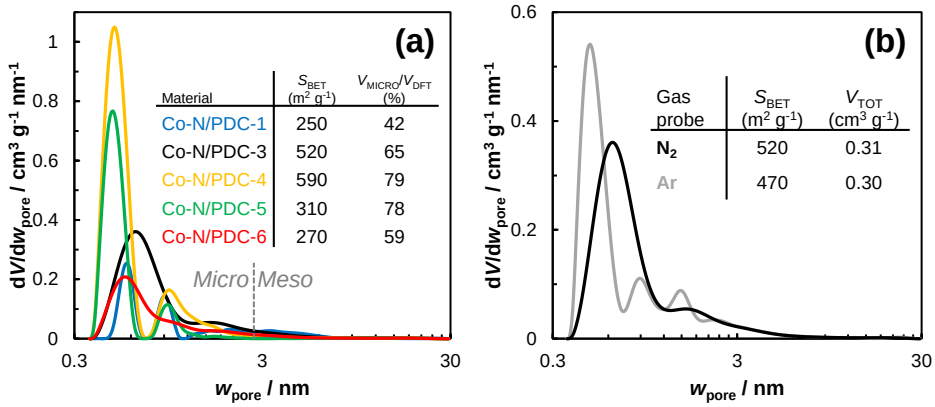

Figure 14. (a) Pore size distributions, (a inset) S_{BET}, and V_{MICRO}/V_{DFT} values for the Co-N/PDCs. (b) Pore size distributions, (b inset) S_{BET}, and V_{TOT} values for Co-N/PDC-3 measured using N_2 or Ar as the gas probe.

An important factor in the measurement of porosity with low-temperature sorption is the choice of gas probe. NPGM catalysts are usually studied with nitrogen as the gas probe due to the low cost and availability of liquid nitrogen [58]. However, nitrogen molecules might interact with the plethora of surface functionalities present in these materials leading to erroneous conclusions regarding porosity and pore size distributions [142,143]. Instead, argon is an alternative gas probe which is significantly less prone to interacting with functionalities due to not having a quadrupole moment contrary to nitrogen [76]. As a result, a number of the Co-N/PDCs were additionally analyzed with low-temperature argon sorption which, surprisingly, provided similar S_{BET} and V_{tot} values, and pore size distributions compared to the results obtained with nitrogen as the gas probe. Comparative pore size distributions and porosity characteristics are given as an example for Co-N/PDC-3 in **Figure 14b**. Therefore, nitrogen was kept as the gas probe in future measurements as the method provides sufficiently reliable porosity data.

The Co-N/PDCs were then analyzed in terms of their elemental and chemical compositions. The SEM-EDS data demonstrated that all the Co-N/PDCs contain somewhat varying amounts of cobalt and nitrogen (**Table 3**). However, the need for an acid-washing procedure was once again evident. While the SEM-EDS data confirmed that the modification procedure was successful, metallic Co and CoO particles were observed in both TEM and XRD analyses (**Figure 15**) [II]. These particles, which are encapsulated by varying numbers of carbon layers, can potentially boost the overall activity of a NPGM catalyst [144] but are typically unwanted for ORR catalysts. More specifically, such particles form at the expense of highly coveted M-N_x moieties preventing an NPGM catalyst from reaching its full potential. It has also been reported that these metallic particles are highly unstable in acidic conditions during fuel cell operation [57]. As a result, an acid-leaching step is commonly

conducted after the pyrolysis step to improve the synthesis strategy by removing these unwanted species.

Table 3. Elemental compositions (wt%) of the Co-N/PDCs measured using SEM-EDS.

Catalyst	C	O	N	Co	Ca	Other elements (<1 wt%)
Co-N/PDC-1	68	15	2.8	3.1	8.4	Si, S, Mg, Al, Cl
Co-N/PDC-2	84	6	5.8	3.0	-	Si, Cl
Co-N/PDC-3	74	14	3.4	5.9	-	Al, Cl, S
Co-N/PDC-4	70	14	4.5	3.5	-	Fe*, S
Co-N/PDC-5	78	11	5.5	4.6	-	Si, Al
Co-N/PDC-6	81	9.7	4.1	3.6	-	Si, Al, Cl

*The concentration of Fe was 8.1 wt%

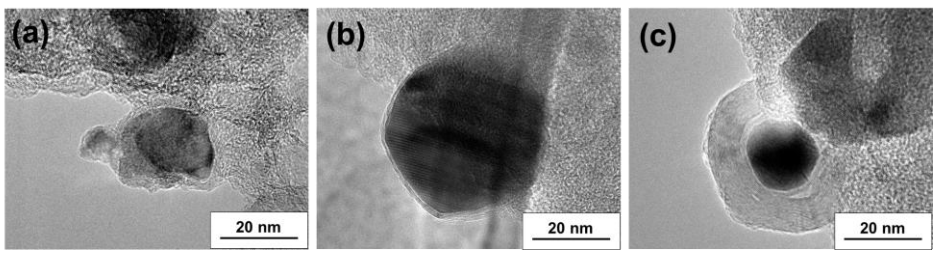

Figure 15. TEM images for (a) Co-N/PDC-1, (b) Co-N/PDC-3, and (c) Co-N/PDC-6.

The chemical structures of the Co-N/PDC catalysts were analyzed in more detail with XPS. Even though the PDCs were subjected to an identical modification procedure (with Co and N) the catalysts exhibited slightly different nitrogen contents of 1.5, 2.1, and 2.4 at% for Co-N/PDC-1, Co-N/PDC-6, and Co-N/PDC-3, respectively [II]. Certain differences were also observed in the deconvoluted N1s spectra of the catalysts as Co-N/PDC-3 exhibits a distinct second peak at higher binding energy values, which is not as developed for Co-N/PDC-1 and Co-N/PDC-6 (**Figure 16a, b, c**). Furthermore, a survey of the C1s region revealed that the PDCs also contain different amounts of carbon-oxygen functionalities which can be considered as defects (**Figure 16d**). Serov et al. [145] proposed that in acidic conditions these parameters, i.e., nitrogen and defect concentrations, correlate with ORR activity. Among the studied Co-N/PDCs, the material synthesized with $ZnCl_2$ as an activating agent, Co-N/PDC-3, comprised the highest amount of nitrogen and defects in the carbon matrix. Analyzing the speciation of cobalt failed most likely due to the en-capsulation of the metallic particles as demonstrated above by TEM.

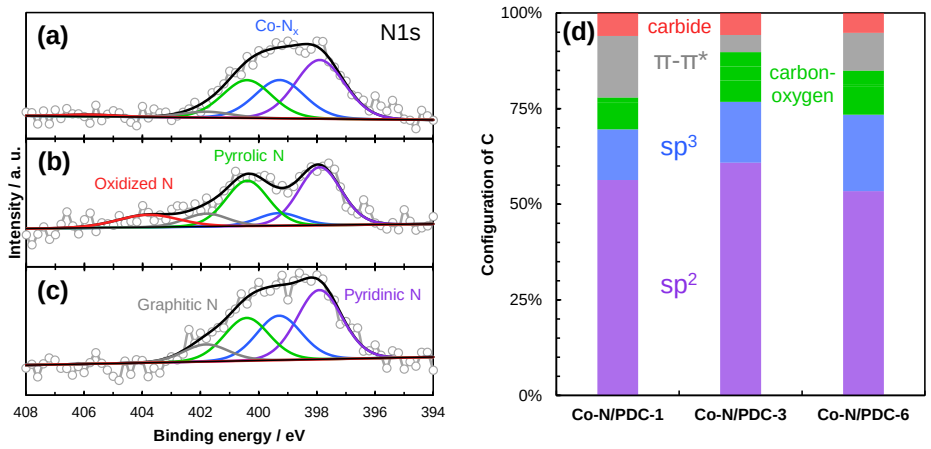

Figure 16. Deconvoluted N1s spectra for (a) Co-N/PDC-1, (b) Co-N/PDC-3, and (c) Co-N/PDC-6, and (d) the relative content of carbon species in the Co-N/PDCs measured with XPS.

7.2.2. Electrochemical performance in acidic and alkaline solutions

The Co-N/PDCs were then studied as ORR catalysts in acidic [II] and alkaline conditions [I, III]. As discussed in the literature overview, reaching the activity of a conventional platinum-based catalyst in acidic media is an extremely difficult task which even state-of-the-art NPGM catalysts struggle with. Despite identical modification procedures, the synthesized Co-N/PDC catalysts exhibit widely different ORR performances in 0.1 M $HClO_4$ with E_{onset} values ranging from 0.72 V vs RHE for Co-N/PDC-5 to 0.80 V vs RHE for Co-N/PDC-3, the catalyst synthesized with $ZnCl_2$ as an activating agent (**Figure 17a**, **Table 4**). Generally, using a more active PDC support provided a more active Co-N/PDC catalyst. These results support the notion that in the case of NPGM catalysts the local environment, i.e., the structure of the carbon matrix, around an active moiety influences the performance of that moiety. Therefore, attention must also be given to engineering suitable carbon networks in addition to pursuing moieties with the highest activity.

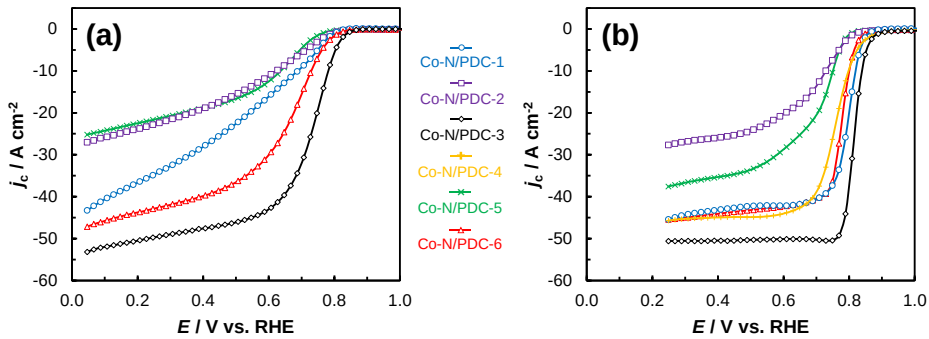

Figure 17. ORR polarization curves measured for the Co-N/PDCs at a catalyst loading of 0.8 mg cm^{-2} in (a) 0.1 M $HClO_4$ at 2000 rpm and (b) 0.1 M KOH at 1500 rpm using a potential scan rate of 10 mV s^{-1}.

As expected, switching to a 0.1 M KOH solution provided significantly improved results (**Figure 17b**, **Table 4**). The E_{onset} value of every Co-N/PDC catalyst was boosted by almost 100 mV with respect to the results obtained in acidic conditions. As a result, the highest E_{onset} value of 0.89 V RHE was measured for the $ZnCl_2$-based catalyst, Co-N/PDC-3. Due to their enhanced performance and well-established current plateaus in the diffusion-limited region, Koutecký-Levich analysis was used to calculate the number of electrons ($n_{K\text{-}L}$) transferred during the ORR (**Table 4**). According to the analysis, the materials catalyze the ORR through a partial 2+2-electron pathway as indicated by average $n_{K\text{-}L}$ values between 3.1 and 3.6. This can partly be attributed to the abundant metallic particles present in the Co-N/PDC catalysts as demonstrated by TEM and XRD methods [II]. Therefore, the synthesis strategy must be improved to incorporate more active sites into the catalysts which promote the direct 4-electron pathway. Furthermore, the catalyst layers on the electrodes are not ideal thin-films as required by the RDE analysis method resulting in very rough estimations for the $n_{K\text{-}L}$ values.

Table 4. E_{onset} values measured in 0.1 M $HClO_4$ and 0.1 M KOH for the Co-N/PDCs and their $n_{K\text{-}L}$ values calculated from the RDE data measured in 0.1 M KOH.

	0.1 M $HClO_4$	0.1 M KOH	
Catalyst	E_{onset} (V vs. RHE)	E_{onset} (V vs. RHE)	$n_{K\text{-}L}$
Co-N/PDC-1	0.76	0.86	3.2
Co-N/PDC-2	0.75	0.82	-
Co-N/PDC-3	0.80	0.89	3.6
Co-N/PDC-4	-	0.89	3.4
Co-N/PDC-5	0.72	0.81	-
Co-N/PDC-6	0.77	0.85	3.1

The array of activities and the data obtained from physical characterization supports the idea proposed by Serov et al. [145] that a higher content of nitrogen and defects in the carbon matrix results in enhanced performance. An exception must be made for Co-N/PDC-1, which exhibited abnormally high ORR activity in alkaline media. However, the catalyst synthesized with $ZnCl_2$ as an activating agent exhibits clearly superior intrinsic activity compared to the other materials which cannot be explained only by the differences observed in XPS. The beneficial effect of $ZnCl_2$ on the ORR activity of NPGM catalysts has been previously observed as well. For example, Ratso et al. [85] demonstrated how enhanced performance in a PEMFC can be obtained by increasing the amount of $ZnCl_2$ used in the synthesis procedure. The impact of $ZnCl_2$ on the results of both PEMFC and AEMFC experiments is discussed in the following sections.

7.3. Pathway #1 catalysts as fuel cell cathodes

As mentioned in the literature overview in section 4.2.4., RDE is an excellent screening tool to rapidly benchmark the intrinsic activity of NPGM catalysts. In contrast, studying the importance of morphology, such as porosity, is a much more difficult task, although not entirely impossible [146]. Hence, fabricating the catalysts into fuel cell cathodes and studying them in a single cell setup is critically important. While fuel cell tests are in general more important than RDE experiments, they are also substantially more difficult as both fabricating the electrodes and measuring the single cells are complex procedures with many parameters to consider.

7.3.1. PEMFC performance

Two best-performing Co-N/PDC catalysts were studied as PEMFC cathodes [II]. Acidic media was chosen for the first test because the ability to construct and measure PEMFC single cells, including those based on NPGM catalysts, has been previously demonstrated by our workgroup [147,148] and is thus a more reliable starting point. Additionally, PEMFC technology is more mature than AEMFC technology due to the existence of a well-developed commercial membrane in Nafion™.

Similarly to the RDE measurements, the Co-N/PDCs exhibit widely different performances reaching almost a two-fold difference in peak power density (*PPD*) values (**Figure 18**). The catalyst based on $ZnCl_2$, Co-N/PDC-3, consistently outperformed the catalyst based on multi-step pyrolysis, Co-N/PDC-6, throughout the entire measured current density range. This can be attributed to several factors. Firstly, Co-N/PDC-3 contains a larger amount of nitrogen and defects in the carbon matrix, both of which have been proposed as sources of activity [145]. Secondly, an *SSA* value roughly twice as large was observed for the $ZnCl_2$-based catalyst. The *PPD* value of 210 mW cm^{-2} obtained for the best Co-N/PDC catalyst also marked a significant improvement

over our workgroups previous attempts at utilizing NPGM catalysts as PEMFC cathodes [148]. Despite these advances, an identical PEMFC test with a state-of-the-art NPGM catalyst as the cathode provided superior performance with a *PPD* value of roughly 400 mW cm^{-2} (data not shown).

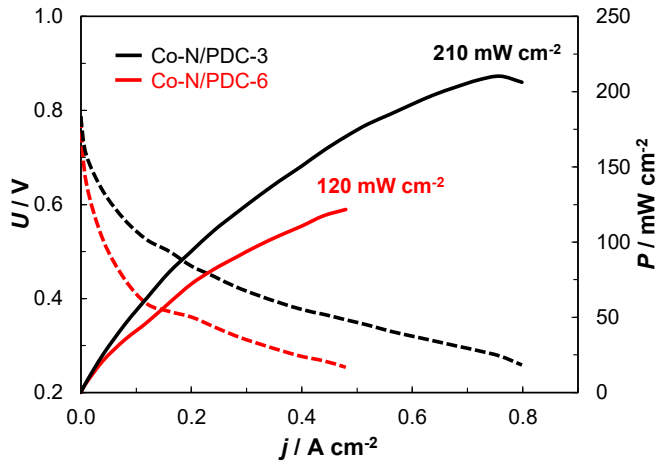

Figure 18. Polarization (dashed lines) and power density (solid lines) curves and the *PPD* values measured for the Co-N/PDCs in a PEMFC experiment. Measurement conditions: cathode catalyst: Co-N/PDC, 4.0 mg cm^{-2}; anode catalyst: 60 wt% Pt/Vulcan, 1.0 mg cm^{-2}; membrane: Nafion™ HP; cell temperature: 80 °C; oxygen/ hydrogen dew points, flow rates, and backpressures: 80/80 °C, 200/200 ml min^{-1}, 100/100 kPa.

7.3.2. AEMFC performance

While not as technologically mature as PEMFCs, AEMFCs present a unique opportunity to utilize NPGM catalysts in milder conditions and thus should be rigorously studied. The need for alkaline conditions is clearly illustrated by the RDE experiments discussed above in section 7.2.2. where a positive shift in E_{onset} values of ~100 mV was observed for every Co-N/PDC catalyst when switching from acidic to alkaline media. Fortunately, at the time there were a couple of AEM and ionomer products available despite their limited performance in fuel cells [139,149]. Our workgroup decided on using a FuMA-Tech membrane and ionomer as well as an increased sample size of four Co-N/PDC catalysts [III].

The performance of the Co-N/PDCs in AEMFC tests could be clearly categorized (**Figure 19a**). Three of the less-active catalysts, Co-N/PDC-1, Co-N/PDC-4, and Co-N/PDC-6, performed almost identically at low current densities. One by one, the performances of the catalysts fell off as severe mass-transport limitations emerged once larger current densities were reached. We concluded that the intrinsic activities of these catalysts must be similar and the

differences in *PPD* values can be attributed to catalyst morphology as discussed below.

In contrast, the performance of the $ZnCl_2$-based catalyst, Co-N/PDC-3, was clearly higher owing to its superior intrinsic activity evident from the RDE measurements. Both these results and the data obtained in PEMFC tests strongly suggest that $ZnCl_2$ helps form pores which are suitable for the active sites of an NPGM catalyst. The performance of Co-N/PDC-3 was also comparable to other NPGM catalysts presented in the literature when FuMA-Tech membranes were used to fabricate the MEAs [150–152].

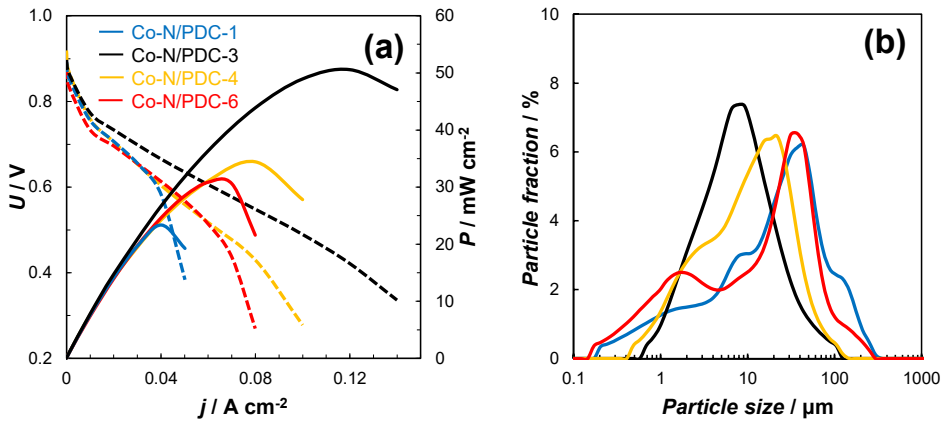

Figure 19. (a) Polarization (dashed lines) and power density (solid lines) curves measured for the Co-N/PDCs in an AEMFC experiment. Measurement conditions: cathode catalyst: Co-N/PDC, 4.0 mg cm^{-2}; anode catalyst: 60 wt% PtRu/Ketjen-black, 0.67 mg cm^{-2}; membrane: FAA-3-50; cell temperature: 60 °C; oxygen/hydrogen dew points, flow rates, and backpressures: 58/58 °C, 50/50 ml min^{-1}, 0/0 kPa. (b) Volumetric particle size distributions measured for the Co-N/PDCs using laser diffraction.

Another important aspect of catalyst morphology next to porosity is the size of the particles. Analyzing the catalysts with laser diffraction demonstrated that the powders are quite inhomogeneous and consist of medium- and large-sized particles (**Figure 19b**). Interestingly, we observed a direct inverse correlation between the median volumetric particle sizes (*Dv50*) of the catalyst powders and their *PPD* values in the AEMFC test (**Figure 20**). Additionally, higher *PPD* values were provided by catalysts with more uniform particle size distribution. An explanation for this phenomenon requires examining the structure of the catalyst layer (**Figure 2**). The ORR can only proceed at the TPB where oxygen, an active site, and the ionomer converge. Therefore, an extensive interconnected ionomer network is required for high performance. A catalyst powder with large and unevenly sized particles can more easily assemble into a dense packed layer where a suitable ionomer network cannot form. In such an agglomerated

catalyst layer many of the active sites are not connected to the ionomer rendering them useless. This logic is supported by the morphology of conventional platinum-based catalysts which consist of significantly smaller and much more homogeneous carbon support particles (data not shown). Besides median particle sizes, the *PPD* values obtained for the catalysts also correlated with their S_{BET} values and nitrogen content measured with XPS (**Figure 20**).

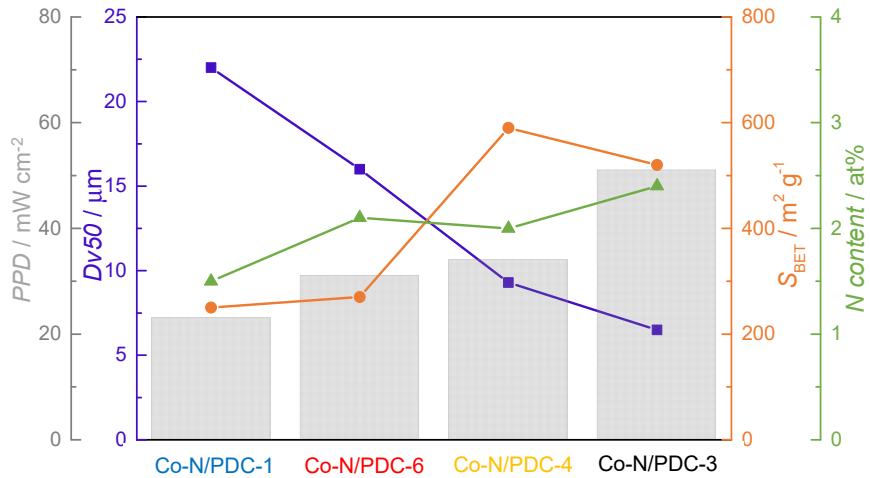

Figure 20. Correlations between peak power density (*PPD*) and median particle size by volume (*Dv50*), specific surface area (S_{BET}), and nitrogen content measured with XPS for the Co-N/PDCs.

Despite a more suitable environment, the *PPD* achieved with the $ZnCl_2$-based catalyst, Co-N/PDC-3, was roughly four times lower than the *PPD* reached in a PEMFC test. Much of this can be attributed to the technological maturity of the two membranes used to fabricate the MEAs. For instance, the specific conductivity of the proton-conducting Nafion™ is roughly two times higher than the conductivity of the hydroxide-conducting FAA-3-50 membrane [153]. Additionally, the two membranes have significantly different thicknesses of 20 µm and 50 µm for Nafion™ HP and FAA-3-50, respectively, leading to further ohmic losses. Therefore, improvements in single cell performance can certainly be expected by using a more advanced AEM, which we demonstrate in the final section.

7.4. Improving performance via synthesis pathway #2

Overall, the performance of the PDC catalysts synthesized so far is encouraging but improvements are still needed regarding both intrinsic activity and porosity to reach the performance of the commercial state-of-the-art NPGM catalyst. As a result, the synthesis strategy was redesigned from an approach based on pathway #1 to an approach based on pathway #2 [IV]. More specifically, the peat was carbonized together with the metal salt and nitrogen source instead of first synthesizing a carbon support material which was then modified with active sites. Through this change the active sites should be more effectively distributed in the carbon matrix (see section 4.2.1.). The metal was switched from cobalt to iron since the following sections focus exclusively on alkaline conditions where iron tends to provide superior results according to the literature [50]. Additionally, guanidine carbonate, a small and inexpensive nitrogen-rich compound, was used as a new nitrogen source. $ZnCl_2$ was also included as a chemical activator and template because using it provided the best results in the previous sections. A commercial state-of-the-art NPGM catalyst denoted as Fe-N-C-comm in both the text and in publication [IV] is used as a reference material where relevant in the analysis.

7.4.1. Enhancing intrinsic activity through synthesis optimization

The following section focuses on varying the parameters of the redesigned synthesis strategy to enhance both the intrinsic activity and porosity of the PDC catalysts [IV]. The variations can be divided into two series with the first varying the amount of either Fe or $ZnCl_2$ and the second varying the pyrolysis temperature. The baseline catalyst, Fe-N-PDC-1, consisted of fairly large and unevenly sized carbon particles similarly to the previous PDC catalysts. However, the Fe-N-PDC-1 exhibited a significantly higher SSA value of 950 $m^2\ g^{-1}$ (**Figure 21**) owing to abundant microporosity generated by $ZnCl_2$. Unfortunately, the mesoporosity present in the pristine $ZnCl_2$-based PDC-3 was not obtained for the new catalyst due to suboptimal synthesis conditions. The elemental composition of the new catalyst Fe-N-PDC-1 as determined by SEM-EDS comprised of a substantial amount of nitrogen (8.7 wt%), and smaller amounts of iron (1.0 wt%) and residual zinc (0.5 wt%) in addition to carbon and oxygen [IV].

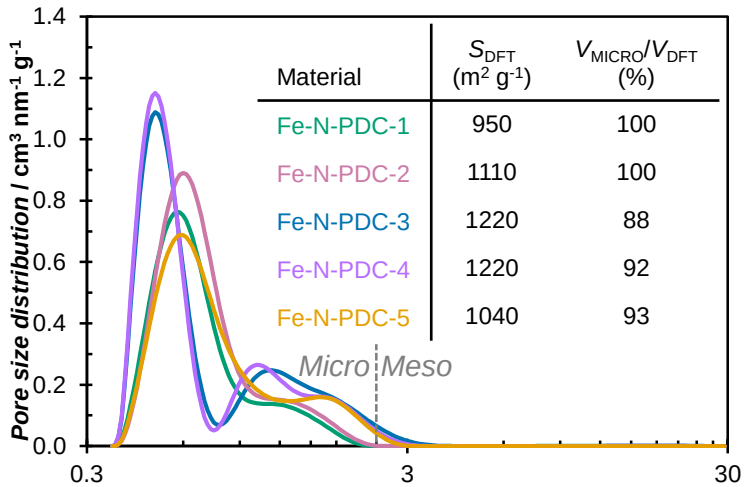

Figure 21. Pore size distributions, (inset) S_{DFT} values, and V_{MICRO}/V_{DFT} values for the Fe-N-PDCs.

In the RRDE experiments conducted in alkaline media, the baseline PDC catalyst, Fe-N-PDC-1, already exhibited enhanced intrinsic activity indicated by its slightly higher E_{onset} value (0.90 vs. 0.89 V vs. RHE) at a significantly lower catalyst loading (0.3 vs. 0.8 mg cm^{-2}) compared to the previous best result obtained with Co-N-PDC-3 (**Figure 22a**). However, a fairly high peroxide yield of 53% was calculated using Formula 2 corresponding to a low electron transfer number of 3.1 compared to the 3.6 achieved with Co-N-PDC-3. Some part of the disparity can be assigned to the different methodologies used to calculate these values with direct measurement via RRDE and estimation via Koutecký-Levich analysis for the former and latter results, respectively. In a brief analysis of similar peat-based Fe-N-C catalysts, we demonstrated that the Koutecký-Levich analysis tends to overestimate the electron transfer number [154]. A more significant portion of the difference can be attributed to the catalyst loadings as peroxide has a larger probability to be reduced further before escaping into the bulk electrolyte in a thicker catalyst layer compared to a thinner one [155].

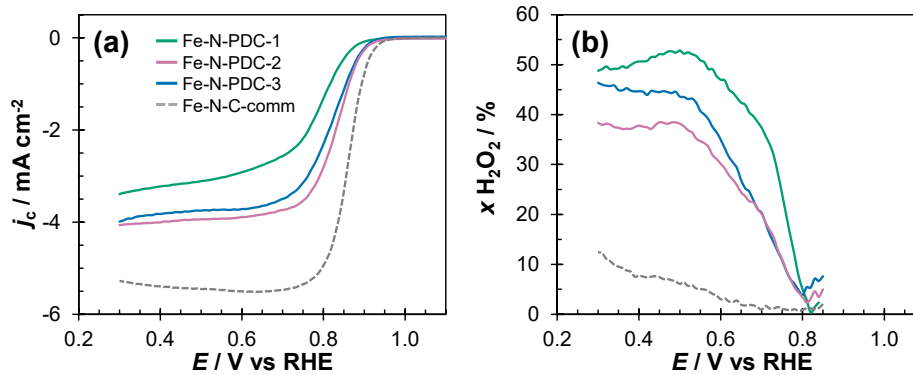

Figure 22. (a) ORR polarization curves and (b) peroxide yield measured for Fe-N-PDC-1...3 and Fe-N-C-comm at a catalyst loading of 0.3 mg cm^{-2} in 0.1 M KOH at 1600 rpm using a potential scan rate of 10 mV s^{-1}.

In the first series, increasing the amount of Fe for Fe-N-PDC-2 did not produce any noticeable changes in the physical properties. Doubling the amount of $ZnCl_2$, however, yielded a material, Fe-N-PDC-3, with a certain degree of mesoporosity (**Figure 21**). Despite only small changes in the physical properties, increasing the amount of either precursor enhanced the ORR activity by 20 mV in the RRDE tests (**Figure 22a** and **Table 5**). Considerably lower peroxide yields compared to the baseline catalyst (**Figure 22b**) were observed for both Fe-N-PDC-2 and Fe-N-PDC-3 as well. For the catalyst Fe-N-PDC-3 with a doubled amount of $ZnCl_2$, these improvements were attributed to the enhanced porosity created by the template. A larger amount of highly active moieties can form in the micropores and more of the active sites are available on the enlarged surface. Similar tendencies have been demonstrated by other authors [77,80].

Table 5. Electrochemical activity and selectivity descriptors for Fe-N-PDC-1…5, Fe-N-PDC-HA, and Fe-N-C-comm measured with the RRDE method in 0.1 M KOH.

Catalyst	E_{onset} (V vs. RHE)	x H_2O_2 at 0.5 V (%)	MA at 0.9 V (A g^{-1})
Fe-N-PDC-1	0.90	53	0.2
Fe-N-PDC-2	0.92	38	0.9
Fe-N-PDC-3	0.92	44	0.7
Fe-N-PDC-4	0.94	33	1.9
Fe-N-PDC-5	0.94	45	2.6
Fe-N-PDC-HA	0.96	14	4.1
Fe-N-C-comm	0.94	6	2.9

In the second series (Fe-N-PDC-3…5), raising the pyrolysis temperature in 100 °C intervals up to 1000 °C provided only minimal changes in the structural characteristics. Conversely, a higher pyrolysis temperature led to a decreased retention of nitrogen and zinc due to their higher volatility at higher temperatures [IV]. Similar behavior has been commonly observed for NPGM catalysts utilizing zinc in the synthesis procedure [70,72]. Importantly, while a higher amount of nitrogen might be desired for better activity, as discussed in our previous analysis, it is not always the case. Zhang et al. [72] demonstrated that the form of the nitrogen is more important than the overall amount. In their analysis, raising the pyrolysis temperature from 800 °C to 1100 °C shifted the nitrogen from mainly a pyridinic form towards a more graphitic form according to detailed N1s region XPS spectra. The shift in nitrogen form was proposed as one explanation for enhanced ORR activity when the pyrolysis steps were conducted at higher temperatures. The same principles are valid for the second series of PDC catalysts (**Figure 23a, b, c**).

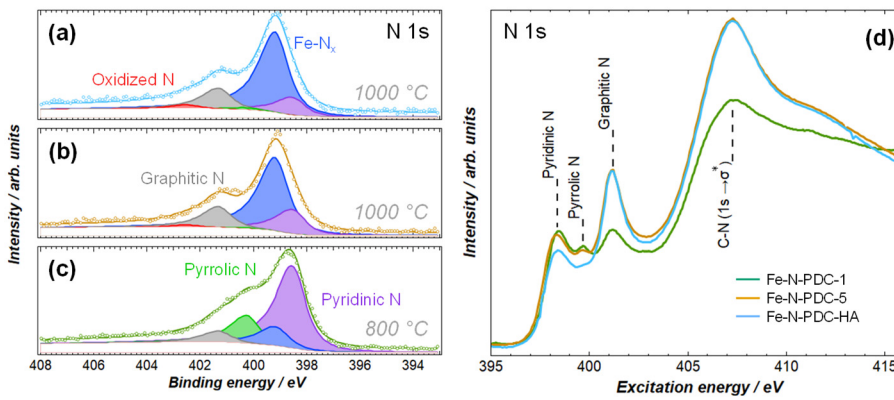

Figure 23. Deconvoluted N 1s XPS spectra for (a) Fe-N-PDC-HA, (b) Fe-N-PDC-5, and (c) Fe-N-PDC-1 along with the respective pyrolysis temperatures used in their synthesis. (d) N 1s XAS spectra for Fe-N-PDC-1, Fe-N-PDC-5, and Fe-N-PDC-HA.

More specifically, increasing the pyrolysis temperature up to 1000 °C provided a catalyst, Fe-N-PDC-5, with a larger amount of graphitic nitrogen, Fe-N_x moieties, and a 20 mV more positive E_{onset} value (**Figure 24** and **Table 5**). The N 1s data measured with XAS also demonstrate that the catalysts synthesized at a higher temperature contain a larger amount of graphitic nitrogen (**Figure 23d**). For highly active NPGM catalysts, an additional activity descriptor known as mass activity (*MA*), which is defined as the current produced per gram of catalyst at 0.9 V vs. RHE, is used to scrutinize the intrinsic activity of catalysts in more detail. Calculating this parameter (**Table 5**) indicated that the ORR activity of Fe-N-PDC-5, which was pyrolyzed at 1000 °C, exhibits *MA* (2.6 A g^{-1}) approaching that of Fe-N-C-comm (2.9 A g^{-1}), a reference state-of-the-art NPGM catalyst. Overall, optimizing the synthesis conditions was

successful in enhancing intrinsic activity by generating better active sites but fell short in enhancing porosity.

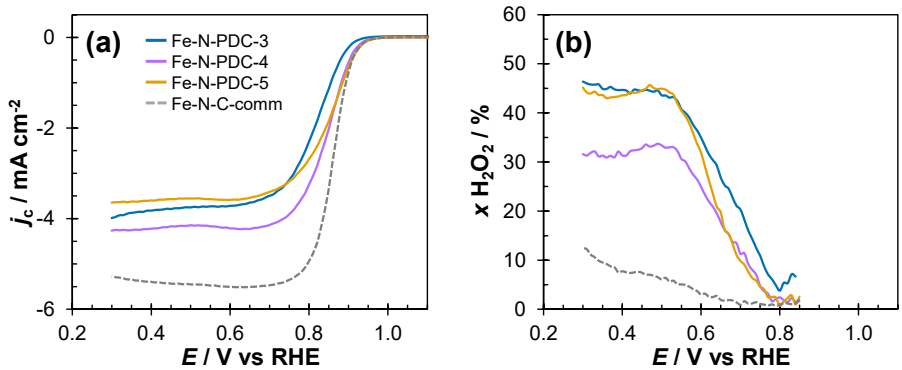

Figure 24. (a) ORR polarization curves and (b) peroxide yield measured for Fe-N-PDC-3...5 and Fe-N-C-comm at a catalyst loading of 0.3 mg cm^{-2} in 0.1 M KOH at 1600 rpm using a potential scan rate of 10 mV s^{-1}.

7.4.2. Superior porosity with hydroxyapatite

As the next step, a novel PDC catalyst was synthesized by employing the knowledge gained in the previous section. As a result, the amounts of both iron and $ZnCl_2$ were doubled and the pyrolysis steps were conducted at 1000 °C. Additionally, we utilized hydroxyapatite (HA) as a hard template to enhance the porosity of the PDC catalysts. The used HA is an acicular nanopowder mainly composed of calcium and phosphorous with particles sized roughly 80 nm and 20 nm in length and width, respectively (**Figure 25a**). These particles were easily leached out with less toxic 1 M HNO_3 compared to the HF needed for leaching silicon-based hard templates. The result was Fe-N-PDC-HA, a PDC catalyst with significantly smaller and more evenly sized particles as HA inhibited the carbon grains from fusing together and forming larger grains at the elevated pyrolysis temperature. The major differences in particle size distributions are evident qualitatively from the HR-SEM images (**Figure 25b, c**), and quantitatively from the results obtained with laser diffraction measurements (**Figure 25b, c** insets).

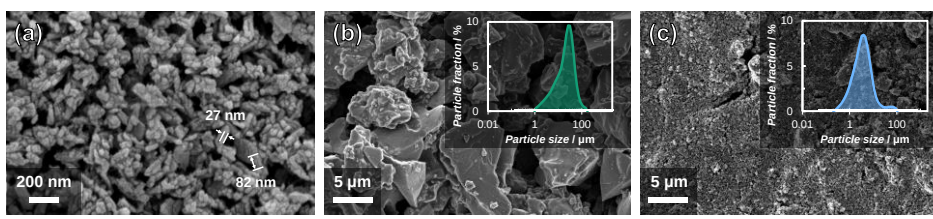

Figure 25. HR-SEM images for (a) HA, (b) Fe-N-PDC-1, and (c) Fe-N-PDC-HA. Insets demonstrate particle size distributions measured using laser diffraction.

Importantly, leaching the HA hard template produced a unique network of pores and interparticle cavities which were studied in more detail with low-temperature N_2-sorption and mercury intrusion porosimetry methods. The N_2-sorption analysis (**Figure 26a**) indicated that Fe-N-PDC-HA contains only a modest amount of mesopores ranging from 3 to 20 nm. However, pores larger than 30 nm, which is where the main templating effect of the HA particles should be expected, are outside the range of the used pore size distribution modeling method. A more suitable method for analyzing larger pores, mercury intrusion porosimetry, confirmed the templating effect of HA as the catalyst contains abundant pores ranging from 10 to 80 nm as well as from 80 to 3000 nm (**Figure 26b**). These pores can be attributed to individual HA nanoparticles and HA agglomerates added into the synthesis mixture, respectively. The results clearly demonstrate how superior meso- and macroporosity can be obtained in Fe-N-PDC-HA by using HA as a hard template since such meso- and macroporosity is extremely limited for the catalyst synthesized without HA, Fe-N-PDC-1.

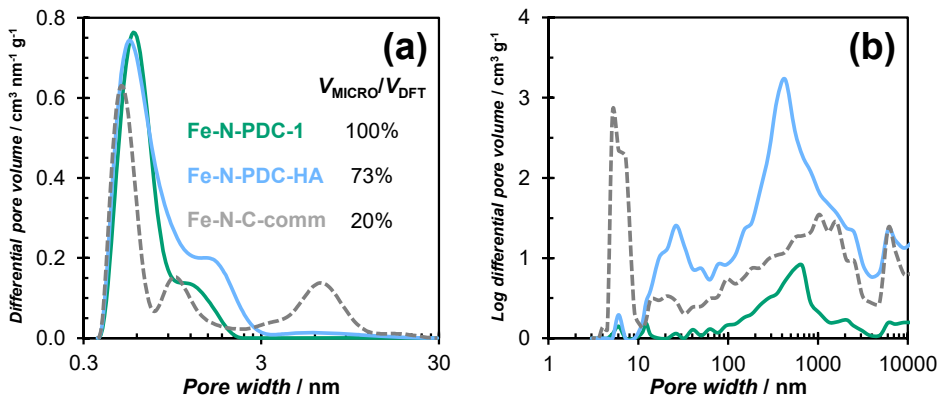

Figure 26. Pore size distributions and (a inset) V_{MICRO}/V_{DFT} values obtained for Fe-N-PDC-1, Fe-N-PDC-HA, and Fe-N-C-comm using (a) low-temperature N_2 sorption and (b) mercury intrusion porosimetry.

Besides changes in morphology, using HA as a hard template also provided certain modifications in the chemical composition of the catalyst compared to the materials synthesized in the previous section. For instance, phosphorous was incorporated into the structure of Fe-N-PDC-HA as evidenced by SEM-EDS data [IV]. Analyzing the catalyst with TEM and XRD methods (**Figure 27**) reveal that the phosphorous is present in the form of Fe_2P particles. Data about whether Fe_2P particles provide adequate ORR activity is a subject only recently raised [156–158]. However, XPS and XAS measurements indicate that the form of nitrogen in Fe-N-PDC-HA is similar to the previous catalyst pyrolyzed at 1000 °C, Fe-N-PDC-5, due to their identical pyrolysis conditions (**Figure 23**).

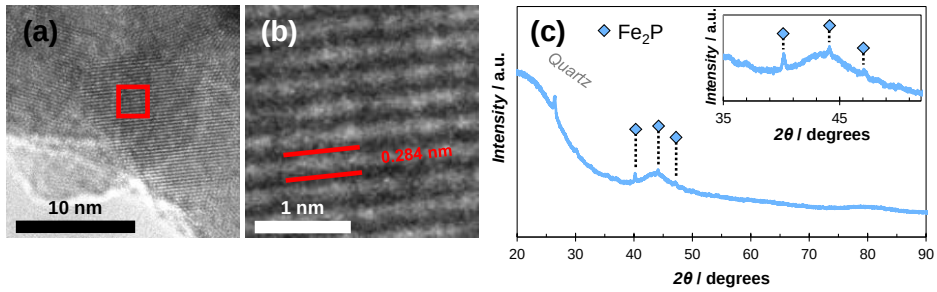

Figure 27. (a) TEM image for Fe-N-PDC-HA, (b) magnified TEM image of the highlighted area, and (c) XRD pattern for Fe-N-PDC-HA with (c inset) a magnified pattern demonstrating the peaks corresponding to Fe_2P.

According to the RRDE experiments, utilizing improved synthesis conditions and including HA as a hard template produced a catalyst with exceptional ORR activity (**Figure 28a**). An E_{onset} value of 0.96 V vs. RHE and an *MA* value of 4.1 A g^{-1} was achieved for Fe-N-PDC-HA (**Table 5**). The result represents an improvement over the reference NPGM catalyst (Fe-N-C-comm) which exhibited respective values of 0.94 V vs. RHE and 2.9 A g^{-1}. A stark improvement in the peroxide yield (**Figure 28b**, **Table 5**) was observed as well for the HA-based catalyst compared to the previously synthesized PDC catalysts. The next step was validating the excellent activity achieved in the RRDE screening tests in a more relevant AEMFC experiment.

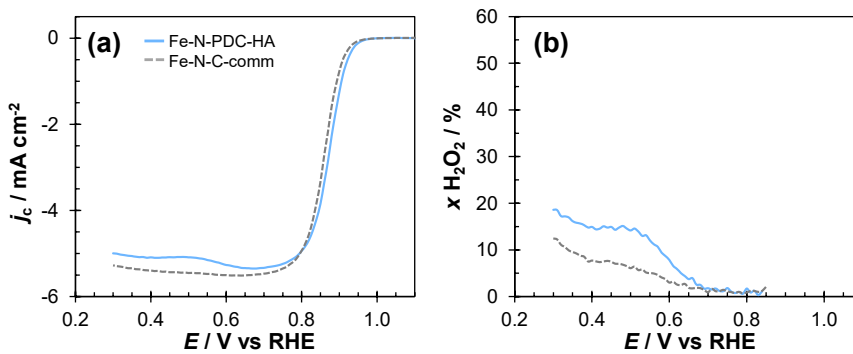

Figure 28. (a) ORR polarization curves and (b) peroxide yield measured for Fe-N-PDC-HA and Fe-N-C-comm at a catalyst loading of 0.3 mg cm^{-2} in 0.1 M KOH at 1600 rpm using a potential scan rate of 10 mV s^{-1}.

7.3.3. High-performance AEMFC

In recent years, constructing AEMFC single cells has become more manageable due to the emergence of several promising commercial hydroxide exchange membranes and ionomers offered by start-ups branching out from university

research groups. We opted to use a 20 µm thin membrane and two ionomers produced by Xergy Inc. as these components have provided record-breaking AEMFC performance with conventional platinum-based catalysts [159]. Additionally, a redesigned electrode formation method developed by Mustain et al. [108,140] was used to accommodate the new membrane and ionomer technology.

AEMFC measurements were conducted with three of the PDC catalysts synthesized using the improved strategy involving pathway #2 and the reference NPGM catalyst. The selection included the baseline PDC catalyst (Fe-N-PDC-1), the catalyst synthesized using an elevated pyrolysis temperature of 1000 °C (Fe-N-PDC-5), and the catalyst synthesized with the improved conditions and HA as a hard template (Fe-N-PDC-HA).

The results clearly demonstrate recent breakthroughs in the field of AEMFCs as performances an order of magnitude higher were obtained with the new electrode fabrication technique (**Figure 29**) over the one utilized previously for the pathway #1 catalysts (**Figure 19a**). While the two catalysts synthesized without HA, Fe-N-PDC-1 and Fe-N-PDC-5, exhibited considerably different activities in RRDE tests, differences in AEMFC performance are not as evident. More specifically, the catalyst pyrolyzed at a higher temperature generates higher current densities at high cell voltages (over 0.8 V) due to its higher intrinsic activity. At lower cell voltages, however, the higher intrinsic activity of this catalyst cannot be fully utilized due to mass-transport limitations arising from extremely limited meso- and macroporosity. As a result, only marginally different *PPD* values of 520 and 480 mW cm^{-2} were achieved for Fe-N-PDC-5 and Fe-N-PDC-1, respectively.

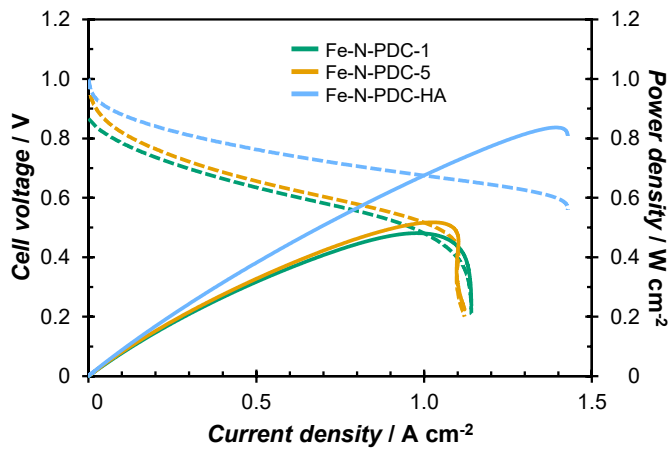

Figure 29. Polarization (dashed lines) and power density (solid lines) curves measured for the Fe-N-PDCs in an AEMFC experiment. Measurement conditions: cathode catalyst: Fe-N-PDC, 1.0 mg cm^{-2}; anode catalyst: 60 wt% PtRu/Ketjen-black, 1.0 mg cm^{-2}; membrane: Xion AEM-Pention-72-15CL-20um; cell temperature: 65 °C; oxygen/hydrogen dew points, flow rates, and backpressures: 63/58 °C, 1000/500 ml min^{-1}, 100/100 kPa.

In contrast, the PDC catalyst synthesized with HA as a hard template, Fe-N-PDC-HA, demonstrated an almost two-fold increase in performance over the previous two catalysts reaching a *PPD* value of 840 mW cm^{-2} (**Figure 29**). Both intrinsic activity and porosity contribute to such a significant improvement. Firstly, the used synthesis conditions lead to the formation of moieties with higher activities according to XPS and XAS measurements (**Figure 23**). Secondly, the unique network of pores and cavities (**Figure 26**) improves the availability of the active sites and severely improves the mass-transport properties of the catalyst.

Finally, additional measurements were made at an elevated cell temperature of 80 °C to compare the best-performing catalyst, Fe-N-PDC-HA, to the reference state-of-the-art NPGM catalyst, Fe-N-C-comm (**Figure 30**). The two catalysts exhibit identical performance at cell voltages above 0.6 V confirming the excellent activity of Fe-N-PDC-HA. Below 0.6 V the polarization curves diverge as mass-transport limitations emerge later for the reference catalyst. This was attributed to the differences in porosity as Fe-N-PDC-HA contains only a limited number of pores between 3 and 10 nm (**Figure 26**). In contrast, the reference catalyst has a continuous pore size distribution ranging from micropores to macropores. A hierarchical pore network such as this has been proposed as a critical factor in fully utilizing NPGM catalysts in fuel cells [160–164]. Therefore, another performance boost should be expected if more pores between 3 and 10 nm could be generated in the catalyst by optimizing the amounts of the used templates, $ZnCl_2$ and HA.

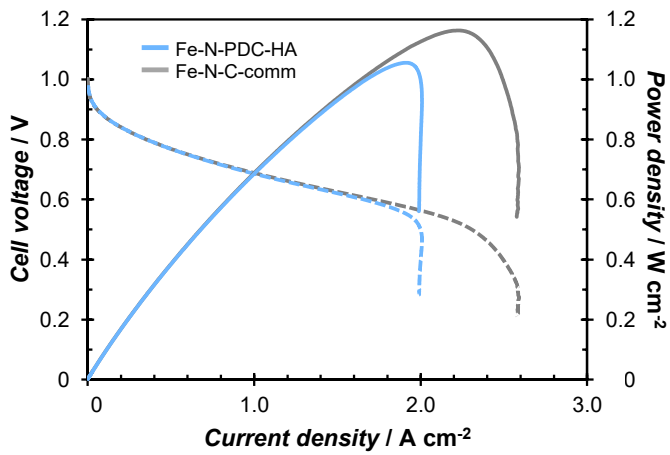

Figure 30. Polarization (dashed lines) and power density (solid lines) curves measured for Fe-N-PDC-HA and Fe-N-C-comm in an AEMFC experiment. Measurement conditions: cathode catalyst: Fe-N-PDC-HA or Fe-N-C-comm, 1.0 mg cm^{-2}; anode catalyst: 60 wt% PtRu/Ketjenblack, 1.0 mg cm^{-2}; membrane: Xion AEM-Pention-72-15CL-20um; cell temperature: 80 °C; oxygen/hydrogen dew points, flow rates, and backpressures: 77/71 °C, 1000/500 ml min^{-1}, 100/100 kPa.

Overall, Fe-N-PDC-HA can be categorized as a high-performing AEMFC catalyst. In a recent review, Hossen et al. [56] provided a thorough overview of NPGM catalysts in alkaline media and noted that only 13 catalysts have exceeded the 1000 mW cm^{-2} *PPD* threshold in an AEMFC experiment. The *PPD* of 1060 mW cm^{-2} obtained here places the synthesized Fe-N-PDC-HA catalyst among those highly active catalysts validating the synthesis approach we presented in this work.

7.5. Conclusions

A summary of the progress in developing NPGM ORR catalysts from peat throughout this study is presented in **Figure 31**. The performance of the PDC catalysts in the three-electrode setup as demonstrated by the E_{onset} value was improved by systematically improving the synthesis strategy. Namely, a noticeable increase in activity was observed when switching from synthesis pathway #1 to pathway #2 and optimizing the synthesis conditions. Additionally, including $ZnCl_2$ in the synthesis mixture as an activating agent and pore former had a clear beneficial effect on the ORR activity. Progress in the *PPD* values obtained in AEMFC experiments were achieved by utilizing improved AEM technology and, importantly, enhancing the meso- and macroporosity of the catalysts via hard templating with HA. It can be concluded that the **hypothesis** established at the beginning of the study was proven as naturally abundant peat was converted into a highly active and porous NPGM ORR catalyst with excellent AEMFC performance. This was accomplished with well-decomposed peat, which is currently only used in low-value applications and is a net emitter of carbon. The results of this thesis provide valuable information towards achieving the **research aim** of developing novel NPGM ORR catalysts by valorizing naturally abundant local resources with the end goal of replacing conventional platinum-based catalysts.

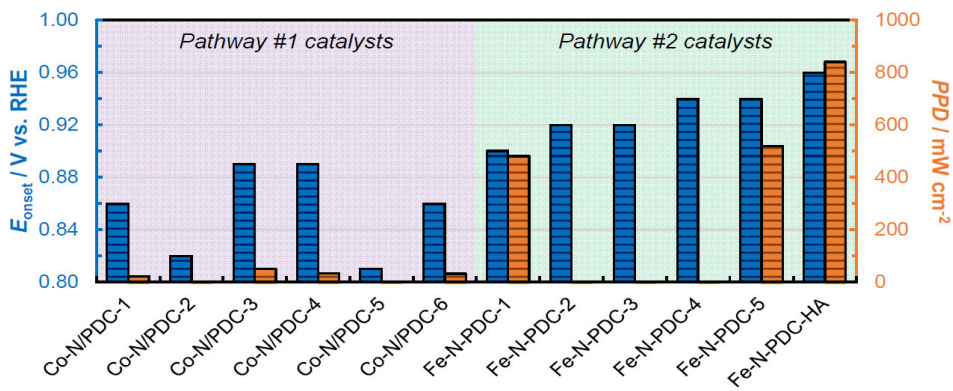

Figure 31. A summary of the E_{onset} values measured with R(R)DE in 0.1 M KOH (left axis) and *PPD* values in AEMFC experiments (right axis) for the PDC catalysts synthesized via pathway #1 [I,III] (left) and pathway #2 [IV] (right).

8. SUMMARY

In this study, naturally abundant Estonian well-decomposed peat was modified into non-platinum group metal (NPGM) oxygen reduction reaction (ORR) catalysts via two principal synthesis pathways. The obtained materials were rigorously analyzed with a wide selection of physical and electrochemical characterization methods. Scrutinizing the data led to several findings on how the performance of the catalysts depends on their physical properties.

Synthesis pathway #1 consisted of first carbonizing the peat into carbon support materials utilizing various activating agents or multi-step pyrolysis and then modifying the carbon supports with Co and N. The analysis demonstrated that the specifics of the carbonization procedure have a major impact on final properties of the materials, both physical and electrochemical. For example, the inclusion of an activating agent yielded carbon networks with higher porosity. Importantly, $ZnCl_2$ as an activator seemed to generate certain changes in the catalysts nanostructure leading to enhanced ORR performance. The $ZnCl_2$-based NPGM catalyst exhibited the highest ORR activity in both acidic and alkaline media as well as both three-electrode rotating disc electrode and two-electrode fuel cell experiments. Furthermore, higher anion exchange membrane fuel cell (AEMFC) performances were reached with catalyst layers consisting of smaller-sized catalyst particles. Analyzing the results obtained with the pathway #1 catalysts led to the conclusion that using $ZnCl_2$ in the synthesis as an activating agent boosts the ORR performance of a peat-derived carbon catalyst.

Synthesis pathway #2 consisted of carbonizing the peat together with sources of Fe and N in a one-pot method. $ZnCl_2$ was additionally included as an activating agent due to its positive impact noted in the synthesis pathway #1 section. Changing the synthesis strategy yielded an NPGM catalyst with enhanced activity compared to the previous materials. Further improvements were obtained through optimizing the synthesis conditions by increasing the amounts of Fe and $ZnCl_2$, and increasing the pyrolysis temperature from 800 to 1000 °C. The enhanced ORR activity of the improved catalysts was attributed to a larger number of micropores and an increased proportion of Fe-N_x and graphitic nitrogen species. However, the progress in activity was not realized in AEMFC experiments due to the limited meso- and macroporosity of the catalysts.

The limited meso- and macroporosity was solved by including a hydroxyapatite (HA) hard template in the synthesis mixture. Removing the calcium- and phosphorous-based HA nanoparticles sized roughly 20 nm in width and 80 nm in length by acid washing with 1 M HNO_3 resulted in a catalyst material with a unique porous structure consisting of abundant meso- and macropores. Improving the porosity was crucial in increasing the availability of the active sites and facilitating the mass transport of reactants and products in the electrode structure. The result was an excellent peak power density value of

1060 mW cm^{-2} in an AEMFC experiment. Notably, using HA as a hard template allows circumventing the extremely toxic HF needed for leaching silica-based hard templates commonly used for obtaining meso- and macroporosity in state-of-the-art NPGM catalysts.

In conclusion, the results of this thesis demonstrated how to synthesize active and porous NPGM catalysts from abundant well-decomposed peat by tuning their physical and electrochemical properties through improving the synthesis method. As a result, a strategy for valorizing low-value peat into advanced functional materials for fuel cell applications was obtained.

9. REFERENCES

[1] IEA, Global Energy Review 2021, (2021). https://www.iea.org/reports/global-energy-review-2021 (accessed May 27, 2023).

[2] Production and forecast | Elering, (2023). https://elering.ee/en/production-and-forecast (accessed May 22, 2023).

[3] Development projects – Eesti Tuuleenergia Assotsiatsioon, (2023). https://tuuleenergia.ee/development-projects/?lang=en (accessed May 22, 2023).

[4] IRENA, Renewable power generation costs in 2021, (2021).

[5] State aims to expedite development of renewable energy | Eesti Vabariigi Valitsus, (2022). https://valitsus.ee/en/news/state-aims-expedite-development-renewable-energy (accessed May 22, 2023).

[6] Electricity consumption and production | Elering, (2021). https://elering.ee/en/electricity-consumption-and-production (accessed May 28, 2023).

[7] M.Z. Jacobson, M.A. Delucchi, Z.A.F. Bauer, S.C. Goodman, W.E. Chapman, M.A. Cameron, C. Bozonnat, L. Chobadi, H.A. Clonts, P. Enevoldsen, J.R. Erwin, S.N. Fobi, O.K. Goldstrom, E.M. Hennessy, J. Liu, J. Lo, C.B. Meyer, S.B. Morris, K.R. Moy, P.L. O'Neill, I. Petkov, S. Redfern, R. Schucker, M.A. Sontag, J. Wang, E. Weiner, A.S. Yachanin, 100% Clean and Renewable Wind, Water, and Sunlight All-Sector Energy Roadmaps for 139 Countries of the World, Joule. 1 (2017) 108–121. https://doi.org/10.1016/j.joule.2017.07.005.

[8] I. Staffell, D. Scamman, A.V. Abad, P. Balcombe, P. E. Dodds, P. Ekins, N. Shah, K. R. Ward, The role of hydrogen and fuel cells in the global energy system, Energy Environ. Sci. 12 (2019) 463–491. https://doi.org/10.1039/C8EE01157E.

[9] European Commission, A Hydrogen Strategy for a climate neutral Europe, (2020). https://ec.europa.eu/commission/presscorner/api/files/attachment/865942/EU_Hydrogen_Strategy.pdf.pdf (accessed May 27, 2023).

[10] U.S. DOE, DOE National Clean Hydrogen Strategy and Roadmap, (2022). https://www.hydrogen.energy.gov/pdfs/clean-hydrogen-strategy-roadmap.pdf (accessed May 27, 2023).

[11] J. Michalski, M. Poltrum, U. Bünger, The role of renewable fuel supply in the transport sector in a future decarbonized energy system, Int. J. Hydrog. Energy. 44 (2019) 12554–12565. https://doi.org/10.1016/j.ijhydene.2018.10.110.

[12] M.M. Whiston, I.L. Azevedo, S. Litster, K.S. Whitefoot, C. Samaras, J.F. Whitacre, Expert assessments of the cost and expected future performance of proton exchange membrane fuel cells for vehicles, Proc. Natl. Acad. Sci. 116 (2019) 4899–4904. https://doi.org/10.1073/pnas.1804221116.

[13] Y. Wang, D.F. Ruiz Diaz, K.S. Chen, Z. Wang, X.C. Adroher, Materials, technological status, and fundamentals of PEM fuel cells – A review, Mater. Today. 32 (2020) 178–203. https://doi.org/10.1016/j.mattod.2019.06.005.

[14] Y. Sun, S. Polani, F. Luo, S. Ott, P. Strasser, F. Dionigi, Advancements in cathode catalyst and cathode layer design for proton exchange membrane fuel cells, Nat. Commun. 12 (2021) 5984. https://doi.org/10.1038/s41467-021-25911-x.

[15] M. Orru, H. Orru, Sustainable use of Estonian peat reserves and environmental challenges, Est. J. Earth Sci. 57 (2008) 87. https://doi.org/10.3176/earth.2008.2.04.

[16] E4tech, The Fuel Cell Industry Review 2021, (2022). www.FuelCellIndustryReview.com (accessed May 22, 2023).

[17] M.B. Sassin, Y. Garsany, R.W. Atkinson, R.M.E. Hjelm, K.E. Swider-Lyons, Understanding the interplay between cathode catalyst layer porosity and thickness on transport limitations en route to high-performance PEMFCs, Int. J. Hydrog. Energy. 44 (2019) 16944–16955. https://doi.org/10.1016/j.ijhydene.2019.04.194.
[18] M. Mandal, G. Huang, N.U. Hassan, X. Peng, T. Gu, A.H. Brooks-Starks, B. Bahar, W.E. Mustain, P.A. Kohl, The Importance of Water Transport in High Conductivity and High-Power Alkaline Fuel Cells, J. Electrochem. Soc. 167 (2019) 054501. https://doi.org/10.1149/2.0022005JES.
[19] T.J. Omasta, L. Wang, X. Peng, C.A. Lewis, J.R. Varcoe, W.E. Mustain, Importance of balancing membrane and electrode water in anion exchange membrane fuel cells, J. Power Sources. 375 (2018) 205–213. https://doi.org/10.1016/j.jpowsour.2017.05.006.
[20] Y. Garsany, C.H. Bancroft, R.W. Atkinson III, K. Bethune, B.D. Gould, K.E. Swider-Lyons, Effect of GDM Pairing on PEMFC Performance in Flow-Through and Dead-Ended Anode Mode, Molecules. 25 (2020) 1469. https://doi.org/10.3390/molecules25061469.
[21] O.T. Holton, J.W. Stevenson, The Role of Platinum in Proton Exchange Membrane Fuel Cells, Platin. Met. Rev. 57 (2013) 259–271. https://doi.org/10.1595/147106713X671222.
[22] H.A. Gasteiger, J.E. Panels, S.G. Yan, Dependence of PEM fuel cell performance on catalyst loading, J. Power Sources. 127 (2004) 162–171. https://doi.org/10.1016/j.jpowsour.2003.09.013.
[23] D. Banham, J. Zou, S. Mukerjee, Z. Liu, D. Yang, Y. Zhang, Y. Peng, A. Dong, Ultralow platinum loading proton exchange membrane fuel cells: Performance losses and solutions, J. Power Sources. 490 (2021) 229515. https://doi.org/10.1016/j.jpowsour.2021.229515.
[24] Y. Horiuchi, T. Terada, A. Hori, N. Mizutani, H. Yoshikawa, Y. Itoh, Fuel cell electrode catalyst and method for producing the same, US10950869B2, 2021. https://patents.google.com/patent/US10950869B2/en (accessed May 22, 2023).
[25] K. Jiao, J. Xuan, Q. Du, Z. Bao, B. Xie, B. Wang, Y. Zhao, L. Fan, H. Wang, Z. Hou, S. Huo, N.P. Brandon, Y. Yin, M.D. Guiver, Designing the next generation of proton-exchange membrane fuel cells, Nature. 595 (2021) 361–369. https://doi.org/10.1038/s41586-021-03482-7.
[26] W. Grot, Laminates of support material and fluorinated polymer containing pendant side chains containing sulfonyl groups, US3770567A, 1973. https://patents.google.com/patent/US3770567A/en (accessed May 22, 2023).
[27] S.J. Peighambardoust, S. Rowshanzamir, M. Amjadi, Review of the proton exchange membranes for fuel cell applications, Int. J. Hydrog. Energy. 35 (2010) 9349–9384. https://doi.org/10.1016/j.ijhydene.2010.05.017.
[28] W.E. Mustain, M. Chatenet, M. Page, Y.S. Kim, Durability challenges of anion exchange membrane fuel cells, Energy Environ. Sci. 13 (2020) 2805–2838. https://doi.org/10.1039/D0EE01133A.
[29] J. Stacy, Y.N. Regmi, B. Leonard, M. Fan, The recent progress and future of oxygen reduction reaction catalysis: A review, Renew. Sustain. Energy Rev. 69 (2017) 401–414. https://doi.org/10.1016/j.rser.2016.09.135.
[30] L. Osmieri, J. Park, D.A. Cullen, P. Zelenay, D.J. Myers, K.C. Neyerlin, Status and challenges for the application of platinum group metal-free catalysts in proton-exchange membrane fuel cells, Curr. Opin. Electrochem. 25 (2021) 100627. https://doi.org/10.1016/j.coelec.2020.08.009.

[31] X. Li, G. Liu, B.N. Popov, Activity and stability of non-precious metal catalysts for oxygen reduction in acid and alkaline electrolytes, J. Power Sources. 195 (2010) 6373–6378. https://doi.org/10.1016/j.jpowsour.2010.04.019.
[32] P.G. Santori, F.D. Speck, J. Li, A. Zitolo, Q. Jia, S. Mukerjee, S. Cherevko, F. Jaouen, Effect of Pyrolysis Atmosphere and Electrolyte pH on the Oxygen Reduction Activity, Stability and Spectroscopic Signature of FeNx Moieties in Fe-N-C Catalysts, J. Electrochem. Soc. 166 (2019) F3311–F3320. https://doi.org/10.1149/2.0371907jes.
[33] D. Banham, S. Ye, K. Pei, J. Ozaki, T. Kishimoto, Y. Imashiro, A review of the stability and durability of non-precious metal catalysts for the oxygen reduction reaction in proton exchange membrane fuel cells, J. Power Sources. 285 (2015) 334–348. https://doi.org/10.1016/j.jpowsour.2015.03.047.
[34] A.G. Wright, J. Fan, B. Britton, T. Weissbach, H.-F. Lee, E.A. Kitching, T.J. Peckham, S. Holdcroft, Hexamethyl-p-terphenyl poly(benzimidazolium): a universal hydroxide-conducting polymer for energy conversion devices, Energy Environ. Sci. 9 (2016) 2130–2142. https://doi.org/10.1039/C6EE00656F.
[35] S. Noh, J.Y. Jeon, S. Adhikari, Y.S. Kim, C. Bae, Molecular Engineering of Hydroxide Conducting Polymers for Anion Exchange Membranes in Electrochemical Energy Conversion Technology, Acc. Chem. Res. 52 (2019) 2745–2755. https://doi.org/10.1021/acs.accounts.9b00355.
[36] N. Li, M.D. Guiver, W.H. Binder, Towards High Conductivity in Anion-Exchange Membranes for Alkaline Fuel Cells, ChemSusChem. 6 (2013) 1376–1383. https://doi.org/10.1002/cssc.201300320.
[37] M. Mandal, G. Huang, P.A. Kohl, Anionic multiblock copolymer membrane based on vinyl addition polymerization of norbornenes: Applications in anion-exchange membrane fuel cells, J. Membr. Sci. 570–571 (2019) 394–402. https://doi.org/10.1016/j.memsci.2018.10.041.
[38] X. Chu, L. Liu, Y. Huang, M.D. Guiver, N. Li, Practical implementation of bis-six-membered N-cyclic quaternary ammonium cations in advanced anion exchange membranes for fuel cells: Synthesis and durability, J. Membr. Sci. 578 (2019) 239–250. https://doi.org/10.1016/j.memsci.2019.02.051.
[39] J. Fan, S. Willdorf-Cohen, E.M. Schibli, Z. Paula, W. Li, T.J.G. Skalski, A.T. Sergeenko, A. Hohenadel, B.J. Frisken, E. Magliocca, W.E. Mustain, C.E. Diesendruck, D.R. Dekel, S. Holdcroft, Poly(bis-arylimidazoliums) possessing high hydroxide ion exchange capacity and high alkaline stability, Nat. Commun. 10 (2019) 2306. https://doi.org/10.1038/s41467-019-10292-z.
[40] Fuel Cell Stacks, (2023). https://www.fuelcellstore.com/fuel-cell-stacks (accessed May 22, 2023).
[41] Batelle Memorial Institute, Manufacturing Cost Analysis of 100 and 250 kW Fuel Cell Systems for Primary Power and Combined Heat and Power Applications, (2016). https://www.energy.gov/eere/fuelcells/articles/manufacturing-cost-analysis-100-and-250-kw-fuel-cell-systems-primary-power (accessed May 22, 2023).
[42] Hydrogen Council, Path to hydrogen competitiveness: A cost perspective, (2020). https://hydrogencouncil.com/en/path-to-hydrogen-competitiveness-a-cost-perspective/ (accessed May 22, 2023).
[43] Platinum: mine production worldwide 2022, Statista. (2022). https://www.statista.com/statistics/1170691/mine-production-of-platinum-worldwide/ (accessed May 22, 2023).

[44] G. Reverdiau, A. Le Duigou, T. Alleau, T. Aribart, C. Dugast, T. Priem, Will there be enough platinum for a large deployment of fuel cell electric vehicles?, Int. J. Hydrog. Energy. 46 (2021) 39195–39207. https://doi.org/10.1016/j.ijhydene.2021.09.149.
[45] B.D. James, J.M. Huya-Kouadio, C. Houchins, D.A. DeSantis, S. Analysis, Mass Production Cost Estimation of Direct H2 PEM Fuel Cell Systems for Transportation Applications: 2018 Update, (2018) 355.
[46] Worldwide automobile production, Statista. (2021). https://www.statista.com/statistics/262747/worldwide-automobile-production-since-2000/ (accessed May 22, 2023).
[47] F. Jaouen, E. Proietti, M. Lefèvre, R. Chenitz, J.-P. Dodelet, G. Wu, H.T. Chung, C.M. Johnston, P. Zelenay, Recent advances in non-precious metal catalysis for oxygen-reduction reaction in polymer electrolyte fuel cells, Energy Env. Sci. 4 (2011) 114–130. https://doi.org/10.1039/c0ee00011f.
[48] S. Gupta, D. Tryk, I. Bae, W. Aldred, E. Yeager, Heat-treated polyacrylonitrile-based catalysts for oxygen electroreduction, J. Appl. Electrochem. 19 (1989) 19–27. https://doi.org/10.1007/BF01039385.
[49] Z. Chen, D. Higgins, A. Yu, L. Zhang, J. Zhang, A review on non-precious metal electrocatalysts for PEM fuel cells, Energy Environ. Sci. 4 (2011) 3167–3192. https://doi.org/10.1039/C0EE00558D.
[50] S. Li, L. Zhang, J. Kim, M. Pan, Z. Shi, J. Zhang, Synthesis of carbon-supported binary FeCo–N non-noble metal electrocatalysts for the oxygen reduction reaction, Electrochimica Acta. 55 (2010) 7346–7353. https://doi.org/10.1016/j.electacta.2010.07.020.
[51] G. Wu, C.M. Johnston, N.H. Mack, K. Artyushkova, M. Ferrandon, M. Nelson, J.S. Lezama-Pacheco, S.D. Conradson, K.L. More, D.J. Myers, P. Zelenay, Synthesis–structure–performance correlation for polyaniline–Me–C non-precious metal cathode catalysts for oxygen reduction in fuel cells, J Mater Chem. 21 (2011) 11392–11405. https://doi.org/10.1039/C0JM03613G.
[52] J. Lilloja, E. Kibena-Põldsepp, A. Sarapuu, M. Kodali, Y. Chen, T. Asset, M. Käärik, M. Merisalu, P. Paiste, J. Aruväli, A. Treshchalov, M. Rähn, J. Leis, V. Sammelselg, S. Holdcroft, P. Atanassov, K. Tammeveski, Cathode Catalysts Based on Cobalt- and Nitrogen-Doped Nanocarbon Composites for Anion Exchange Membrane Fuel Cells, ACS Appl. Energy Mater. 3 (2020) 5375–5384. https://doi.org/10.1021/acsaem.0c00381.
[53] S. Ratso, I. Kruusenberg, M. Käärik, M. Kook, L. Puust, R. Saar, J. Leis, K. Tammeveski, Highly efficient transition metal and nitrogen co-doped carbide-derived carbon electrocatalysts for anion exchange membrane fuel cells, J. Power Sources. 375 (2018) 233–243. https://doi.org/10.1016/j.jpowsour.2017.08.046.
[54] S. Gupta, S. Zhao, O. Ogoke, Y. Lin, H. Xu, G. Wu, Engineering Favorable Morphology and Structure of Fe-N-C Oxygen-Reduction Catalysts through Tuning of Nitrogen/Carbon Precursors, ChemSusChem. 10 (2017) 774–785. https://doi.org/10.1002/cssc.201601397.
[55] S. Akula, M. Mooste, B. Zulevi, S. McKinney, A. Kikas, H.-M. Piirsoo, M. Rähn, A. Tamm, V. Kisand, A. Serov, E.B. Creel, D.A. Cullen, K.C. Neyerlin, H. Wang, M. Odgaard, T. Reshetenko, K. Tammeveski, Mesoporous textured Fe-N-C electrocatalysts as highly efficient cathodes for proton exchange membrane fuel cells, J. Power Sources. 520 (2022) 230819. https://doi.org/10.1016/j.jpowsour.2021.230819.

[56] Md.M. Hossen, Md.S. Hasan, Md.R.I. Sardar, J. bin Haider, Mottakin, K. Tammeveski, P. Atanassov, State-of-the-art and developmental trends in platinum group metal-free cathode catalyst for anion exchange membrane fuel cell (AEMFC), Appl. Catal. B Environ. 325 (2023) 121733. https://doi.org/10.1016/j.apcatb.2022.121733.
[57] T. Asset, P. Atanassov, Iron-Nitrogen-Carbon Catalysts for Proton Exchange Membrane Fuel Cells, Joule. 4 (2020) 33–44. https://doi.org/10.1016/j.joule.2019.12.002.
[58] J.K. Dombrovskis, A.E.C. Palmqvist, Recent Progress in Synthesis, Characterization and Evaluation of Non-Precious Metal Catalysts for the Oxygen Reduction Reaction, Fuel Cells. 16 (2016) 4–22. https://doi.org/10.1002/fuce.201500123.
[59] U.I. Kramm, I. Abs-Wurmbach, I. Herrmann-Geppert, J. Radnik, S. Fiechter, P. Bogdanoff, Influence of the Electron-Density of FeN4-Centers Towards the Catalytic Activity of Pyrolyzed FeTMPPCl-Based ORR-Electrocatalysts, J. Electrochem. Soc. 158 (2010) B69. https://doi.org/10.1149/1.3499621.
[60] A. Zitolo, N. Ranjbar-Sahraie, T. Mineva, J. Li, Q. Jia, S. Stamatin, G.F. Harrington, S.M. Lyth, P. Krtil, S. Mukerjee, E. Fonda, F. Jaouen, Identification of catalytic sites in cobalt-nitrogen-carbon materials for the oxygen reduction reaction, Nat. Commun. 8 (2017) 957. https://doi.org/10.1038/s41467-017-01100-7.
[61] I. Matanovic, K. Artyushkova, P. Atanassov, Understanding PGM-free catalysts by linking density functional theory calculations and structural analysis: Perspectives and challenges, Curr. Opin. Electrochem. 9 (2018) 137–144. https://doi.org/10.1016/j.coelec.2018.03.009.
[62] Y. He, S. Hwang, D.A. Cullen, M.A. Uddin, L. Langhorst, B. Li, S. Karakalos, A.J. Kropf, E.C. Wegener, J. Sokolowski, M. Chen, D. Myers, D. Su, K.L. More, G. Wang, S. Litster, G. Wu, Highly active atomically dispersed CoN4 fuel cell cathode catalysts derived from surfactant-assisted MOFs: carbon-shell confinement strategy, Energy Environ. Sci. 12 (2019) 250–260. https://doi.org/10.1039/C8EE02694G.
[63] H.T. Chung, D.A. Cullen, D. Higgins, B.T. Sneed, E.F. Holby, K.L. More, P. Zelenay, Direct atomic-level insight into the active sites of a high-performance PGM-free ORR catalyst, Science. 357 (2017) 479–484. https://doi.org/10.1126/science.aan2255.
[64] S. Kabir, K. Artyushkova, A. Serov, P. Atanassov, Role of Nitrogen Moieties in N-Doped 3D-Graphene Nanosheets for Oxygen Electroreduction in Acidic and Alkaline Media, ACS Appl. Mater. Interfaces. 10 (2018) 11623–11632. https://doi.org/10.1021/acsami.7b18651.
[65] L. Lai, J.R. Potts, D. Zhan, L. Wang, C.K. Poh, C. Tang, H. Gong, Z. Shen, J. Lin, R.S. Ruoff, Exploration of the active center structure of nitrogen-doped graphene-based catalysts for oxygen reduction reaction, Energy Environ. Sci. 5 (2012) 7936–7942. https://doi.org/10.1039/C2EE21802J.
[66] K. Artyushkova, A. Serov, S. Rojas-Carbonell, P. Atanassov, Chemistry of Multitudinous Active Sites for Oxygen Reduction Reaction in Transition Metal–Nitrogen–Carbon Electrocatalysts, J. Phys. Chem. C. 119 (2015) 25917–25928. https://doi.org/10.1021/acs.jpcc.5b07653.
[67] Y. Shao, J.-P. Dodelet, G. Wu, P. Zelenay, PGM-Free Cathode Catalysts for PEM Fuel Cells: A Mini-Review on Stability Challenges, Adv. Mater. 31 (2019) 1807615. https://doi.org/10.1002/adma.201807615.

[68] M. Chen, Y. He, J.S. Spendelow, G. Wu, Atomically Dispersed Metal Catalysts for Oxygen Reduction, ACS Energy Lett. 4 (2019) 1619–1633. https://doi.org/10.1021/acsenergylett.9b00804.
[69] U.I. Kramm, I. Herrmann-Geppert, J. Behrends, K. Lips, S. Fiechter, P. Bogdanoff, On an Easy Way To Prepare Metal–Nitrogen Doped Carbon with Exclusive Presence of MeN4-type Sites Active for the ORR, J. Am. Chem. Soc. 138 (2016) 635–640. https://doi.org/10.1021/jacs.5b11015.
[70] X.X. Wang, D.A. Cullen, Y.-T. Pan, S. Hwang, M. Wang, Z. Feng, J. Wang, M.H. Engelhard, H. Zhang, Y. He, Y. Shao, D. Su, K.L. More, J.S. Spendelow, G. Wu, Nitrogen-coordinated single cobalt atom catalysts for oxygen reduction in proton exchange membrane fuel cells, Adv Mater. 30 (2018) 1706758. https://doi.org/10.1002/adma.201706758.
[71] Y. He, S. Liu, C. Priest, Q. Shi, G. Wu, Atomically dispersed metal–nitrogen–carbon catalysts for fuel cells: advances in catalyst design, electrode performance, and durability improvement, Chem. Soc. Rev. 49 (2020) 3484–3524. https://doi.org/10.1039/C9CS00903E.
[72] H. Zhang, S. Hwang, M. Wang, Z. Feng, S. Karakalos, L. Luo, Z. Qiao, X. Xie, C. Wang, D. Su, Y. Shao, G. Wu, Single Atomic Iron Catalysts for Oxygen Reduction in Acidic Media: Particle Size Control and Thermal Activation, J. Am. Chem. Soc. 139 (2017) 14143–14149. https://doi.org/10.1021/jacs.7b06514.
[73] J. Li, H. Zhang, W. Samarakoon, W. Shan, D.A. Cullen, S. Karakalos, M. Chen, D. Gu, K.L. More, G. Wang, Z. Feng, Z. Wang, G. Wu, Thermally Driven Structure and Performance Evolution of Atomically Dispersed FeN4 Sites for Oxygen Reduction, Angew. Chem. Int. Ed. 58 (2019) 18971–18980. https://doi.org/10.1002/anie.201909312.
[74] A. Velázquez-Palenzuela, L. Zhang, L. Wang, P.L. Cabot, E. Brillas, K. Tsay, J. Zhang, Fe–Nx/C electrocatalysts synthesized by pyrolysis of Fe(II)–2,3,5,6-tetra(2-pyridyl)pyrazine complex for PEM fuel cell oxygen reduction reaction, Electrochim Acta. 56 (2011) 4744–4752. https://doi.org/10.1016/j.electacta.2011.03.059.
[75] J. Liu, Y. Liu, P. Li, L. Wang, H. Zhang, H. Liu, J. Liu, Y. Wang, W. Tian, X. Wang, Z. Li, M. Wu, Fe-N-doped porous carbon from petroleum asphalt for highly efficient oxygen reduction reaction, Carbon. 126 (2018) 1–8. https://doi.org/10.1016/j.carbon.2017.10.004.
[76] M. Thommes, K. Kaneko, A.V. Neimark, J.P. Olivier, F. Rodriguez-Reinoso, J. Rouquerol, K.S.W. Sing, Physisorption of gases, with special reference to the evaluation of surface area and pore size distribution (IUPAC Technical Report), Pure Appl. Chem. 87 (2015) 1051–1069. https://doi.org/10.1515/pac-2014-1117.
[77] F. Jaouen, M. Lefèvre, J.-P. Dodelet, M. Cai, Heat-Treated Fe/N/C Catalysts for O2 Electroreduction: Are Active Sites Hosted in Micropores?, J. Phys. Chem. B. 110 (2006) 5553–5558. https://doi.org/10.1021/jp057135h.
[78] R. Chenitz, U.I. Kramm, M. Lefèvre, V. Glibin, G. Zhang, S. Sun, J.-P. Dodelet, A specific demetalation of Fe–N4 catalytic sites in the micropores of NC_Ar + NH3 is at the origin of the initial activity loss of the highly active Fe/N/C catalyst used for the reduction of oxygen in PEM fuel cells, Energy Environ. Sci. 11 (2018) 365–382. https://doi.org/10.1039/C7EE02302B.
[79] J. Li, S. Ghoshal, W. Liang, M.-T. Sougrati, F. Jaouen, B. Halevi, S. McKinney, G. McCool, C. Ma, X. Yuan, Z.-F. Ma, S. Mukerjee, Q. Jia, Structural and mecha-

nistic basis for the high activity of Fe–N–C catalysts toward oxygen reduction, Energy Environ. Sci. 9 (2016) 2418–2432. https://doi.org/10.1039/C6EE01160H.
[80] S. Park, M. Her, H. Shin, W. Hwang, Y.-E. Sung, Maximizing the Active Site Densities of Single-Atomic Fe–N–C Electrocatalysts for High-Performance Anion Membrane Fuel Cells, ACS Appl. Energy Mater. 4 (2021) 1459–1466. https://doi.org/10.1021/acsaem.0c02650.
[81] T. Kyotani, Control of pore structure in carbon, Carbon. 38 (2000) 269–286. https://doi.org/10.1016/S0008-6223(99)00142-6.
[82] M. Härmas, T. Thomberg, H. Kurig, T. Romann, A. Jänes, E. Lust, Microporous–mesoporous carbons for energy storage synthesized by activation of carbonaceous material by zinc chloride, potassium hydroxide or mixture of them, J. Power Sources. 326 (2016) 624–634. https://doi.org/10.1016/j.jpowsour.2016.04.038.
[83] F. Caturla, M. Molina-Sabio, F. Rodríguez-Reinoso, Preparation of activated carbon by chemical activation with ZnCl2, Carbon. 29 (1991) 999–1007. https://doi.org/10.1016/0008-6223(91)90179-M.
[84] PubChem, Zinc Chloride, (2023). https://pubchem.ncbi.nlm.nih.gov/compound/5727 (accessed May 29, 2023).
[85] S. Ratso, M.T. Sougrati, M. Käärik, M. Merisalu, M. Rähn, V. Kisand, A. Kikas, P. Paiste, J. Leis, V. Sammelselg, F. Jaouen, K. Tammeveski, Effect of Ball-Milling on the Oxygen Reduction Reaction Activity of Iron and Nitrogen Co-doped Carbide-Derived Carbon Catalysts in Acid Media, ACS Appl. Energy Mater. 2 (2019) 7952–7962. https://doi.org/10.1021/acsaem.9b01430.
[86] R. Muzyka, E. Misztal, J. Hrabak, S.W. Banks, M. Sajdak, Various biomass pyrolysis conditions influence the porosity and pore size distribution of biochar, Energy. 263 (2023) 126128. https://doi.org/10.1016/j.energy.2022.126128.
[87] K.-Y. Cheung, K.-L. Lee, K.-L. Lam, T.-Y. Chan, C.-W. Lee, C.-W. Hui, Operation strategy for multi-stage pyrolysis, J. Anal. Appl. Pyrolysis. 91 (2011) 165–182. https://doi.org/10.1016/j.jaap.2011.02.004.
[88] X. Zhang, H. Li, K. Zhang, Q. Wang, B. Qin, Q. Cao, L. Jin, Strategy for Preparing Porous Graphitic Carbon for Supercapacitor: Balance on Porous Structure and Graphitization Degree, J. Electrochem. Soc. 165 (2018) A2084. https://doi.org/10.1149/2.0491910jes.
[89] K. Artyushkova, S. Rojas-Carbonell, C. Santoro, E. Weiler, A. Serov, R. Awais, R.R. Gokhale, P. Atanassov, Correlations between Synthesis and Performance of Fe-Based PGM-Free Catalysts in Acidic and Alkaline Media: Evolution of Surface Chemistry and Morphology, ACS Appl. Energy Mater. 2 (2019) 5406–5418. https://doi.org/10.1021/acsaem.9b00331.
[90] Y. Huang, Y. Chen, M. Xu, T. Asset, P. Tieu, A. Gili, D. Kulkarni, V. De Andrade, F. De Carlo, H.S. Barnard, A. Doran, D.Y. Parkinson, X. Pan, P. Atanassov, I.V. Zenyuk, Catalysts by pyrolysis: Direct observation of chemical and morphological transformations leading to transition metal-nitrogen-carbon materials, Mater. Today. 47 (2021) 53–68. https://doi.org/10.1016/j.mattod.2021.02.006.
[91] S. Li, C. Cheng, X. Zhao, J. Schmidt, A. Thomas, Active Salt/Silica-Templated 2D Mesoporous FeCo-Nx-Carbon as Bifunctional Oxygen Electrodes for Zinc–Air Batteries, Angew. Chem. Int. Ed. 57 (2018) 1856–1862. https://doi.org/10.1002/anie.201710852.

[92] L. Osmieri, R. Escudero-Cid, A.H.A. Monteverde Videla, P. Ocón, S. Specchia, Performance of a Fe-N-C catalyst for the oxygen reduction reaction in direct methanol fuel cell: Cathode formulation optimization and short-term durability, Appl Catal B. 201 (2017) 253–265. https://doi.org/10.1016/j.apcatb.2016.08.043.
[93] Y. Hua, T. Jiang, K. Wang, M. Wu, S. Song, Y. Wang, P. Tsiakaras, Efficient Pt-free electrocatalyst for oxygen reduction reaction: Highly ordered mesoporous N and S co-doped carbon with saccharin as single-source molecular precursor, Appl Catal B. 194 (2016) 202–208. https://doi.org/10.1016/j.apcatb.2016.04.056.
[94] T. Morishita, T. Tsumura, M. Toyoda, J. Przepiórski, A.W. Morawski, H. Konno, M. Inagaki, A review of the control of pore structure in MgO-templated nanoporous carbons, Carbon. 48 (2010) 2690–2707. https://doi.org/10.1016/j.carbon.2010.03.064.
[95] S. Zhu, N. Zhao, J. Li, X. Deng, J. Sha, C. He, Hard-template synthesis of three-dimensional interconnected carbon networks: Rational design, hybridization and energy-related applications, Nano Today. 29 (2019) 100796. https://doi.org/10.1016/j.nantod.2019.100796.
[96] K. Kisand, A. Sarapuu, J.C. Douglin, A. Kikas, A. Treshchalov, M. Käärik, H.-M. Piirsoo, P. Paiste, J. Aruväli, J. Leis, V. Kisand, A. Tamm, D.R. Dekel, K. Tammeveski, Templated Nitrogen-, Iron-, and Cobalt-Doped Mesoporous Nanocarbon Derived from an Alkylresorcinol Mixture for Anion-Exchange Membrane Fuel Cell Application, ACS Catal. 12 (2022) 14050–14061. https://doi.org/10.1021/acscatal.2c03683.
[97] X. Peng, T.J. Omasta, E. Magliocca, L. Wang, J.R. Varcoe, W.E. Mustain, Nitrogen-doped Carbon–CoOx Nanohybrids: A Precious Metal Free Cathode that Exceeds 1.0 W cm−2 Peak Power and 100 h Life in Anion-Exchange Membrane Fuel Cells, Angew. Chem. 131 (2019) 1058–1063. https://doi.org/10.1002/ange.201811099.
[98] C. Shuai, Y. Zhou, Y. Yang, P. Feng, L. Liu, C. He, M. Zhao, S. Yang, C. Gao, P. Wu, Biodegradation Resistance and Bioactivity of Hydroxyapatite Enhanced Mg-Zn Composites via Selective Laser Melting, Materials. 10 (2017) 307. https://doi.org/10.3390/ma10030307.
[99] Z. Shi, X. Huang, Y. Cai, R. Tang, D. Yang, Size effect of hydroxyapatite nanoparticles on proliferation and apoptosis of osteoblast-like cells, Acta Biomater. 5 (2009) 338–345. https://doi.org/10.1016/j.actbio.2008.07.023.
[100] Y. Cai, Y. Liu, W. Yan, Q. Hu, J. Tao, M. Zhang, Z. Shi, R. Tang, Role of hydroxyapatite nanoparticle size in bone cell proliferation, J. Mater. Chem. 17 (2007) 3780–3787. https://doi.org/10.1039/B705129H.
[101] A.J. Bard, L.R. Faulkner, Electrochemical Methods: Fundamentals and Applications, 2nd Edition, Wiley Textbooks, 2000.
[102] J. Masa, C. Batchelor-McAuley, W. Schuhmann, R.G. Compton, Koutecky-Levich analysis applied to nanoparticle modified rotating disk electrodes: Electrocatalysis or misinterpretation, Nano Res. 7 (2014) 71–78. https://doi.org/10.1007/s12274-013-0372-0.
[103] R.G. Compton, S.V. Sokolov, Electrochemistry needs electrochemists: “goodbye to rotating discs,” J. Solid State Electrochem. (2023). https://doi.org/10.1007/s10008-023-05443-8.
[104] L. Bouleau, S. Pérez-Rodríguez, J. Quílez-Bermejo, M.T. Izquierdo, F. Xu, V. Fierro, A. Celzard, Best practices for ORR performance evaluation of metal-free porous carbon electrocatalysts, Carbon. 189 (2022) 349–361.

https://doi.org/10.1016/j.carbon.2021.12.078.
[105] G. Wu, K.L. More, C.M. Johnston, P. Zelenay, High-performance electrocatalysts for oxygen reduction derived from polyaniline, iron, and cobalt, Science. 332 (2011) 443–447. https://doi.org/10.1126/science.1200832.
[106] H. Zhang, H.T. Chung, D.A. Cullen, S. Wagner, U.I. Kramm, K.L. More, P. Zelenay, G. Wu, High-performance fuel cell cathodes exclusively containing atomically dispersed iron active sites, Energy Environ. Sci. 12 (2019) 2548–2558. https://doi.org/10.1039/C9EE00877B.
[107] K. Shinozaki, J.W. Zack, R.M. Richards, B.S. Pivovar, S.S. Kocha, Oxygen Reduction Reaction Measurements on Platinum Electrocatalysts Utilizing Rotating Disk Electrode Technique I. Impact of Impurities, Measurement Protocols and Applied Corrections, J. Electrochem. Soc. 162 (2015) F1144–F1158. https://doi.org/10.1149/2.1071509jes.
[108] H. Adabi, P.G. Santori, A. Shakouri, X. Peng, K. Yassin, I.G. Rasin, S. Brandon, D.R. Dekel, N.U. Hassan, M.-T. Sougrati, A. Zitolo, J.R. Varcoe, J.R. Regalbuto, F. Jaouen, W.E. Mustain, Understanding how single-atom site density drives the performance and durability of PGM-free Fe–N–C cathodes in anion exchange membrane fuel cells, Mater. Today Adv. 12 (2021) 100179. https://doi.org/10.1016/j.mtadv.2021.100179.
[109] H. Su, S. Zhou, X. Zhang, H. Sun, H. Zhang, Y. Xiao, K. Yu, Z. Dong, X. Dai, X. Huang, Metal–organic frameworks-derived core–shell Fe3O4/Fe3N@graphite carbon nanocomposites as excellent non-precious metal electrocatalyst for oxygen reduction, Dalton Trans. 47 (2018) 16567–16577. https://doi.org/10.1039/C8DT02250J.
[110] H.T. Chung, J.H. Won, P. Zelenay, Active and stable carbon nanotube/nanoparticle composite electrocatalyst for oxygen reduction, Nat. Commun. 4 (2013) 1922. https://doi.org/10.1038/ncomms2944.
[111] S. Ratso, A. Zitolo, M. Käärik, M. Merisalu, A. Kikas, V. Kisand, M. Rähn, P. Paiste, J. Leis, V. Sammelselg, S. Holdcroft, F. Jaouen, K. Tammeveski, Non-precious metal cathodes for anion exchange membrane fuel cells from ball-milled iron and nitrogen doped carbide-derived carbons, Renew. Energy. 167 (2021) 800–810. https://doi.org/10.1016/j.renene.2020.11.154.
[112] T. Lazaridis, B.M. Stühmeier, H.A. Gasteiger, H.A. El-Sayed, Capabilities and limitations of rotating disk electrodes versus membrane electrode assemblies in the investigation of electrocatalysts, Nat. Catal. 5 (2022) 363–373. https://doi.org/10.1038/s41929-022-00776-5.
[113] S.A. Mauger, J.R. Pfeilsticker, M. Wang, S. Medina, A.C. Yang-Neyerlin, K.C. Neyerlin, C. Stetson, S. Pylypenko, M. Ulsh, Fabrication of high-performance gas-diffusion-electrode based membrane-electrode assemblies, J. Power Sources. 450 (2020) 227581. https://doi.org/10.1016/j.jpowsour.2019.227581.
[114] D. Banham, J.-Y. Choi, T. Kishimoto, S. Ye, Integrating PGM-Free Catalysts into Catalyst Layers and Proton Exchange Membrane Fuel Cell Devices, Adv. Mater. 31 (2019) 1804846. https://doi.org/10.1002/adma.201804846.
[115] X. Peng, D. Kulkarni, Y. Huang, T.J. Omasta, B. Ng, Y. Zheng, L. Wang, J.M. LaManna, D.S. Hussey, J.R. Varcoe, I.V. Zenyuk, W.E. Mustain, Using operando techniques to understand and design high performance and stable alkaline membrane fuel cells, Nat. Commun. 11 (2020) 3561. https://doi.org/10.1038/s41467-020-17370-7.

[116] H. Deng, D. Wang, X. Xie, Y. Zhou, Y. Yin, Q. Du, K. Jiao, Modeling of hydrogen alkaline membrane fuel cell with interfacial effect and water management optimization, Renew. Energy. 91 (2016) 166–177. https://doi.org/10.1016/j.renene.2016.01.054.
[117] T.J. Omasta, A.M. Park, J.M. LaManna, Y. Zhang, X. Peng, L. Wang, D.L. Jacobson, J.R. Varcoe, D.S. Hussey, B.S. Pivovar, W.E. Mustain, Beyond catalysis and membranes: visualizing and solving the challenge of electrode water accumulation and flooding in AEMFCs, Energy Environ. Sci. 11 (2018) 551–558. https://doi.org/10.1039/C8EE00122G.
[118] Q. Wang, Y. Yang, F. Sun, G. Chen, J. Wang, L. Peng, W.-T. Chen, L. Shang, J. Zhao, D. Sun-Waterhouse, T. Zhang, G.I.N. Waterhouse, Molten NaCl-Assisted Synthesis of Porous Fe-N-C Electrocatalysts with a High Density of Catalytically Accessible FeN4 Active Sites and Outstanding Oxygen Reduction Reaction Performance, Adv. Energy Mater. 11 (2021) 2100219. https://doi.org/10.1002/aenm.202100219.
[119] H. Adabi, A. Shakouri, N. Ul Hassan, J.R. Varcoe, B. Zulevi, A. Serov, J.R. Regalbuto, W.E. Mustain, High-performing commercial Fe–N–C cathode electrocatalyst for anion-exchange membrane fuel cells, Nat. Energy. 6 (2021) 834–843. https://doi.org/10.1038/s41560-021-00878-7.
[120] H.A. Firouzjaie, W.E. Mustain, Catalytic Advantages, Challenges, and Priorities in Alkaline Membrane Fuel Cells, ACS Catal. 10 (2020) 225–234. https://doi.org/10.1021/acscatal.9b03892.
[121] Activated Carbon Market Size & Trends Analysis Report, 2030, (2022). https://www.grandviewresearch.com/industry-analysis/activated-carbon-market (accessed May 25, 2023).
[122] A.J. Ragauskas, C.K. Williams, B.H. Davison, G. Britovsek, J. Cairney, C.A. Eckert, W.J. Frederick, J.P. Hallett, D.J. Leak, C.L. Liotta, J.R. Mielenz, R. Murphy, R. Templer, T. Tschaplinski, The Path Forward for Biofuels and Biomaterials, Science. 311 (2006) 484–489. https://doi.org/10.1126/science.1114736.
[123] J. Deng, M. Li, Y. Wang, Biomass-derived carbon: synthesis and applications in energy storage and conversion, Green Chem. 18 (2016) 4824–4854. https://doi.org/10.1039/C6GC01172A.
[124] B.M. Upton, A.M. Kasko, Strategies for the Conversion of Lignin to High-Value Polymeric Materials: Review and Perspective, Chem. Rev. 116 (2016) 2275–2306. https://doi.org/10.1021/acs.chemrev.5b00345.
[125] C. Lai, P. Kolla, Y. Zhao, H. Fong, A.L. Smirnova, Lignin-derived electrospun carbon nanofiber mats with supercritically deposited Ag nanoparticles for oxygen reduction reaction in alkaline fuel cells, Electrochimica Acta. 130 (2014) 431–438. https://doi.org/10.1016/j.electacta.2014.03.006.
[126] C. Li, Y. Wu, M. Fu, X. Zhao, S. Zhai, Y. Yan, L. Zhang, X. Zhang, Preparation of Fe/N Double Doped Carbon Nanotubes from Lignin in Pennisetum as Oxygen Reduction Reaction Electrocatalysts for Zinc–Air Batteries, ACS Appl. Energy Mater. 5 (2022) 4340–4350. https://doi.org/10.1021/acsaem.1c03956.
[127] Y. Shen, F. Peng, Y. Cao, J. Zuo, H. Wang, H. Yu, Preparation of nitrogen and sulfur co-doped ultrathin graphitic carbon via annealing bagasse lignin as potential electrocatalyst towards oxygen reduction reaction in alkaline and acid media, J. Energy Chem. 34 (2019) 33–42. https://doi.org/10.1016/j.jechem.2018.09.021.

[128] Y. Shen, Y. Li, G. Yang, Q. Zhang, H. Liang, F. Peng, Lignin derived multi-doped (N, S, Cl) carbon materials as excellent electrocatalyst for oxygen reduction reaction in proton exchange membrane fuel cells, J. Energy Chem. 44 (2020) 106–114. https://doi.org/10.1016/j.jechem.2019.09.019.
[129] Agreement reached on cutting maritime transport emissions, Eur. Comm. - Eur. Comm. (2023). https://ec.europa.eu/commission/presscorner/detail/en/ip_23_1813 (accessed May 30, 2023).
[130] Peat, Turbaliit. (2023). https://www.turbaliit.ee/en/peat/ (accessed May 30, 2023).
[131] P.H. Given, W. Spackman, P.C. Painter, C.A. Rhoads, N.J. Ryan, L. Alemany, R.J. Pugmire, The fate of cellulose and lignin in peats: an exploratory study of the input to coalification, Org. Geochem. 6 (1984) 399–407. https://doi.org/10.1016/0146-6380(84)90062-7.
[132] K. Kimmel, A. Kull, J.-O. Salm, Ü. Mander, The status, conservation and sustainable use of Estonian wetlands, Wetl. Ecol. Manag. 18 (2010) 375–395. https://doi.org/10.1007/s11273-008-9129-z.
[133] TemaNord, Peatlands and Climate in a Ramsar context: A Nordic-Baltic Perspective, 2015. http://norden.diva-portal.org/smash/get/diva2:814147/fulltext02.pdf?fbclid=IwAR23joGWMKCHsgDXPmAssksWQ8A9EfUHW5hjsgNLrY-xS8u_0rr8dIAtVgg (accessed May 25, 2023).
[134] D. Wilson, F. Mackin, J.-P. Tuovinen, G. Moser, C. Farrell, F. Renou-Wilson, Carbon and climate implications of rewetting a raised bog in Ireland, Glob. Change Biol. 28 (2022) 6349–6365. https://doi.org/10.1111/gcb.16359.
[135] M. Orru, K. Ots, H. Orru, Re-vegetation processes in cutaway peat production fields in Estonia in relation to peat quality and water regime, Environ. Monit. Assess. 188 (2016) 655. https://doi.org/10.1007/s10661-016-5669-5.
[136] M. Härmas, R. Palm, T. Thomberg, R. Härmas, M. Koppel, M. Paalo, I. Tallo, T. Romann, A. Jänes, E. Lust, Hydrothermal and peat-derived carbons as electrode materials for high-efficient electrical double-layer capacitors, J. Appl. Electrochem. 50 (2020) 15–32. https://doi.org/10.1007/s10800-019-01364-5.
[137] A. Adamson, R. Väli, M. Paalo, J. Aruväli, M. Koppel, R. Palm, E. Härk, J. Nerut, T. Romann, E. Lust, A. Jänes, Peat-derived hard carbon electrodes with superior capacity for sodium-ion batteries, RSC Adv. 10 (2020) 20145–20154. https://doi.org/10.1039/D0RA03212C.
[138] S. Sepp, J. Nerut, K. Vaarmets, R. Kanarbik, I. Tallo, E. Lust, Activity and Stability of Carbide Derived Carbon Supports in PEMFC Application, ECS Trans. 86 (2018) 507. https://doi.org/10.1149/08613.0507ecst.
[139] B. Britton, S. Holdcroft, The Control and Effect of Pore Size Distribution in AEMFC Catalyst Layers, J. Electrochem. Soc. 163 (2016) F353. https://doi.org/10.1149/2.0421605jes.
[140] N. Ul Hassan, M.J. Zachman, M. Mandal, H. Adabi Firouzjaie, P.A. Kohl, D.A. Cullen, W.E. Mustain, Understanding Recoverable vs Unrecoverable Voltage Losses and Long-Term Degradation Mechanisms in Anion Exchange Membrane Fuel Cells, ACS Catal. 12 (2022) 8116–8126. https://doi.org/10.1021/acscatal.2c01880.
[141] P. Rydelek, Origin and Composition of Mineral Constituents of Fen Peats from Eastern Poland, J. Plant Nutr. 36 (2013) 911–928. https://doi.org/10.1080/01904167.2013.770525.

[142] J. Jagiello, M. Thommes, Comparison of DFT characterization methods based on N2, Ar, CO2, and H2 adsorption applied to carbons with various pore size distributions, Carbon. 42 (2004) 1227–1232. https://doi.org/10.1016/j.carbon.2004.01.022.
[143] J. Jagiello, J. Kenvin, Consistency of carbon nanopore characteristics derived from adsorption of simple gases and 2D-NLDFT models. Advantages of using adsorption isotherms of oxygen (O2) at 77 K, J. Colloid Interface Sci. 542 (2019) 151–158. https://doi.org/10.1016/j.jcis.2019.01.116.
[144] W.-J. Jiang, L. Gu, L. Li, Y. Zhang, X. Zhang, L.-J. Zhang, J.-Q. Wang, J.-S. Hu, Z. Wei, L.-J. Wan, Understanding the High Activity of Fe–N–C Electrocatalysts in Oxygen Reduction: Fe/Fe3C Nanoparticles Boost the Activity of Fe–Nx, J. Am. Chem. Soc. 138 (2016) 3570–3578. https://doi.org/10.1021/jacs.6b00757.
[145] A. Serov, K. Artyushkova, N.I. Andersen, S. Stariha, P. Atanassov, Original Mechanochemical Synthesis of Non-Platinum Group Metals Oxygen Reduction Reaction Catalysts Assisted by Sacrificial Support Method, Electrochimica Acta. 179 (2015) 154–160. https://doi.org/10.1016/j.electacta.2015.02.108.
[146] V. Di Noto, E. Negro, A. Nale, G. Pagot, K. Vezzù, P. Atanassov, Hidden in plain sight: unlocking the full potential of cyclic voltammetry with the thin-film rotating (ring) disk electrode studies for the investigation of oxygen reduction reaction electrocatalysts, Curr. Opin. Electrochem. 25 (2021) 100626. https://doi.org/10.1016/j.coelec.2020.08.008.
[147] S. Sepp, K. Vaarmets, J. Nerut, I. Tallo, E. Tee, H. Kurig, J. Aruväli, R. Kanarbik, E. Lust, Performance of Polymer Electrolyte Membrane Fuel Cell Single Cells Prepared Using Hierarchical Microporous-Mesoporous Carbon Supported Pt Nanoparticles Activated Catalysts, Electrochim Acta. 203 (2016) 221–229. https://doi.org/10.1016/j.electacta.2016.03.158.
[148] P. Teppor, R. Jäger, E. Härk, S. Sepp, M. Kook, O. Volobujeva, P. Paiste, Z. Kochovski, I. Tallo, E. Lust, Exploring Different Synthesis Parameters for the Preparation of Metal-Nitrogen-Carbon Type Oxygen Reduction Catalysts, J. Electrochem. Soc. 167 (2020) 054513. https://doi.org/10.1149/1945-7111/ab7093.
[149] M. Carmo, G. Doubek, R.C. Sekol, M. Linardi, A.D. Taylor, Development and electrochemical studies of membrane electrode assemblies for polymer electrolyte alkaline fuel cells using FAA membrane and ionomer, J. Power Sources. 230 (2013) 169–175. https://doi.org/10.1016/j.jpowsour.2012.12.015.
[150] R. Soni, S.N. Bhange, S. Kurungot, A 3-D nanoribbon-like Pt-free oxygen reduction reaction electrocatalyst derived from waste leather for anion exchange membrane fuel cells and zinc-air batteries, Nanoscale. 11 (2019) 7893–7902. https://doi.org/10.1039/C9NR00977A.
[151] V.M. Dhavale, S.K. Singh, A. Nadeema, S.S. Gaikwad, S. Kurungot, Nanocrystalline Fe–Fe2O3 particle-deposited N-doped graphene as an activity-modulated Pt-free electrocatalyst for oxygen reduction reaction, Nanoscale. 7 (2015) 20117–20125. https://doi.org/10.1039/C5NR04929F.
[152] H.B. Aiyappa, S.N. Bhange, V.P. Sivasankaran, S. Kurungot, Single Cell Fabrication Towards the Realistic Evaluation of a CNT-Strung ZIF-Derived Electrocatalyst as a Cathode Material in Alkaline Fuel Cells and Metal−Air Batteries, ChemElectroChem. 4 (2017) 2928–2933. https://doi.org/10.1002/celc.201700562.

[153] H. Khalid, M. Najibah, H.S. Park, C. Bae, D. Henkensmeier, Properties of Anion Exchange Membranes with a Focus on Water Electrolysis, Membranes. 12 (2022) 989. https://doi.org/10.3390/membranes12100989.
[154] P. Teppor, R. Jäger, J. Nerut, M. Koppel, J. Aruväli, O. Volobujeva, E. Lust, Valorization of Naturally Abundant Low-Value Peat into Highly Active Non-Platinum Group Metal Oxygen Reduction Catalysts, ECS Trans. 111 (2023) 73. https://doi.org/10.1149/11105.0073ecst.
[155] A. Bonakdarpour, M. Lefevre, R. Yang, F. Jaouen, T. Dahn, J.-P. Dodelet, J.R. Dahn, Impact of Loading in RRDE Experiments on Fe–N–C Catalysts: Two- or Four-Electron Oxygen Reduction?, Electrochem. Solid-State Lett. 11 (2008) B105. https://doi.org/10.1149/1.2904768.
[156] C.-C. Liu, H.-Y. Chen, H.-P. Jhong, S.-T. Chang, K.-C. Wang, Y.-C. Chang, H.-C. Huang, C.-H. Wang, In-situ growth of iron phosphide encapsulated by carbon nanotubes decorated with zeolitic imidazolate framework-8 for enhancing oxygen reduction reaction, Int. J. Hydrog. Energy. 47 (2022) 17367–17378. https://doi.org/10.1016/j.ijhydene.2022.03.228.
[157] N. Norouzi, F.A. Choudhury, H.M. El-Kaderi, Iron Phosphide Doped, Porous Carbon as an Efficient Electrocatalyst for Oxygen Reduction Reaction, ACS Appl. Energy Mater. 3 (2020) 2537–2546. https://doi.org/10.1021/acsaem.9b02250.
[158] T.-N. Tran, M.Y. Song, T.-H. Kang, J. Samdani, H.-Y. Park, H. Kim, S.H. Jhung, J.-S. Yu, Iron Phosphide Incorporated into Iron-Treated Heteroatoms-Doped Porous Bio-Carbon as Efficient Electrocatalyst for the Oxygen Reduction Reaction, ChemElectroChem. 5 (2018) 1944–1953. https://doi.org/10.1002/celc.201800091.
[159] G. Huang, M. Mandal, X. Peng, A.C. Yang-Neyerlin, B.S. Pivovar, W.E. Mustain, P.A. Kohl, Composite Poly(norbornene) Anion Conducting Membranes for Achieving Durability, Water Management and High Power (3.4 W/cm2) in Hydrogen/Oxygen Alkaline Fuel Cells, J. Electrochem. Soc. 166 (2019) F637. https://doi.org/10.1149/2.1301910jes.
[160] Z. Li, H. Sun, L. Wei, W.-J. Jiang, M. Wu, J.-S. Hu, Lamellar Metal Organic Framework-Derived Fe–N–C Non-Noble Electrocatalysts with Bimodal Porosity for Efficient Oxygen Reduction, ACS Appl. Mater. Interfaces. 9 (2017) 5272–5278. https://doi.org/10.1021/acsami.6b15154.
[161] H.-W. Liang, X. Zhuang, S. Brüller, X. Feng, K. Müllen, Hierarchically porous carbons with optimized nitrogen doping as highly active electrocatalysts for oxygen reduction, Nat. Commun. 5 (2014) 4973. https://doi.org/10.1038/ncomms5973.
[162] E. Proietti, F. Jaouen, M. Lefèvre, N. Larouche, J. Tian, J. Herranz, J.-P. Dodelet, Iron-based cathode catalyst with enhanced power density in polymer electrolyte membrane fuel cells, Nat. Commun. 2 (2011) 416. https://doi.org/10.1038/ncomms1427.
[163] M. Wu, K. Wang, M. Yi, Y. Tong, Y. Wang, S. Song, A Facile Activation Strategy for an MOF-Derived Metal-Free Oxygen Reduction Reaction Catalyst: Direct Access to Optimized Pore Structure and Nitrogen Species, ACS Catal. 7 (2017) 6082–6088. https://doi.org/10.1021/acscatal.7b01649.
[164] A. Tan, Y. Wang, Z. Fu, P. Tsiakaras, Z. Liang, Highly effective oxygen reduction reaction electrocatalysis: Nitrogen-doped hierarchically mesoporous carbon derived from interpenetrated nonporous metal-organic frameworks, Appl Catal B. 218 (2017) 260–266. https://doi.org/10.1016/j.apcatb.2017.06.051.

10. SUMMARY IN ESTONIAN

Eestimaise turba väärindamine plaatina-vabadeks hapniku redutseerumise katalüsaatoriteks

Käesolevas töös valmistati kahe sünteesimetoodiga looduslikust eestimaisest hästilagunenud turbast mitte-väärismetalli tüüpi (NPGM) hapniku redutseerumisreaktsiooni (ORR) katalüsaatorid. Saadud materjale uuriti erinevate füüsikaliste ja elektrokeemiliste karakteriseerimismeetoditega. Andmete analüüsist selgusid mitmed seosed katalüsaatorite aktiivsuse ja füüsikaliste omaduste vahel.

Sünteesimetoodika #1 puhul karboniseeriti turvas esmajoones süsinikalusmaterjaliks kasutades erinevaid aktiveerivaid aineid või mitmesammulist pürolüüsi. Seejärel modifitseeriti süsinikalusmaterjale koobalti ja lämmastikuga ja saadi NPGM katalüsaatorid. Töös näidati, et karboniseerimise tingimused mõjutasid oluliselt materjalide füüsikalisi ja elektrokeemilisi omadusi. Kui süsiniku sünteesil kasutati aktiveerivaid aineid ($ZnCl_2$, $FeCl_3$, KOH), saadi suurema poorsusega materjalid. NPGM katalüsaatorite puhul saavutati kõrgeim aktiivsus nii happelises kui ka aluselises keskkonnas nii kolme-elektroodses pöörleva ketaselektroodi kui ka kahe-elektroodses kütuseelemendi katses just katalüsaatoriga, kus süsinikalusmaterjali sünteesil kasutati aktiveeriva ainena $ZnCl_2$-i. Lisaks leiti, et elektroodide korral, mis koosnesid väiksematest katalüsaatorite osakestest, saavutati anioonivahetusmembraaniga kütuseelemendi (AEMFC) katses kõrgem aktiivsus. Järelikult on NPGM katalüsaatorite sünteesimisel $ZnCl_2$ kasutamine aktiveeriva ainena õigustatud.

Sünteesimetoodika #2 puhul karboniseeriti turvas koos raua ja lämmastiku allikaga. Lisaks kasutati eelmise osa tulemustele tuginedes aktiveeriva ainena $ZnCl_2$-i. Vahetatud sünteesimetoodikaga saadi NPGM katalüsaator, mille aktiivsus oli kõrgem võrreldes eelmise metoodikaga saadud katalüsaatoritega. Sünteesimetoodikas tõsteti rauda sisaldava lähteaine ja $ZnCl_2$ koguseid ning pürolüüsitemperatuuri 800 °C pealt 1000 °C–ni, mille tagajärjel saavutati veelgi kõrgema ORR aktiivsusega NPGM katalüsaatorid. Kõrgem aktiivsus kolme-elektroodses süsteemis seostati suurema mikropoorsuse ja Fe-N_x ning nn grafiitse lämmastiku osakaaluga materjalis. Samas ei avaldunud kõrgem aktiivsus kahe-elektroodses AEMFC katses materjalide vähese meso- ja makropoorsuse tõttu.

Poorsuse suurendamiseks lisati sünteesi lähteainete hulka peamiselt kaltsiumist ja fosforist koosnevat hüdroksüapatiiti (HA), mis käitus kui "kõva" poorimoodustaja. Töös kasutati HA nanoosakesi, mille laius oli ligikaudu 20 nm ja pikkus 80 nm. HA-st poorimoodustaja eeliseks on see, et selle eemaldamiseks materjalist ei pea kasutama ohtlikku HF-i, mida vajavad tavapärased räni sisaldavad meso- ja makropooride moodustajad. Pärast 1 M HNO_3 happelahusega pesemist, mis eemaldas materjalist HA, tekkis ainulaadse struktuuriga NPGM katalüsaator, mille struktuuris oli palju meso- ja makropoore. AEMFC katses saadi uue materjaliga suurepärane tulemus maksimaalse võimsustihedusega

1060 mW cm^{-2}. Poorsuse suurendamise tagajärjel paranes katalüsaatoris aktiivtsentrite kättesaadavus ja lähteainete ning saaduste massitransport.

Käesolevas töös näidatakse, kuidas sünteesida hästilagunenud turbast ORR suhtes aktiivseid ja poorseid NPGM katalüsaatoreid ja kuidas täiustada sünteesimetoodikat, et saavutada katalüsaatoritele vajalikke füüsikalisi ja elektrokeemilisi omadusi. Töö tulemusena saadi eeskiri madala väärtusega kasutuseta ja keskkonda saastavaid gaase eritava maavara väärindamiseks kõrgtehnoloogiliseks materjaliks kütuseelemendi rakenduse jaoks.

11. ACKNOWLEDGEMENTS

Firstly, I want to sincerely thank my supervisors, Dr. Rutha Jäger and prof. Enn Lust, for providing me with everything I needed to grow as a young scientist. Under their supervision, with Rutha handling the comprehensive day-to-day supervision and Enn acting as a wise guide, I have grown from a lowly student with no notable skills to a (hopefully) independent young researcher who has a basic grasp on my own work. They have taught me invaluable skills on how to conduct research, how to understand the results, how to place the results into a broader context, and how to present the results to people in and out of academia.

I want to give a special thanks to Dr. Jaak Nerut for many fruitful discussions about electrochemistry and helping me learn how to conduct successful fuel cell and rotating ring disc electrode experiments. His input was critically important for my development as an electrochemist and for that reason I consider him as an unofficial third supervisor.

I want to thank all the co-authors of the publications included in this thesis for taking the time out of their undoubtedly busy schedules and conducting the various experiments and data analysis needed to get valuable information about the synthesized materials. They have helped me realize that science can truly flourish only with extensive cooperation. More specifically, I want to thank Dr. Maarja Paalo, Dr. Meelis Härmas, and M.Sc. Anu Adamson for synthesizing the peat-derived carbons in publications [I-III], Dr. Rasmus Palm for help with the low-temperature gas sorption data analysis [I-III] and conducting the mercury intrusion porosimetry measurements and data analysis [IV], Dr. Martin Månsson for providing the resources needed for the mercury intrusion porosimetry measurements [IV], Dr. Olga Volobujeva for conducting the HR-SEM and SEM-EDS measurements [I-IV], Dr. Eneli Härk and Dr. Zdravko Kochovski for conducting the TEM measurements [I, II, IV], Dr. Tavo Romann for conducting the Raman spectroscopy measurements [I, II], Dr. Riinu Härmas for analyzing the Raman data [I, II], M.Sc. Jaan Aruväli for conducting the XRD measurements and data analysis [I-IV], Dr. Arvo Kikas for conducting the XPS measurements and data analysis [I, II], Dr. Kuno Kooser for conducting the XPS measurements and data analysis [IV], Dr. Sari Granroth for conducting the XPS measurements [IV], and Dr Tanel Käämbre for conducting the XAS measurements and data analysis [IV].

I want to also thank all my wonderful co-workers both in room 5040 and in the whole building for making my 8 long years in the workplace a fun and enjoyable experience in addition to a productive learning one.

Finally, I want to thank my family for unconditionally supporting me throughout this endeavor. My deepest gratitude goes to my girlfriend M.Sc. Miriam Koppel who has helped me retain my sanity by enduring my shenanigans both at work and at home. Also, thanks for splitting the rent.

This research was funded by the EU through the European Regional Development Fund under projects TK141 (2014-2020.4.01.15-0011) and grant No. MAX-TEENUS 2014-2020.4.01.20-0278 to University of Tartu; the Estonian Research Council through projects PRG676, PRG551, PUT1581 (1.01.2017–31.12.2020), NAMUR (3.2.0304.12-0397), NAMUR+ core facility funded by the Estonian Research Council (TT 13); the Estonian institutional research grant IUT20-13; ASTRA project PER ASPERA Graduate School of Functional Materials and Technologies receiving funding from the European Regional Development Fund; AuVe Tech OÜ through project LLTKT20148; the Materials Research Infrastructure (MARI)/Department of Physics and Astronomy, University of Turku; Ragnar Holm's Foundation; the Swedish Research Council, VR (Dnr. 2021-06157 and Dnr. 2022-03936).

PUBLICATIONS

CURRICULUM VITAE

Name: Patrick Teppor
Date of birth: April 15, 1995
Citizenship: Estonian
Contact: Institute of Chemistry, University of Tartu, Ravila 14a, 50411, Tartu, Estonia
E-mail: patrick.teppor@ut.ee

Education:

2019–…	University of Tartu, chemistry, Ph. D.
2017–2019	University of Tartu, materials science, M. Sc., *cum laude*
2014–2017	University of Tartu, materials science, B. Sc., *cum laude*
2002-2024	Jõhvi Gymnasium

Professional employment:

2017–…	University of Tartu, Institute of Chemistry, Chemist

Scientific publications:

1. H.Q.V. Nguyen, J. Nerut, H. Kasuk, M. Härmas, P. Valk, T. Romann, M. Koppel, **P. Teppor**, J. Aruväli, O. Korjus, O. Volobujeva, E. Lust, Optimisation of the ethylene glycol reduction method for the synthesis of platinum-ceria-carbon materials as catalysts for the methanol oxidation reaction, *Journal of Solid State Electrochemistry*, 27, **2023**, 313.
2. **P. Teppor**, R. Jäger, M. Paalo, A. Adamson, M. Härmas, O. Volobujeva, J. Aruväli, R. Palm, E. Lust, Peat as a carbon source for non-platinum group metal oxygen electrocatalysts and AEMFC cathodes, *International Journal of Hydrogen Energy*, 47, **2022**, 16908.
3. R. Jäger, **P. Teppor**, M. Paalo, M. Härmas, A. Adamson, O. Volobujeva, E. Härk, Z. Kochovski, T. Romann, R. Härmas, J. Aruväli, A. Kikas, E. Lust, Synthesis and Characterization of Cobalt and Nitrogen Co-Doped Peat-Derived Carbon Catalysts for Oxygen Reduction in Acidic Media, *Catalysts*, 11, **2021**, 715.
4. **P. Teppor**, R. Jäger, M. Paalo, R. Palm, O. Volobujeva, E. Härk, Z. Kochovski, T. Romann, R. Härmas, J. Aruväli, A. Kikas, E. Lust, Peat-derived carbon-based non-platinum group metal type catalyst for oxygen reduction and evolution reactions, *Electrochemistry Communications*, 113, **2020**, 106700.
5. **P. Teppor**, R. Jäger, E. Härk, S. Sepp, M. Kook, O. Volobujeva, P. Paiste, Z. Kochovski, I. Tallo, E. Lust, Exploring Different Synthesis Parameters for the Preparation of Metal-Nitrogen-Carbon Type Oxygen Reduction Catalysts, *Journal of the Electrochemical Society*, 167, **2020**, 054513.
6. R. Jäger, P.E. Kasatkin, E. Härk, **P. Teppor**, T. Romann, R. Härmas, I. Tallo, U. Mäeorg, U. Joost, P. Paiste, K. Kirsimäe, E. Lust, The effect of N

precursors in Fe-N/C type catalysts based on activated silicon carbide derived carbon for oxygen reduction activity at various pH values, *Journal of Electroanalytical Chemistry*, 823, **2018**, 593.
7. **P. Teppor**, R. Jäger, E. Härk, I. Tallo, U. Joost, M. Kook, P. Paiste, K. Šmits, K. Kirsimäe, E. Lust, ORR Activity and Stability of Co-N/C Catalysts Based on Silicon Carbide Derived Carbon and the Impact of Loading in Acidic Media, *Journal of the Electrochemical Society*, 165, **2018**, F1217.
8. P.E. Kasatkin, R. Jäger, E. Härk, **P. Teppor**, I. Tallo, U. Joost, K. Šmits, R. Kanarbik, E. Lust, Fe-N/C catalysts for oxygen reduction based on silicon carbide derived carbon, *Electrochemistry Communications*, 80, **2017**, 33.

ELULOOKIRJELDUS

Nimi: Patrick Teppor
Sünniaeg: 15. aprill 1995
Kodakondsus: Eesti
Kontakt: Tartu Ülikooli keemia instituut, Ravila 14a, 50411, Tartu, Eesti
E-post: patrick.teppor@ut.ee

Haridus:

2019–…	Tartu Ülikool, keemia, Ph. D.
2017–2019	Tartu Ülikool, materjaliteadus, M. Sc., *cum laude*
2014–2017	Tartu Ülikool, materjaliteadus, B. Sc., *cum laude*
2002–2014	Jõhvi Gümnaasium

Töökogemus:

2017–…	Tartu Ülikool, keemia instituut, keemik

Teaduspublikatsioonid:

1. H.Q.V. Nguyen, J. Nerut, H. Kasuk, M. Härmas, P. Valk, T. Romann, M. Koppel, **P. Teppor**, J. Aruväli, O. Korjus, O. Volobujeva, E. Lust, Optimisation of the ethylene glycol reduction method for the synthesis of platinum-ceria-carbon materials as catalysts for the methanol oxidation reaction, *Journal of Solid State Electrochemistry*, 27, **2023**, 313.
2. **P. Teppor**, R. Jäger, M. Paalo, A. Adamson, M. Härmas, O. Volobujeva, J. Aruväli, R. Palm, E. Lust, Peat as a carbon source for non-platinum group metal oxygen electrocatalysts and AEMFC cathodes, *International Journal of Hydrogen Energy*, 47, **2022**, 16908.
3. R. Jäger, **P. Teppor**, M. Paalo, M. Härmas, A. Adamson, O. Volobujeva, E. Härk, Z. Kochovski, T. Romann, R. Härmas, J. Aruväli, A. Kikas, E. Lust, Synthesis and Characterization of Cobalt and Nitrogen Co-Doped Peat-Derived Carbon Catalysts for Oxygen Reduction in Acidic Media, *Catalysts*, 11, **2021**, 715.
4. **P. Teppor**, R. Jäger, M. Paalo, R. Palm, O. Volobujeva, E. Härk, Z. Kochovski, T. Romann, R. Härmas, J. Aruväli, A. Kikas, E. Lust, Peat-derived carbon-based non-platinum group metal type catalyst for oxygen reduction and evolution reactions, *Electrochemistry Communications*, 113, **2020**, 106700.
5. **P. Teppor**, R. Jäger, E. Härk, S. Sepp, M. Kook, O. Volobujeva, P. Paiste, Z. Kochovski, I. Tallo, E. Lust, Exploring Different Synthesis Parameters for the Preparation of Metal-Nitrogen-Carbon Type Oxygen Reduction Catalysts, *Journal of the Electrochemical Society*, 167, **2020**, 054513.
6. R. Jäger, P.E. Kasatkin, E. Härk, **P. Teppor**, T. Romann, R. Härmas, I. Tallo, U. Mäeorg, U. Joost, P. Paiste, K. Kirsimäe, E. Lust, The effect of N

precursors in Fe-N/C type catalysts based on activated silicon carbide derived carbon for oxygen reduction activity at various pH values, *Journal of Electroanalytical Chemistry*, 823, **2018**, 593.
7. **P. Teppor**, R. Jäger, E. Härk, I. Tallo, U. Joost, M. Kook, P. Paiste, K. Šmits, K. Kirsimäe, E. Lust, ORR Activity and Stability of Co-N/C Catalysts Based on Silicon Carbide Derived Carbon and the Impact of Loading in Acidic Media, *Journal of the Electrochemical Society*, 165, **2018**, F1217.
8. P.E. Kasatkin, R. Jäger, E. Härk, **P. Teppor**, I. Tallo, U. Joost, K. Šmits, R. Kanarbik, E. Lust, Fe-N/C catalysts for oxygen reduction based on silicon carbide derived carbon, *Electrochemistry Communications*, 80, **2017**, 33.

DISSERTATIONES CHIMICAE UNIVERSITATIS TARTUENSIS

1. **Toomas Tamm.** Quantum-chemical simulation of solvent effects. Tartu, 1993, 110 p.
2. **Peeter Burk.** Theoretical study of gas-phase acid-base equilibria. Tartu, 1994, 96 p.
3. **Victor Lobanov.** Quantitative structure-property relationships in large descriptor spaces. Tartu, 1995, 135 p.
4. **Vahur Mäemets.** The ^{17}O and ^{1}H nuclear magnetic resonance study of H_2O in individual solvents and its charged clusters in aqueous solutions of electrolytes. Tartu, 1997, 140 p.
5. **Andrus Metsala.** Microcanonical rate constant in nonequilibrium distribution of vibrational energy and in restricted intramolecular vibrational energy redistribution on the basis of slater's theory of unimolecular reactions. Tartu, 1997, 150 p.
6. **Uko Maran.** Quantum-mechanical study of potential energy surfaces in different environments. Tartu, 1997, 137 p.
7. **Alar Jänes.** Adsorption of organic compounds on antimony, bismuth and cadmium electrodes. Tartu, 1998, 219 p.
8. **Kaido Tammeveski.** Oxygen electroreduction on thin platinum films and the electrochemical detection of superoxide anion. Tartu, 1998, 139 p.
9. **Ivo Leito.** Studies of Brønsted acid-base equilibria in water and non-aqueous media. Tartu, 1998, 101 p.
10. **Jaan Leis.** Conformational dynamics and equilibria in amides. Tartu, 1998, 131 p.
11. **Toonika Rinken.** The modelling of amperometric biosensors based on oxidoreductases. Tartu, 2000, 108 p.
12. **Dmitri Panov.** Partially solvated Grignard reagents. Tartu, 2000, 64 p.
13. **Kaja Orupõld.** Treatment and analysis of phenolic wastewater with microorganisms. Tartu, 2000, 123 p.
14. **Jüri Ivask.** Ion Chromatographic determination of major anions and cations in polar ice core. Tartu, 2000, 85 p.
15. **Lauri Vares.** Stereoselective Synthesis of Tetrahydrofuran and Tetrahydropyran Derivatives by Use of Asymmetric Horner-Wadsworth-Emmons and Ring Closure Reactions. Tartu, 2000, 184 p.
16. **Martin Lepiku.** Kinetic aspects of dopamine D_2 receptor interactions with specific ligands. Tartu, 2000, 81 p.
17. **Katrin Sak.** Some aspects of ligand specificity of P2Y receptors. Tartu, 2000, 106 p.
18. **Vello Pällin.** The role of solvation in the formation of iotsitch complexes. Tartu, 2001, 95 p.
19. **Katrin Kollist.** Interactions between polycyclic aromatic compounds and humic substances. Tartu, 2001, 93 p.

20. **Ivar Koppel.** Quantum chemical study of acidity of strong and superstrong Brønsted acids. Tartu, 2001, 104 p.
21. **Viljar Pihl.** The study of the substituent and solvent effects on the acidity of OH and CH acids. Tartu, 2001, 132 p.
22. **Natalia Palm.** Specification of the minimum, sufficient and significant set of descriptors for general description of solvent effects. Tartu, 2001, 134 p.
23. **Sulev Sild.** QSPR/QSAR approaches for complex molecular systems. Tartu, 2001, 134 p.
24. **Ruslan Petrukhin.** Industrial applications of the quantitative structure-property relationships. Tartu, 2001, 162 p.
25. **Boris V. Rogovoy.** Synthesis of (benzotriazolyl)carboximidamides and their application in relations with *N*- and *S*-nucleophyles. Tartu, 2002, 84 p.
26. **Koit Herodes.** Solvent effects on UV-vis absorption spectra of some solvatochromic substances in binary solvent mixtures: the preferential solvation model. Tartu, 2002, 102 p.
27. **Anti Perkson.** Synthesis and characterisation of nanostructured carbon. Tartu, 2002, 152 p.
28. **Ivari Kaljurand.** Self-consistent acidity scales of neutral and cationic Brønsted acids in acetonitrile and tetrahydrofuran. Tartu, 2003, 108 p.
29. **Karmen Lust.** Adsorption of anions on bismuth single crystal electrodes. Tartu, 2003, 128 p.
30. **Mare Piirsalu.** Substituent, temperature and solvent effects on the alkaline hydrolysis of substituted phenyl and alkyl esters of benzoic acid. Tartu, 2003, 156 p.
31. **Meeri Sassian.** Reactions of partially solvated Grignard reagents. Tartu, 2003, 78 p.
32. **Tarmo Tamm.** Quantum chemical modelling of polypyrrole. Tartu, 2003. 100 p.
33. **Erik Teinemaa.** The environmental fate of the particulate matter and organic pollutants from an oil shale power plant. Tartu, 2003. 102 p.
34. **Jaana Tammiku-Taul.** Quantum chemical study of the properties of Grignard reagents. Tartu, 2003. 120 p.
35. **Andre Lomaka.** Biomedical applications of predictive computational chemistry. Tartu, 2003. 132 p.
36. **Kostyantyn Kirichenko.** Benzotriazole – Mediated Carbon–Carbon Bond Formation. Tartu, 2003. 132 p.
37. **Gunnar Nurk.** Adsorption kinetics of some organic compounds on bismuth single crystal electrodes. Tartu, 2003, 170 p.
38. **Mati Arulepp.** Electrochemical characteristics of porous carbon materials and electrical double layer capacitors. Tartu, 2003, 196 p.
39. **Dan Cornel Fara.** QSPR modeling of complexation and distribution of organic compounds. Tartu, 2004, 126 p.
40. **Riina Mahlapuu.** Signalling of galanin and amyloid precursor protein through adenylate cyclase. Tartu, 2004, 124 p.

41. **Mihkel Kerikmäe.** Some luminescent materials for dosimetric applications and physical research. Tartu, 2004, 143 p.
42. **Jaanus Kruusma.** Determination of some important trace metal ions in human blood. Tartu, 2004, 115 p.
43. **Urmas Johanson.** Investigations of the electrochemical properties of polypyrrole modified electrodes. Tartu, 2004, 91 p.
44. **Kaido Sillar.** Computational study of the acid sites in zeolite ZSM-5. Tartu, 2004, 80 p.
45. **Aldo Oras.** Kinetic aspects of dATPαS interaction with $P2Y_1$ receptor. Tartu, 2004, 75 p.
46. **Erik Mölder.** Measurement of the oxygen mass transfer through the air-water interface. Tartu, 2005, 73 p.
47. **Thomas Thomberg.** The kinetics of electroreduction of peroxodisulfate anion on cadmium (0001) single crystal electrode. Tartu, 2005, 95 p.
48. **Olavi Loog.** Aspects of condensations of carbonyl compounds and their imine analogues. Tartu, 2005, 83 p.
49. **Siim Salmar.** Effect of ultrasound on ester hydrolysis in aqueous ethanol. Tartu, 2006, 73 p.
50. **Ain Uustare.** Modulation of signal transduction of heptahelical receptors by other receptors and G proteins. Tartu, 2006, 121 p.
51. **Sergei Yurchenko.** Determination of some carcinogenic contaminants in food. Tartu, 2006, 143 p.
52. **Kaido Tämm.** QSPR modeling of some properties of organic compounds. Tartu, 2006, 67 p.
53. **Olga Tšubrik.** New methods in the synthesis of multisubstituted hydrazines. Tartu. 2006, 183 p.
54. **Lilli Sooväli.** Spectrophotometric measurements and their uncertainty in chemical analysis and dissociation constant measurements. Tartu, 2006, 125 p.
55. **Eve Koort.** Uncertainty estimation of potentiometrically measured ph and pK_a values. Tartu, 2006, 139 p.
56. **Sergei Kopanchuk.** Regulation of ligand binding to melanocortin receptor subtypes. Tartu, 2006, 119 p.
57. **Silvar Kallip.** Surface structure of some bismuth and antimony single crystal electrodes. Tartu, 2006, 107 p.
58. **Kristjan Saal.** Surface silanization and its application in biomolecule coupling. Tartu, 2006, 77 p.
59. **Tanel Tätte.** High viscosity $Sn(OBu)_4$ oligomeric concentrates and their applications in technology. Tartu, 2006, 91 p.
60. **Dimitar Atanasov Dobchev**. Robust QSAR methods for the prediction of properties from molecular structure. Tartu, 2006, 118 p.
61. **Hannes Hagu**. Impact of ultrasound on hydrophobic interactions in solutions. Tartu, 2007, 81 p.
62. **Rutha Jäger.** Electroreduction of peroxodisulfate anion on bismuth electrodes. Tartu, 2007, 142 p.

63. **Kaido Viht.** Immobilizable bisubstrate-analogue inhibitors of basophilic protein kinases: development and application in biosensors. Tartu, 2007, 88 p.
64. **Eva-Ingrid Rõõm.** Acid-base equilibria in nonpolar media. Tartu, 2007, 156 p.
65. **Sven Tamp.** DFT study of the cesium cation containing complexes relevant to the cesium cation binding by the humic acids. Tartu, 2007, 102 p.
66. **Jaak Nerut.** Electroreduction of hexacyanoferrate(III) anion on Cadmium (0001) single crystal electrode. Tartu, 2007, 180 p.
67. **Lauri Jalukse.** Measurement uncertainty estimation in amperometric dissolved oxygen concentration measurement. Tartu, 2007, 112 p.
68. **Aime Lust.** Charge state of dopants and ordered clusters formation in CaF_2:Mn and CaF_2:Eu luminophors. Tartu, 2007, 100 p.
69. **Iiris Kahn**. Quantitative Structure-Activity Relationships of environmentally relevant properties. Tartu, 2007, 98 p.
70. **Mari Reinik.** Nitrates, nitrites, N-nitrosamines and polycyclic aromatic hydrocarbons in food: analytical methods, occurrence and dietary intake. Tartu, 2007, 172 p.
71. **Heili Kasuk.** Thermodynamic parameters and adsorption kinetics of organic compounds forming the compact adsorption layer at Bi single crystal electrodes. Tartu, 2007, 212 p.
72. **Erki Enkvist.** Synthesis of adenosine-peptide conjugates for biological applications. Tartu, 2007, 114 p.
73. **Svetoslav Hristov Slavov**. Biomedical applications of the QSAR approach. Tartu, 2007, 146 p.
74. **Eneli Härk.** Electroreduction of complex cations on electrochemically polished Bi(*hkl*) single crystal electrodes. Tartu, 2008, 158 p.
75. **Priit Möller.** Electrochemical characteristics of some cathodes for medium temperature solid oxide fuel cells, synthesized by solid state reaction technique. Tartu, 2008, 90 p.
76. **Signe Viggor.** Impact of biochemical parameters of genetically different pseudomonads at the degradation of phenolic compounds. Tartu, 2008, 122 p.
77. **Ave Sarapuu.** Electrochemical reduction of oxygen on quinone-modified carbon electrodes and on thin films of platinum and gold. Tartu, 2008, 134 p.
78. **Agnes Kütt.** Studies of acid-base equilibria in non-aqueous media. Tartu, 2008, 198 p.
79. **Rouvim Kadis.** Evaluation of measurement uncertainty in analytical chemistry: related concepts and some points of misinterpretation. Tartu, 2008, 118 p.
80. **Valter Reedo.** Elaboration of IVB group metal oxide structures and their possible applications. Tartu, 2008, 98 p.
81. **Aleksei Kuznetsov.** Allosteric effects in reactions catalyzed by the cAMP-dependent protein kinase catalytic subunit. Tartu, 2009, 133 p.

82. **Aleksei Bredihhin.** Use of mono- and polyanions in the synthesis of multisubstituted hydrazine derivatives. Tartu, 2009, 105 p.
83. **Anu Ploom.** Quantitative structure-reactivity analysis in organosilicon chemistry. Tartu, 2009, 99 p.
84. **Argo Vonk.** Determination of adenosine A_{2A}- and dopamine D_1 receptor-specific modulation of adenylate cyclase activity in rat striatum. Tartu, 2009, 129 p.
85. **Indrek Kivi.** Synthesis and electrochemical characterization of porous cathode materials for intermediate temperature solid oxide fuel cells. Tartu, 2009, 177 p.
86. **Jaanus Eskusson.** Synthesis and characterisation of diamond-like carbon thin films prepared by pulsed laser deposition method. Tartu, 2009, 117 p.
87. **Marko Lätt.** Carbide derived microporous carbon and electrical double layer capacitors. Tartu, 2009, 107 p.
88. **Vladimir Stepanov.** Slow conformational changes in dopamine transporter interaction with its ligands. Tartu, 2009, 103 p.
89. **Aleksander Trummal.** Computational Study of Structural and Solvent Effects on Acidities of Some Brønsted Acids. Tartu, 2009, 103 p.
90. **Eerold Vellemäe.** Applications of mischmetal in organic synthesis. Tartu, 2009, 93 p.
91. **Sven Parkel.** Ligand binding to 5-HT_{1A} receptors and its regulation by Mg^{2+} and Mn^{2+}. Tartu, 2010, 99 p.
92. **Signe Vahur.** Expanding the possibilities of ATR-FT-IR spectroscopy in determination of inorganic pigments. Tartu, 2010, 184 p.
93. **Tavo Romann**. Preparation and surface modification of bismuth thin film, porous, and microelectrodes. Tartu, 2010, 155 p.
94. **Nadežda Aleksejeva.** Electrocatalytic reduction of oxygen on carbon nanotube-based nanocomposite materials. Tartu, 2010, 147 p.
95. **Marko Kullapere.** Electrochemical properties of glassy carbon, nickel and gold electrodes modified with aryl groups. Tartu, 2010, 233 p.
96. **Liis Siinor.** Adsorption kinetics of ions at Bi single crystal planes from aqueous electrolyte solutions and room-temperature ionic liquids. Tartu, 2010, 101 p.
97. **Angela Vaasa.** Development of fluorescence-based kinetic and binding assays for characterization of protein kinases and their inhibitors. Tartu 2010, 101 p.
98. **Indrek Tulp.** Multivariate analysis of chemical and biological properties. Tartu 2010, 105 p.
99. **Aare Selberg.** Evaluation of environmental quality in Northern Estonia by the analysis of leachate. Tartu 2010, 117 p.
100. **Darja Lavõgina.** Development of protein kinase inhibitors based on adenosine analogue-oligoarginine conjugates. Tartu 2010, 248 p.
101. **Laura Herm.** Biochemistry of dopamine D_2 receptors and its association with motivated behaviour. Tartu 2010, 156 p.

102. **Terje Raudsepp.** Influence of dopant anions on the electrochemical properties of polypyrrole films. Tartu 2010, 112 p.
103. **Margus Marandi.** Electroformation of Polypyrrole Films: *In-situ* AFM and STM Study. Tartu 2011, 116 p.
104. **Kairi Kivirand.** Diamine oxidase-based biosensors: construction and working principles. Tartu, 2011, 140 p.
105. **Anneli Kruve.** Matrix effects in liquid-chromatography electrospray mass-spectrometry. Tartu, 2011, 156 p.
106. **Gary Urb.** Assessment of environmental impact of oil shale fly ash from PF and CFB combustion. Tartu, 2011, 108 p.
107. **Nikita Oskolkov.** A novel strategy for peptide-mediated cellular delivery and induction of endosomal escape. Tartu, 2011, 106 p.
108. **Dana Martin.** The QSPR/QSAR approach for the prediction of properties of fullerene derivatives. Tartu, 2011, 98 p.
109. **Säde Viirlaid.** Novel glutathione analogues and their antioxidant activity. Tartu, 2011, 106 p.
110. **Ülis Sõukand.** Simultaneous adsorption of Cd^{2+}, Ni^{2+}, and Pb^{2+} on peat. Tartu, 2011, 124 p.
111. **Lauri Lipping.** The acidity of strong and superstrong Brønsted acids, an outreach for the "limits of growth": a quantum chemical study. Tartu, 2011, 124 p.
112. **Heisi Kurig.** Electrical double-layer capacitors based on ionic liquids as electrolytes. Tartu, 2011, 146 p.
113. **Marje Kasari.** Bisubstrate luminescent probes, optical sensors and affinity adsorbents for measurement of active protein kinases in biological samples. Tartu, 2012, 126 p.
114. **Kalev Takkis.** Virtual screening of chemical databases for bioactive molecules. Tartu, 2012, 122 p.
115. **Ksenija Kisseljova**. Synthesis of aza-β^3-amino acid containing peptides and kinetic study of their phosphorylation by protein kinase A. Tartu, 2012, 104 p.
116. **Riin Rebane.** Advanced method development strategy for derivatization LC/ESI/MS. Tartu, 2012, 184 p.
117. **Vladislav Ivaništšev.** Double layer structure and adsorption kinetics of ions at metal electrodes in room temperature ionic liquids. Tartu, 2012, 128 p.
118. **Irja Helm.** High accuracy gravimetric Winkler method for determination of dissolved oxygen. Tartu, 2012, 139 p.
119. **Karin Kipper.** Fluoroalcohols as Components of LC-ESI-MS Eluents: Usage and Applications. Tartu, 2012, 164 p.
120. **Arno Ratas.** Energy storage and transfer in dosimetric luminescent materials. Tartu, 2012, 163 p.
121. **Reet Reinart-Okugbeni**. Assay systems for characterisation of subtype-selective binding and functional activity of ligands on dopamine receptors. Tartu, 2012, 159 p.

122. **Lauri Sikk.** Computational study of the Sonogashira cross-coupling reaction. Tartu, 2012, 81 p.
123. **Karita Raudkivi.** Neurochemical studies on inter-individual differences in affect-related behaviour of the laboratory rat. Tartu, 2012, 161 p.
124. **Indrek Saar.** Design of GalR2 subtype specific ligands: their role in depression-like behavior and feeding regulation. Tartu, 2013, 126 p.
125. **Ann Laheäär.** Electrochemical characterization of alkali metal salt based non-aqueous electrolytes for supercapacitors. Tartu, 2013, 127 p.
126. **Kerli Tõnurist.** Influence of electrospun separator materials properties on electrochemical performance of electrical double-layer capacitors. Tartu, 2013, 147 p.
127. **Kaija Põhako-Esko.** Novel organic and inorganic ionogels: preparation and characterization. Tartu, 2013, 124 p.
128. **Ivar Kruusenberg.** Electroreduction of oxygen on carbon nanomaterial-based catalysts. Tartu, 2013, 191 p.
129. **Sander Piiskop.** Kinetic effects of ultrasound in aqueous acetonitrile solutions. Tartu, 2013, 95 p.
130. **Ilona Faustova**. Regulatory role of L-type pyruvate kinase N-terminal domain. Tartu, 2013, 109 p.
131. **Kadi Tamm.** Synthesis and characterization of the micro-mesoporous anode materials and testing of the medium temperature solid oxide fuel cell single cells. Tartu, 2013, 138 p.
132. **Iva Bozhidarova Stoyanova-Slavova.** Validation of QSAR/QSPR for regulatory purposes. Tartu, 2013, 109 p.
133. **Vitali Grozovski**. Adsorption of organic molecules at single crystal electrodes studied by *in situ* STM method. Tartu, 2014, 146 p.
134. **Santa Veikšina**. Development of assay systems for characterisation of ligand binding properties to melanocortin 4 receptors. Tartu, 2014, 151 p.
135. **Jüri Liiv.** PVDF (polyvinylidene difluoride) as material for active element of twisting-ball displays. Tartu, 2014, 111 p.
136. **Kersti Vaarmets.** Electrochemical and physical characterization of pristine and activated molybdenum carbide-derived carbon electrodes for the oxygen electroreduction reaction. Tartu, 2014, 131 p.
137. **Lauri Tõntson**. Regulation of G-protein subtypes by receptors, guanine nucleotides and Mn^{2+}. Tartu, 2014, 105 p.
138. **Aiko Adamson.** Properties of amine-boranes and phosphorus analogues in the gas phase. Tartu, 2014, 78 p.
139. **Elo Kibena**. Electrochemical grafting of glassy carbon, gold, highly oriented pyrolytic graphite and chemical vapour deposition-grown graphene electrodes by diazonium reduction method. Tartu, 2014, 184 p.
140. **Teemu Näykki.** Novel Tools for Water Quality Monitoring – From Field to Laboratory. Tartu, 2014, 202 p.
141. **Karl Kaupmees.** Acidity and basicity in non-aqueous media: importance of solvent properties and purity. Tartu, 2014, 128 p.

142. **Oleg Lebedev**. Hydrazine polyanions: different strategies in the synthesis of heterocycles. Tartu, 2015, 118 p.
143. **Geven Piir.** Environmental risk assessment of chemicals using QSAR methods. Tartu, 2015, 123 p.
144. **Olga Mazina.** Development and application of the biosensor assay for measurements of cyclic adenosine monophosphate in studies of G protein-coupled receptor signalinga. Tartu, 2015, 116 p.
145. **Sandip Ashokrao Kadam.** Anion receptors: synthesis and accurate binding measurements. Tartu, 2015, 116 p.
146. **Indrek Tallo.** Synthesis and characterization of new micro-mesoporous carbide derived carbon materials for high energy and power density electrical double layer capacitors. Tartu, 2015, 148 p.
147. **Heiki Erikson.** Electrochemical reduction of oxygen on nanostructured palladium and gold catalysts. Tartu, 2015, 204 p.
148. **Erik Anderson.** *In situ* Scanning Tunnelling Microscopy studies of the interfacial structure between Bi(111) electrode and a room temperature ionic liquid. Tartu, 2015, 118 p.
149. **Girinath G. Pillai.** Computational Modelling of Diverse Chemical, Biochemical and Biomedical Properties. Tartu, 2015, 140 p.
150. **Piret Pikma.** Interfacial structure and adsorption of organic compounds at Cd(0001) and Sb(111) electrodes from ionic liquid and aqueous electrolytes: an *in situ* STM study. Tartu, 2015, 126 p.
151. **Ganesh babu Manoharan.** Combining chemical and genetic approaches for photoluminescence assays of protein kinases. Tartu, 2016, 126 p.
152. **Carolin Siimenson**. Electrochemical characterization of halide ion adsorption from liquid mixtures at Bi(111) and pyrolytic graphite electrode surface. Tartu, 2016, 110 p.
153. **Asko Laaniste.** Comparison and optimisation of novel mass spectrometry ionisation sources. Tartu, 2016, 156 p.
154. **Hanno Evard.** Estimating limit of detection for mass spectrometric analysis methods. Tartu, 2016, 224 p.
155. **Kadri Ligi.** Characterization and application of protein kinase-responsive organic probes with triplet-singlet energy transfer. Tartu, 2016, 122 p.
156. **Margarita Kagan.** Biosensing penicillins' residues in milk flows. Tartu, 2016, 130 p.
157. **Marie Kriisa.** Development of protein kinase-responsive photoluminescent probes and cellular regulators of protein phosphorylation. Tartu, 2016, 106 p.
158. **Mihkel Vestli.** Ultrasonic spray pyrolysis deposited electrolyte layers for intermediate temperature solid oxide fuel cells. Tartu, 2016, 156 p.
159. **Silver Sepp**. Influence of porosity of the carbide-derived carbon on the properties of the composite electrocatalysts and characteristics of polymer electrolyte fuel cells. Tartu, 2016, 137 p.
160. **Kristjan Haav**. Quantitative relative equilibrium constant measurements in supramolecular chemistry. Tartu, 2017, 158 p.

161. **Anu Teearu**. Development of MALDI-FT-ICR-MS methodology for the analysis of resinous materials. Tartu, 2017, 205 p.
162. **Taavi Ivan**. Bifunctional inhibitors and photoluminescent probes for studies on protein complexes. Tartu, 2017, 140 p.
163. **Maarja-Liisa Oldekop**. Characterization of amino acid derivatization reagents for LC-MS analysis. Tartu, 2017, 147 p.
164. **Kristel Jukk**. Electrochemical reduction of oxygen on platinum- and palladium-based nanocatalysts. Tartu, 2017, 250 p.
165. **Siim Kukk**. Kinetic aspects of interaction between dopamine transporter and *N*-substituted nortropane derivatives. Tartu, 2017, 107 p.
166. **Birgit Viira**. Design and modelling in early drug development in targeting HIV-1 reverse transcriptase and Malaria. Tartu, 2017, 172 p.
167. **Rait Kivi**. Allostery in cAMP dependent protein kinase catalytic subunit. Tartu, 2017, 115 p.
168. **Agnes Heering**. Experimental realization and applications of the unified acidity scale. Tartu, 2017, 123 p.
169. **Delia Juronen**. Biosensing system for the rapid multiplex detection of mastitis-causing pathogens in milk. Tartu, 2018, 85 p.
170. **Hedi Rahnel.** ARC-inhibitors: from reliable biochemical assays to regulators of physiology of cells. Tartu, 2018, 176 p.
171. **Anton Ruzanov.** Computational investigation of the electrical double layer at metal–aqueous solution and metal–ionic liquid interfaces. Tartu, 2018, 129 p.
172. **Katrin Kestav.** Crystal Structure-Guided Development of Bisubstrate-Analogue Inhibitors of Mitotic Protein Kinase Haspin. Tartu, 2018, 166 p.
173. **Mihkel Ilisson.** Synthesis of novel heterocyclic hydrazine derivatives and their conjugates. Tartu, 2018, 101 p.
174. **Anni Allikalt.** Development of assay systems for studying ligand binding to dopamine receptors. Tartu, 2018, 160 p.
175. **Ove Oll.** Electrical double layer structure and energy storage characteristics of ionic liquid based capacitors. Tartu, 2018, 187 p.
176. **Rasmus Palm.** Carbon materials for energy storage applications. Tartu, 2018, 114 p.
177. **Jörgen Metsik.** Preparation and stability of poly(3,4-ethylenedioxythiophene) thin films for transparent electrode applications. Tartu, 2018, 111 p.
178. **Sofja Tšepelevitš.** Experimental studies and modeling of solute-solvent interactions. Tartu, 2018, 109 p.
179. **Märt Lõkov.** Basicity of some nitrogen, phosphorus and carbon bases in acetonitrile. Tartu, 2018, 104 p.
180. **Anton Mastitski**. Preparation of α-aza-amino acid precursors and related compounds by novel methods of reductive one-pot alkylation and direct alkylation. Tartu, 2018, 155 p.
181. **Jürgen Vahter**. Development of bisubstrate inhibitors for protein kinase CK2. Tartu, 2019, 186 p.

182. **Piia Liigand.** Expanding and improving methodology and applications of ionization efficiency measurements. Tartu, 2019, 189 p.
183. **Sigrid Selberg.** Synthesis and properties of lipophilic phosphazene-based indicator molecules. Tartu, 2019, 74 p.
184. **Jaanus Liigand.** Standard substance free quantification for LC/ESI/MS analysis based on the predicted ionization efficiencies. Tartu, 2019, 254 p.
185. **Marek Mooste.** Surface and electrochemical characterisation of aryl film and nanocomposite material modified carbon and metal-based electrodes. Tartu, 2019, 304 p.
186. **Mare Oja.** Experimental investigation and modelling of pH profiles for effective membrane permeability of drug substances. Tartu, 2019, 306 p.
187. **Sajid Hussain.** Electrochemical reduction of oxygen on supported Pt catalysts. Tartu, 2019, 220 p.
188. **Ronald Väli.** Glucose-derived hard carbon electrode materials for sodium-ion batteries. Tartu, 2019, 180 p.
189. **Ester Tee.** Analysis and development of selective synthesis methods of hierarchical micro- and mesoporous carbons. Tartu, 2019, 210 p.
190. **Martin Maide.** Influence of the microstructure and chemical composition of the fuel electrode on the electrochemical performance of reversible solid oxide fuel cell. Tartu, 2020, 144 p.
191. **Edith Viirlaid.** Biosensing Pesticides in Water Samples. Tartu, 2020, 102 p.
192. **Maike Käärik.** Nanoporous carbon: the controlled nanostructure, and structure-property relationships. Tartu, 2020, 162 p.
193. **Artur Gornischeff.** Study of ionization efficiencies for derivatized compounds in LC/ESI/MS and their application for targeted analysis. Tartu, 2020, 124 p.
194. **Reet Link.** Ligand binding, allosteric modulation and constitutive activity of melanocortin-4 receptors. Tartu, 2020, 108 p.
195. **Pilleriin Peets.** Development of instrumental methods for the analysis of textile fibres and dyes. Tartu, 2020, 150 p.
196. **Larisa Ivanova.** Design of active compounds against neurodegenerative diseases. Tartu, 2020, 152 p.
197. **Meelis Härmas.** Impact of activated carbon microstructure and porosity on electrochemical performance of electrical double-layer capacitors. Tartu, 2020, 122 p.
198. **Ruta Hecht.** Novel Eluent Additives for LC-MS Based Bioanalytical Methods. Tartu, 2020, 202 p.
199. **Max Hecht.** Advances in the Development of a Point-of-Care Mass Spectrometer Test. Tartu, 2020, 168 p.
200. **Ida Rahu.** Bromine formation in inorganic bromide/nitrate mixtures and its application for oxidative aromatic bromination. Tartu, 2020, 116 p.
201. **Sander Ratso**. Electrocatalysis of oxygen reduction on non-precious metal catalysts. Tartu, 2020, 371 p.
202. **Astrid Darnell.** Computational design of anion receptors and evaluation of host-guest binding. Tartu, 2021, 150 p.

203. **Ove Korjus.** The development of ceramic fuel electrode for solid oxide cells. Tartu, 2021, 150 p.
204. **Merit Oss.** Ionization efficiency in electrospray ionization source and its relations to compounds' physico-chemical properties. Tartu, 2021, 124 p.
205. **Madis Lüsi**. Electroreduction of oxygen on nanostructured palladium catalysts. Tartu, 2021, 180 p.
206. **Eliise Tammekivi.** Derivatization and quantitative gas-chromatographic analysis of oils. Tartu, 2021, 122 p.
207. **Simona Selberg.** Development of Small-Molecule Regulators of Epi-transcriptomic Processes. Tartu, 2021, 122 p.
208. **Olivier Etebe Nonga.** Inhibitors and photoluminescent probes for in vitro studies on protein kinases PKA and PIM. Tartu, 2021, 189 p.
209. **Riinu Härmas.** The structure and H2 diffusion in porous carbide-derived carbon particles. Tartu, 2022, 123 p.
210. **Maarja Paalo.** Synthesis and characterization of novel carbon electrodes for high power density electrochemical capacitors. Tartu, 2022, 144 p.
211. **Jinfeng Zhao.** Electrochemical characteristics of Bi(hkl) and micro-meso-porous carbon electrodes in ionic liquid based electrolytes. Tartu, 2022, 134 p.
212. **Alar Heinsaar.** Investigation of oxygen electrode materials for high-temperature solid oxide cells in natural conditions. Tartu, 2022, 120 p.
213. **Jaana Lilloja.** Transition metal and nitrogen doped nanocarbon cathode catalysts for anion exchange membrane fuel cells. Tartu, 2022, 202 p.
214. **Maris-Johanna Tahk.** Novel fluorescence-based methods for illuminating transmembrane signal transduction by G-protein coupled receptors. Tartu, 2022, 200 p.
215. **Eerik Jõgi.** Development and Applications of E. coli Immunosensor. Tartu, 2022, 103 p.
216. **Alo Rüütel.** Design principles of synthetic molecular receptors for anion-selective electrodes. Tartu, 2022, 109 p.
217. **Tanel Sõrmus.** Development of stimuli-responsive and covalent bisubstrate inhibitors of protein kinases. Tartu, 2022, 148 p.
218. **Oleg Artemchuk.** Autotrophic nitrogen removal processes for nutrient removal from sidestream and mainstream wastewater. Tartu, 2022, 115 p.
219. **Andre Leesment.** Quantitative studies of Brønsted acidity in biphasic systems and gas-phase. Tartu, 2023, 83 p.
220. **Meeli Arujõe-Sado.** Structural effects in aza-peptide bond formation reaction. Tartu, 2023, 83 p.
221. **Jonas Mart Linge.** Electrochemical reduction of oxygen on silver-based catalysts. Tartu, 2023, 269 p.
222. **Tõnis Laasfeld.** Integrating Image Analysis and Quantitative Modeling for a Holistic View of GPCR Ligand Binding Dynamics. Tartu, 2023, 226 p.
223. **Ernesto de Jesus Zapata Flores.** Derivatization Reagents used in negative mode electrospray LC-MS. Tartu, 2023, 107 p.